

DISSERTATION

TUNING OPTOELECTRONIC PROPERTIES AND UNDERSTANDING CHARGE  
TRANSPORT IN NANOCRYSTAL THIN FILMS OF EARTH ABUNDANT  
SEMICONDUCTING MATERIALS

Submitted by

Shannon C. Riha

Department of Chemistry

In partial fulfillment of the requirements

For the Degree of Doctor of Philosophy

Colorado State University

Fort Collins, Colorado

Summer 2011

Doctoral Committee:

Advisor: Bruce A. Parkinson

Co-Advisor: Amy L. Prieto

C. Michael Elliott

Stuart Field

Charles Henry

Anthony Rappe

## ABSTRACT

### TUNING OPTOELECTRONIC PROPERTIES AND UNDERSTANDING CHARGE TRANSPORT IN NANOCRYSTAL THIN FILMS OF EARTH ABUNDANT SEMICONDUCTING MATERIALS

With the capability of producing nearly 600 TW annually, solar power is one renewable energy source with the potential to meet a large fraction of the world's burgeoning energy demand. To make solar technology cost-competitive with carbon-based fuels, cheaper devices need to be realized. Solution-processed solar cells from nanocrystal inks of earth abundant materials satisfy this requirement. Nonetheless, a major hurdle in commercializing such devices is poor charge transport through nanocrystal thin films. The efficiency of charge transport through nanocrystal thin films is strongly dependent on the quality of the nanocrystals, as well as their optoelectronic properties. Therefore, the first part of this dissertation is focused on synthesizing high quality nanocrystals of  $\text{Cu}_2\text{ZnSnS}_4$ , a promising earth abundant photovoltaic absorber material. The optoelectronic properties of the nanocrystals were tuned by altering the copper to zinc ratio, as well as by introducing selenium to create  $\text{Cu}_2\text{ZnSn}(\text{S}_{1-x}\text{Se}_x)_4$  solid solutions. Photoelectrochemical characterization was used to test the  $\text{Cu}_2\text{ZnSnS}_4$  and  $\text{Cu}_2\text{ZnSn}(\text{S}_{1-x}\text{Se}_x)_4$  nanocrystal thin films. The results identify minority carrier diffusion

and recombination via the redox shuttle as the major loss mechanisms hindering efficient charge transport through the nanocrystal thin films. One way to solve this issue is to sinter the nanocrystals together, creating large grains for efficient charge transport. Although this may be quick and effective, it can lead to the formation of structural defects, among other issues. To this end, using a different copper-based material, namely  $\text{Cu}_2\text{Se}$ , and simple surface chemistry treatments, an alternative route to enhance charge transport through nanocrystals thin films is proposed.

## ACKNOWLEDGEMENTS

This dissertation and the work contained within would not have been possible had it not been for the certain people I have interacted with throughout this journey. First and foremost my wonderful husband Joe Mondloch, who has supported me both emotionally, as well as intellectually, throughout the past 4 years. He has put up with me in times of troubles and celebrated with me in times of triumph, pushed me through the many obstacles of graduate school, and most importantly, has been loving and encouraging the whole way through. I am thankful to my parents, Gary and Laurie Riha, who have provided love and support through every step of my life, even during those rebellious years of my life. They have always taught me to work hard/play hard, and that if you put your mind to it, nothing is impossible... it just might take a little while to get there. When I first moved to Colorado for graduate school, I knew very few people but over the years I have come to know quite a few. Aside from Joe, there are three people who have made a significant impact on my graduate school career: Dr. Doug Shepherd, Dr. Justin Sambur, and Sarah Fredrick. The fruitful scientific discussions and crazy ideas for experiments to try, the early mornings and late nights in the lab with Sarah, maintaining a lab transition with Justin, and the late night poker games at conferences with Doug have made these past few years far from uneventful. Of course I wouldn't have had many of these experiences and opportunities if it weren't for my two advisors, Dr.

Amy Prieto and Dr. Bruce Parkinson. I am especially grateful for allowing me the opportunity to bridge two seemingly different groups, such that I could develop expertise in not only nanomaterial synthesis but also materials/photoelectrochemical characterization. They have provided excellent guidance, pushed me harder and farther, and allowed me to think freely in order to become a successful chemist. Because I have two advisors, I have also had the opportunity to interact with members of both the Prieto and Parkinson lab. I have enjoyed my time working with everyone and thank you for providing an exciting and sometimes eventful place to work, as well as moral support. Although every one of the Parkinson and Prieto lab members have directly impacted my everyday life as a graduate student, there are two members in particular that I owe my gratitude to, Dr. Manashi Nath and Dr. Derek Johnson, who were post docs in the Parkinson and Prieto labs, respectively. I have learned a considerable amount from each of them, especially Manashi, who from the time I was an REU in the Parkinson lab, has given me the skill set to synthesize the intricate materials described herein. Last, but certainly not least, I would like to thank God, because it was he who put all these wonderful people into my life, and made this Ph. D. dissertation possible.

## TABLE OF CONTENTS

<b>CHAPTER 1</b>	INTRODUCTION .....	1
<b>CHAPTER 2</b>	ADVANCING SOLAR TECHNOLOGY: FUNDAMENTALS OF SOLAR CELLS AND THE KNOWLEDGE TRANSFER TOWARD SOLUTION-PROCESSED PHOTOVOLTAICS .....	4
	2.1 Overview .....	5
	2.2 Background of Solar Cells .....	6
	2.3 1 <sup>st</sup> Generation Photovoltaic Devices .....	11
	2.4 2 <sup>nd</sup> Generation Photovoltaic Devices .....	13
	2.5 Nanocrystal Thin Film Solar Cells .....	15
	2.6 Conclusions .....	20
	2.7 References .....	21
<b>CHAPTER 3</b>	TOWARD THE SYNTHESIS OF HIGH QUALITY NANOCRYSTALS: AN OVERVIEW OF THE HOT INJECTION METHOD .....	24
	3.1 Overview .....	24
	3.2 Background .....	25
	3.3 A Brief History Detailing the Hot Injection Method .....	26
	3.4 Nucleation and Growth .....	30
	3.5 Hot Injection Parameters Affecting Nucleation and Growth .....	33
	3.6 Conclusions .....	41
	3.7 References .....	43
<b>CHAPTER 4</b>	SOLUTION-BASED SYNTHESIS AND CHARACTERIZATION OF $\text{Cu}_2\text{ZnSnS}_4$ NANOCRYSTALS .....	46
	4.1 Overview .....	47
	4.2 Communication .....	47
	4.3 Experimental Details .....	52
	4.4 Acknowledgements .....	56
	4.5 References .....	57

	Supporting Information .....	59
<b>CHAPTER 5</b>	<b>PHOTOELECTRONCHEMICAL CHARACTERIZATION OF NANOCRYSTALLINE THIN FILM <math>\text{Cu}_2\text{ZnSnS}_4</math> PHOTOCATHODES .....</b>	<b>65</b>
	5.1 Overview .....	66
	5.2 Introduction .....	66
	5.3 Results and Discussion .....	70
	5.4 Conclusions .....	87
	5.5 Experimental Details .....	88
	5.6 Acknowledgements .....	91
	5.7 References .....	92
	Supporting Information .....	95
<b>CHAPTER 6</b>	<b>COMPOSITIONALLY TUNABLE <math>\text{Cu}_2\text{ZnSn}(\text{S}_{1-x}\text{Se}_x)_4</math> NANOCRYSTALS: PROBING THE EFFECT OF SE-INCLUSION IN MIXED CHALCOGENIDE THIN FILMS</b>	<b>100</b>
	6.1 Overview .....	101
	6.2 Communication .....	101
	6.3 Experimental Details .....	109
	6.4 Acknowledgements .....	111
	6.5 References .....	112
	Supporting Information .....	114
<b>CHAPTER 7</b>	<b><math>\text{Cu}_2\text{Se}</math> NANOPARTICLES WITH DUAL FUNCTIONALITY DUE TO A CONTROLLED SOLID-STATE PHASE TRANSITION DRIVEN BY COPPER OXIDATION AND CATIONIC CONDUCTION .....</b>	<b>120</b>
	7.1 Overview .....	121
	7.2 Introduction .....	121
	7.3 Results and Discussion .....	124
	7.4 Conclusion .....	136
	7.5 Experimental Details .....	137
	7.6 Acknowledgements .....	140
	7.7 References .....	141
	Supporting Information .....	146
<b>CHAPTER 8</b>	<b>SUMMARY .....</b>	<b>152</b>
<b>APPENDIX 1</b>	<b>PHOTOELECTROCHEMICAL CHARACTERIZATION OF <math>\text{Cu}_2\text{ZnSn}(\text{S}_{1-x}\text{Se}_x)_4</math> NANOCRYSTAL THIN FILMS .....</b>	<b>157</b>

## LIST OF FIGURES, TABLES, AND SCHEMES

<b>Figure 2.1</b>	Distribution of global energy production .....	5
<b>Figure 2.2</b>	Characteristic current-voltage curve of a solar cell .....	6
<b>Figure 2.3</b>	Types of electron-hole pair recombination .....	9
<b>Figure 2.4</b>	Efficiency potential for 1 <sup>st</sup> , 2 <sup>nd</sup> , and 3 <sup>rd</sup> generation solar cells .....	12
<b>Figure 2.5</b>	Charge transport through nanocrystal thin films .....	18
<b>Figure 3.1</b>	Experimental set-up for the hot injection method .....	27
<b>Figure 3.2</b>	Free-energy versus nuclei radius .....	31
<b>Figure 3.3</b>	Growth rate versus nanocrystal diameter .....	32
<b>Figure 3.4</b>	Chemical structures of typical ligands .....	37
<b>Figure 4.1</b>	TEM images of Cu <sub>2</sub> ZnSnS <sub>4</sub> nanocrystals .....	49
<b>Figure 4.2</b>	XRD pattern of Cu <sub>2</sub> ZnSnS <sub>4</sub> nanocrystals .....	50
<b>Figure 4.3</b>	UV-vis spectrum of Cu <sub>2</sub> ZnSnS <sub>4</sub> nanocrystals .....	51
<b>Figure S4.1</b>	TEM images and size distribution plots of Cu <sub>2</sub> ZnSnS <sub>4</sub> nanocrystals ..	60
<b>Figure S4.2</b>	SEM and EDS of Cu <sub>2</sub> ZnSnS <sub>4</sub> nanocrystals .....	60
<b>Figure S4.3</b>	TEM from EDS of Cu <sub>2</sub> ZnSnS <sub>4</sub> nanocrystals .....	61
<b>Figure S4.4</b>	XRD patterns versus aliquot time .....	61
<b>Figure S4.5</b>	High-resolution XPS of elements in CZTS .....	62
<b>Figure S4.6</b>	DTA plots of CZTS, Cu <sub>2</sub> SnS <sub>3</sub> , and ZnS nanocrystals .....	63
<b>Figure S4.7</b>	XRD of ZnS and Cu <sub>2</sub> SnS <sub>3</sub> nanocrystals .....	64
<b>Figure S4.8</b>	I-V plot of CZTS nanocrystal thin film .....	64
<b>Scheme 5.1</b>	Ligand exchange mechanism .....	72
<b>Figure 5.1</b>	SEM image of CZTS thin film .....	73

<b>Figure 5.2</b>	UV-vis of as-deposited and annealed CZTS thin films with ideal and copper-poor/zinc-rich stoichiometries . . . . .	74
<b>Figure 5.3</b>	J-V plots of the photocurrent response from as-deposited stoichiometric and Zn-rich thin films . . . . .	77
<b>Figure 5.4</b>	J-V plots of the photocurrent response from annealed stoichiometric and Zn-rich thin films . . . . .	78
<b>Figure 5.5</b>	IPCE and APCE measurements for Zn-rich CZTS thin films . . . . .	79
<b>Figure 5.6</b>	Absorption profiles for 473, 532 and 632 nm light . . . . .	81
<b>Figure 5.7</b>	IPCE as a function of film thickness from front or back illumination . . . . .	82
<b>Figure 5.8</b>	Plot of the IPCE for front and back illumination versus film thickness at 473, 532, and 632 nm light . . . . .	86
<b>Figure 5.9</b>	Steady-state photocurrent plotted as a function of light intensity . . . . .	84
<b>Table S5.1</b>	Molar ratios of precursors used in the synthesis of stoichiometric and zinc-rich CZTS nanocrystals . . . . .	96
<b>Figure S5.1</b>	TEM and size distribution of stoichiometric and Zn-rich CZTS nanocrystals . . . . .	96
<b>Figure S5.2</b>	XRD from stoichiometric and Zn-rich CZTS nanocrystal powders . . . . .	97
<b>Figure S5.3</b>	ATR-IR of CZTS films with and without ligand exchange . . . . .	97
<b>Figure S5.4</b>	SEM images of CZTS thin films before and after annealing . . . . .	98
<b>Figure S5.5</b>	XRD of CZTS thin films before and after annealing . . . . .	98
<b>Figure S5.6</b>	J-V plots of a CZTS thin film using a cobalt mediator . . . . .	99
<b>Table 6.1</b>	Compositional Analysis, lattice parameters and band gap energies of $\text{Cu}_2\text{ZnSn}(\text{S}_{1-x}\text{Se}_x)_4$ nanocrystals . . . . .	104
<b>Figure 6.1</b>	XRD pattern of $\text{Cu}_2\text{ZnSn}(\text{S}_{1-x}\text{Se}_x)_4$ nanocrystals with $0 \leq x \leq 1$ . . . . .	105
<b>Figure 6.2</b>	HR-TEM images of $\text{Cu}_2\text{ZnSn}(\text{S}_{1-x}\text{Se}_x)_4$ nanocrystals with $0 \leq x \leq 1$ . . . . .	106
<b>Figure 6.3</b>	Band gap energies plotted versus CZTS,Se composition . . . . .	107
<b>Figure S6.1</b>	Relationship between the (220/204) diffraction peak and lattice parameters $a$ and $c$ with composition . . . . .	115
<b>Figure S6.2</b>	TEM images of CZTS,Se nanocrystals with $0 \leq x \leq 1$ . . . . .	115
<b>Table S6.1</b>	Nanocrystal size distribution from XRD and TEM analysis . . . . .	116
<b>Figure S6.3</b>	UV-vis data from colloidal CZTS,Se nanocrystals . . . . .	117
<b>Figure S6.4</b>	Conductivity from CZTS,Se nanocrystal powders versus composition . . . . .	118
<b>Figure 7.1</b>	TEM and HR-TEM of $\text{Cu}_2\text{Se}$ nanocrystals . . . . .	125

<b>Figure 7.2</b>	Schematic and SEM image of Cu <sub>2</sub> Se nanocrystal thin film device . . .	127
<b>Figure 7.3</b>	Current-voltage measurement of Cu <sub>2</sub> Se nanocrystal thin film as a function of air exposure . . . . .	129
<b>Figure 7.4</b>	XRD patterns of Cu <sub>2</sub> Se nanocrystals as a function of air exposure . . .	130
<b>Figure 7.5</b>	Cu2p XPS spectra as a function of air exposure . . . . .	132
<b>Figure 7.6</b>	Se3d XPS spectra as a function of air exposure . . . . .	133
<b>Figure S7.1</b>	TEM images and size distribution of Cu <sub>2</sub> Se nanocrystals . . . . .	147
<b>Figure S7.2</b>	Current-voltage behavior of Cu <sub>2</sub> Se nanocrystal thin films as a function of time exposed to air . . . . .	148
<b>Figure S7.3</b>	High resolution XPS Cu2p region spectra of Cu <sub>2</sub> Se nanocrystals as a function of time exposed to air . . . . .	149
<b>Figure S7.4</b>	High resolution XPS Se3d region spectra of Cu <sub>2</sub> Se nanocrystals as a function of time exposed to air . . . . .	150
<b>Figure S7.5</b>	UV-vis spectra of Cu <sub>2</sub> Se nanocrystal thin films as a function of time exposed to air . . . . .	151
<b>Figure A1</b>	PEC data from as-deposited and annealed CZTS,Se thin films . . . . .	158

## CHAPTER 1

### INTRODUCTION

The primary theme of this dissertation is the synthesis and characterization of earth abundant, copper-based semiconducting nanocrystals for optoelectronic applications. A strong emphasis is placed on controlling the optical and electronic properties of the nanocrystals, as well as the charge transport through nanocrystal thin films, by means of composition tuning and surface chemistry treatments. This dissertation is written in the “journals format” style—which is accepted by the Graduate School at Colorado State University—and is based on three peer-reviewed publications that have appeared in *The Journal of the American Chemical Society* and *ACS Applied Materials and Interfaces*, as well as one manuscript that has recently been submitted to *The Journal of the American Chemical Society*. In order to create a context for these publications, Chapters 2 and 3 provide an overview of key concepts addressed, while the final chapter seeks to draw general conclusions and make connections.

Chapter 2 gives a brief explanation of the different types of solar cells, including 1<sup>st</sup>, 2<sup>nd</sup> and 3<sup>rd</sup> generation devices. More specifically, this chapter describes the basic operation of solar cells, as well as the parameters that govern their efficiency. Finally, as solar technology moves towards solution-based processing using nanocrystal inks, the

factors that affect charge transport in nanocrystal thin films are discussed. In order to tune the electronic properties and understand charge transport in the nanocrystal systems presented within, one must first start with high quality nanocrystals as the quality of such materials affects these properties. One way to reproducibly synthesize high quality nanocrystals is by the hot injection method, as described in Chapter 3. Three important parameters are necessary for the success of the hot injection method—precursors, ligands, and the injection and growth temperatures—which will be described in detail.

Chapter 4 is a communication—published in *The Journal of the American Chemical Society*—of one of the pioneering syntheses of  $\text{Cu}_2\text{ZnSnS}_4$  (CZTS) nanocrystals by means of the hot injection method. This synthesis was quite extraordinary because very few quaternary materials have been synthesized on the nanoscale. CZTS was chosen because it is a very promising earth-abundant and non-toxic material for photovoltaic applications. More importantly, it offers a high degree of tunability—with regard to optical and electronic properties—as compared to other promising binary materials.

Chapter 5, is based on a publication that appeared in *ACS Applied Materials and Interfaces*, which highlights this tunability by comparing stoichiometric CZTS nanocrystals with copper-poor/zinc-rich CZTS nanocrystals. Nanocrystal thin films of each stoichiometry were fabricated by the layer-by-layer dip-casting method. Photoelectrochemical characterization was used to determine the photovoltaic properties of each composition, as well as the effects of low temperature annealing. Furthermore, the charge transport properties in such devices were determined and the major loss mechanisms deduced. In this system the major loss mechanisms results from

recombination via the redox shuttle at the back contact as well as minority carrier diffusion.

The optical and electronic properties of CZTS were further tuned by introducing selenium into the synthesis of CZTS nanocrystals. Chapter 6 reports the synthesis and characterization of  $\text{Cu}_2\text{ZnSn}(\text{S}_{1-x}\text{Se}_x)_4$  (where  $0 < x < 1$ ), which has been submitted to *The Journal of the American Chemical Society*. In order for this synthesis to be achieved, the reactivity of the sulfur and selenium precursors had to be carefully controlled. Other parameters affecting the synthesis are also discussed. Furthermore, changes in the optical properties and conductivity are presented.

In many cases, in order to overcome the poor transport properties in nanocrystal thin films, these films are subject to high temperature annealing to sinter the nanocrystals together. This, unfortunately, affords a greater processing cost and limits large scale production, as well as introduces structural defects and carbon impurities from ligand decomposition. Therefore, Chapter 7 presents an alternative approach to increasing the charge transport properties in nanocrystal thin films of copper selenide,  $\text{Cu}_2\text{Se}$ . Emphasis is placed on using surface chemistry treatments to induce a solid-state transformation and enhance charge transport properties within the nanocrystal thin films.

Finally, Chapter 8 contains a concise summary of the work presented within this dissertation. The experimental results from all three systems—CZTS, CZTS,Se, and  $\text{Cu}_2\text{Se}$ —have been highlighted. Furthermore, a direction for future research within the area of nanocrystal thin film electronics has been proposed.

## CHAPTER 2

# ADVANCING SOLAR TECHNOLOGY: FUNDAMENTALS OF SOLAR CELLS AND THE KNOWLEDGE TRANSFER TOWARD SOLUTION-PROCESSED PHOTOVOLTAICS

### 2.1 Overview

With the ever-increasing energy demand there is a strong push toward the development and application of renewable energies. Solar power is one renewable energy source that is capable of producing enough energy to power the planet, hence we have seen an annual 30% increase in the solar market over the past few years. Despite such advances, solar energy has not been competitive with carbon-based fuels due to the costs associated with processing and material usage. The current solar market is dominated by silicon technology; however, in an effort to reduce the cost of solar technology, there has been a strong push towards thin film (<100  $\mu\text{m}$ ) solar cells. Thin film solar cells, otherwise known as 2<sup>nd</sup> generation devices, take advantage of materials with enhanced optical properties, which allow for less material usage, cheaper substrates, and decreased fabrication costs, while maintaining modest device efficiencies. Initiatives to develop solution-processed solar cells for further cost reduction are currently underway. Solution-processed devices offer the advantages of high throughput, efficient materials

usage, ambient processing temperatures and pressures, and flexibility of the substrate choice. However, in order to achieve efficiencies comparable to those in bulk thin film devices a second annealing step is typically required, limiting the cost-advantage and scalability. Therefore, in order to move forward with solution-processed devices, a better understanding of the interfacial device characteristics of the materials is necessary to optimize the design of the cell. Herein we introduce the fundamentals of solar cells, highlight the different types of solar cells, and discuss charge transport through solution-processed nanocrystal thin films.

## 2.2 Background of Solar Cells

Currently, annual world power consumption is 15 TW and is forecasted to increase to nearly 30 TW by 2050.<sup>1,2</sup> Of the current 15 TW being consumed, 80-90% is produced by burning fossil fuels, which could have a negative impact on our climate.<sup>3</sup> Therefore, to

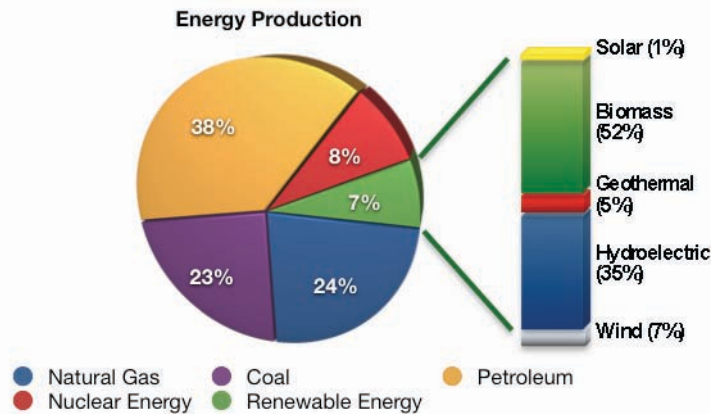


**Figure 2.1.** Distribution of global energy production according to the U.S. Energy Information Administration. Renewable energy has been expanded to show the different types and their distribution within the total energy produced by renewables.

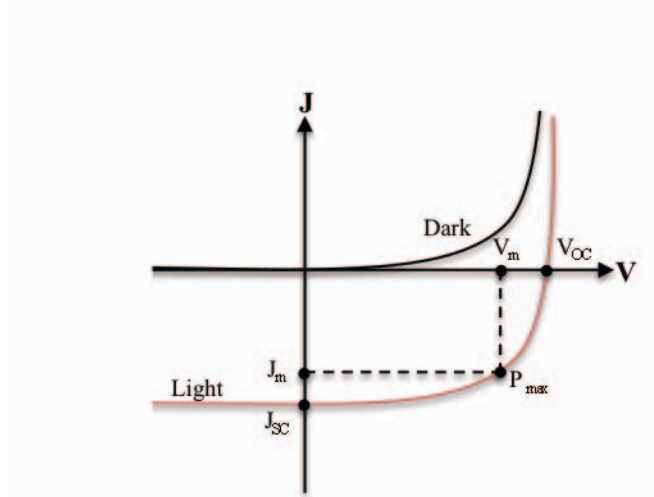


**Figure 2.2.** Characteristic current-voltage (J-V) curve of a solar cell.  $V_{OC}$  is the open circuit voltage,  $J_{SC}$  is the short-circuit current density,  $J_m$  and  $V_m$  are the optimized current density and voltage values, respectively, used to determine the maximum power,  $P_{max}$ , output of the solar cell. [2]

reduce our carbon footprint, alternative energy sources, including renewable energy, will be required. Today renewable energy accounts for less than 10% of the total energy produced worldwide, and that consists of hydroelectric, geothermal, biomass, wind and solar, Figure 2.1.<sup>4</sup> However, of those listed the only source capable of providing the extra 10-15 TW of energy needed by 2050 is solar energy. The amount of solar energy that hits the earth's surface in one hour is equivalent to the current total yearly energy consumption. Despite its potential to meet the clean energy demand, solar energy only makes up less than 0.01% of the total energy produced.<sup>4</sup> In order for solar energy to meet its potential as a clean energy source, new initiatives into the research and development of economically viable photovoltaics (PVs) need to be realized.<sup>1,4-7</sup>

Photovoltaic modules are made up of an absorber layer that is sandwiched between a metal back contact and a transparent front contact, typically a transparent conducting oxide (TCO).<sup>5</sup> Operation of a PV device is similar to that of a diode and can be illustrated by its current density-voltage (J-V) characteristics as shown in Figure 2.2. In

the dark, when negative or zero bias is applied there is minimal current flowing, but as a forward bias is applied, the cell behaves like a diode and current increases rapidly. However, under illumination, there is a vertical shift in the J-V curve and current flows at zero bias. The device should be operated under an applied bias (V) such that  $0 < V < V_{OC}$ , where  $V_{OC}$  is the open circuit potential—the voltage between the terminals when no current is flowing. Many parameters can be determined from J-V curves, such as  $V_{OC}$  and the short circuit current density,  $J_{SC}$ , which is the current drawn when the terminals are connected and the applied bias is zero.  $V_{OC}$  is determined by the band gap energy where  $V_{OC} < E_g / q$ , where  $q$  is the charge on the material, and  $J_{SC}$  is a function of the carrier density,  $n$ , carrier mobility,  $\mu$ , and the electric field,  $E$ , such that

$$J_{SC} = en\mu E \quad (2.1)$$

where  $e$  is the charge of an electron. The maximum power,  $P_{max}$ , one can get out of a solar cell or PV occurs when the current density and the voltage are maximized,  $J_m$  and  $V_m$ , respectively. The ratio of  $J_m V_m$  to  $J_{SC} V_{OC}$  is known as the fill factor, FF,

$$FF = \frac{J_m V_m}{J_{SC} V_{SC}} \quad (2.2)$$

which describes the squareness of the J-V curve and the performance of the device. One can then determine the efficiency,  $\eta$ , of the device by equation 2.3

$$\eta = \frac{P_{max}}{P_{in}} = FF \frac{J_{SC} V_{OC}}{P_{in}} \quad (2.3)$$

where  $P_{in}$  is the power put into the cell by the light. To compare PV devices,  $P_{in}$  is usually defined as air mass 1.5, AM1.5, and is equivalent to  $1000 \text{ W m}^{-2}$ .<sup>6,7</sup> PV device efficiency depends on three critical processes: i) charge carriers must be generated by absorbing sun light; ii) once the charge carriers are generated they must be separated; and iii) upon

charge carrier separation, the charge carriers must be transported to their respective contacts and collected to produce electricity.

The most important component in a solar cell is the absorber material, which converts photons into electricity by the photovoltaic effect.<sup>6</sup> When sunlight hits the absorber material, it excites an electron into the conduction band generating an electron-hole pair. For an ideal solar absorber, all incident photons with energy ( $h\nu$ ) greater than the absorber band gap ( $E_g$ ) are absorbed and promote exactly one electron per photon to the conduction band.

Once the charge carriers are generated, some driving force must subsequently separate them. This is typically achieved in most PV devices by forming a junction—between a metal and a semiconductor (Schottky junction) or between two oppositely doped semiconductors (p-n junction)—which introduces a built-in potential. There are two main routes for charge carrier separation: (i) diffusion to the junction based on carrier concentration profiles and (ii) drift, which is driven by a built-in electrostatic potential at the junction. After the charge carriers have been separated, they must be transported and extracted at the respective current collectors. The efficiency of carrier extraction is, however, limited due to recombination of the electron-hole pair.

Figure 2.3 illustrates three types of recombination that result in the loss of free carriers: i.) radiative recombination, ii.) Auger recombination, and iii.) non-radiative recombination.<sup>6,8</sup> Radiative recombination results in spontaneous and stimulated optical emission, which is an unavoidable process. The rate of radiative recombination is proportional to the product of the free carrier densities—the density of electrons multiplied by the density of holes. Auger recombination is also an unavoidable process

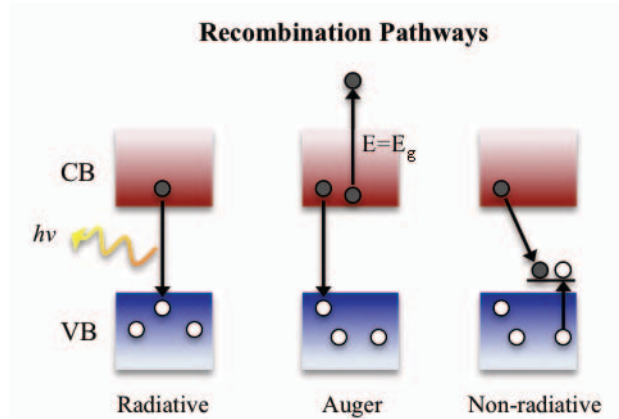


**Figure 2.3.** Three types of electron-hole pair recombination: radiative, Auger, and non-radiative. VB and CB refer to the valence and conduction bands, respectively. Radiative recombination results in photon emission. Auger recombination occurs when an excited charge carrier decays across the band gap while the kinetic energy of a second similar charge carrier is increased by an amount equal to the band gap energy. Non-radiative recombination typically occurs at trap sites, as depicted in the illustration. This figure has been adapted from reference [6].<sup>2</sup>

that involves the interaction between an excited electron or hole with a second similar carrier. This interaction causes a decay of one carrier across the band gap and an increase in the kinetic energy of the other carrier by an amount equal to the band gap energy. Ultimately, this extra energy is lost as heat. Unlike the first two, non-radiative recombination is an avoidable process and should be minimized. Non-radiative recombination occurs in real devices due to the presence of trap states, typically located at surfaces or interfaces where defects are the highest. Traps are localized whereas the charge carriers are delocalized, so the free carriers are effectively ‘trapped’ at these sites. The trap states are carrier specific, with states located near the valence band edge being donor states that trap holes and states near the conduction band being acceptor states that trap electrons. Once a carrier becomes trapped at a trap state, non-radiative recombination follows prohibiting carrier extraction. Therefore, minimizing interfacial

resistance and surface defects is key to minimizing non-radiative recombination, optimizing carrier diffusion lengths, and ultimately maximizing PV efficiency.

In 1961, Shockley and Queisser calculated the maximum theoretical power conversion efficiency for a range of band gap energies.<sup>6,9,10</sup> This calculation was based on certain criteria: i) exactly one  $e^-h^+$  pair is generated for every photon with  $h\nu > E_g$  absorbed; ii) the only loss mechanism is by radiative recombination; iii) all photogenerated charge carriers that survive radiative recombination are collected; and iv) detailed balance is assumed. Based on these criteria, Shockley and Queisser determined that a maximum efficiency of ~33% could be achieved using a material with an optimal band gap of 1.4-1.6 eV. Therefore, ideal choices are absorber materials that have band gap energies within this range, which ensures that a sufficient amount of the solar spectrum can be captured to generate charge carriers.

### **2.3 1<sup>st</sup> Generation Photovoltaic Devices**

Current silicon photovoltaic technology—the most common type of commercial PV modules—is rapidly approaching the Shockley-Queisser maximum predicted efficiency, providing 25% power conversion efficiency (PCE) in the laboratory and 15% PCE for commercial devices.<sup>11,12</sup> Silicon technology dominates the solar industry, with crystalline (x-Si), multicrystalline (mc-Si), and ribbon silicon making up about 94% of the solar market. Silicon technology dates back to 1954 when Bell Labs introduced the first solar cell demonstrating 6% efficiency. However it was not until the 1970's, when oil prices were on the rise, that photovoltaics became the subject of intense interest. Current understanding of the science governing solar cell technology is based on this time period

forward.<sup>6</sup> Single crystalline silicon solar cells are grown by the Czochralski process, where a single crystal is gradually formed by pulling a poly-crystalline rod through a molten zone. Silicon has the advantage of being easily doped p-type or n-type—during the growth process the material is doped p-type by introducing boron, while n-type doping with phosphorous is achieved post-synthesis by diffusion-doping onto the top of the wafer. This produces a homojunction at the p-n junction, which is a distinct advantage because it reduces the number of interface states. With the rapid advancement in silicon technology, the x-Si solar cell efficiency was on the rise.

However, silicon is not an ideal solar absorber. It has a non-optimal indirect band gap of 1.1 eV, a low absorption coefficient, which necessitates the need for a thick material, and hence requires high purity to allow for charge carrier transport which adds to the manufacturing cost.<sup>6</sup> Therefore, despite PCE values of commercial PVs being close to 75% of that measured in the lab, the cost of x-Si-based PV modules is  $\sim \$4/W_p$  ( $W_p$  = peak Watt, which is the power produced under peak solar illumination), a cost too high to compete with carbon-based fuels.<sup>3</sup> This cost is based off the sum of the manufacturing cost ( $\sim \$2.70/W_p$ ) and the installation costs, balance of systems costs (frames, inverters, battery storage, etc...), lifetime, and maintenance costs. The nomenclature is derived by dividing the capital cost ( $\$/m^2$ ) by the product of the efficiency ( $\eta$ ) and the standard value for peak power of AM 1.5 global ( $1000 W_p/m^2$ ).<sup>1,2,8,9</sup> With a DOE goal of  $\$0.33/W_p$ , initiatives to reduce the cost or increase the efficiency of PVs must be realized. Figure 2.4 addresses alternatives to this 1<sup>st</sup> generation silicon technology; 2<sup>nd</sup> generation technology focuses on reducing the module cost while maintaining moderate efficiencies, whereas 3<sup>rd</sup> generation technology is based on increasing the efficiency beyond the

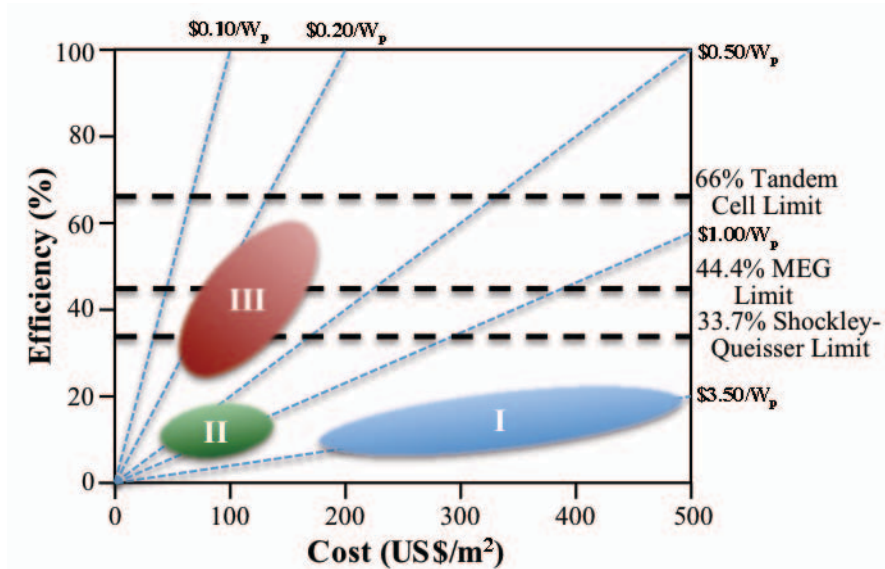


**Figure 2.4.** Efficiency potential for first (I), second (II) and third (III) generation solar cells plotted as a function of the module cost ( $\$/m^2$ ). The dashed blue lines correspond to the cost per watt ( $\$/W_p$ ). The dashed black lines are efficiency limits based on a single junction device (Shockley-Queisser), devices based off ‘hot carriers’ or multiple electron generation (MEG), and limits for tandem devices. This figure is adapted from reference [3].

Shockley-Queisser limit by mean of multiple electron generation.<sup>1,3-6,12,13</sup> *The contents discussed herein are focused on 2<sup>nd</sup> generation devices with aims of reducing the overall module cost.*

## 2.4 2<sup>nd</sup> Generation Photovoltaic Devices

Over 50% of the cost associated with Si-based PV modules comes from the fabrication of high quality crystalline Si, the amount of material used, and the module production.<sup>1</sup> Second generation photovoltaic devices aim to reduce this cost by using less expensive substrates, lowering processing expenses, and by incorporating absorber material(s) with ideal optical properties in effort to reduce the total material consumption and relax the requirement for high quality materials.<sup>1,3,5,6</sup> Unlike silicon, 2<sup>nd</sup> generation devices

incorporate materials with direct band gaps and high absorption coefficients (e.g., CdTe,  $\text{CuIn}_{1-x}\text{Ga}_x\text{Se}_2$  (CIGS), PbSe *and the materials of interest herein:  $\text{Cu}_2\text{ZnSnS}_4$  (CZTS),  $\text{Cu}_2\text{ZnSnSe}_4$  (CZTSe,) and  $\text{Cu}_2\text{Se}$ ).*<sup>2</sup> For these types of materials, the device performance is dictated by elemental composition, crystal phase, grain structure, and film density. In combination with inexpensive substrates such as glass, plastic, or metal foils, a typical thin film solar device is fabricated in a planar pn-junction, where the p- and n-type materials—having a total thickness of 1-10  $\mu\text{m}$ —are sandwiched between a transparent conducting oxide (TCO) and a metal contact.<sup>3,7</sup> Most typically, the absorber materials are p-type and therefore require an n-type material to create a junction for charge separation. CdS is one of the more common n-type layers, herein referred to as a window or buffer layer in these devices. Window layers are very thin wide-band-gap materials that allow light to pass through to the absorber, while also providing the built-in potential necessary to separate the charge carriers, minimize the resistive losses, and prevent short circuiting of the p-type absorber with the TCO. In addition, the window layer can reduce oxidation of the absorber surface. Commercial devices of this structure with either CdTe (FirstSolar) or CIGS (Nanosolar) as the absorber are currently being fabricated yielding PCE values near 10% and with a cost reduction to  $\sim \$1.25/\text{W}_p$  ( $\$0.98/\text{W}_p$  is associated with manufacturing costs) vs. Si-based cells.<sup>3,8</sup>

Unfortunately, the cost of 2<sup>nd</sup> generation devices still exceeds the goal set forth by the DOE of  $\$0.33/\text{W}_p$ . Such costs are directly attributable to low throughput, high-energy fabrication techniques (e.g., sputtering, electron beam evaporation and chemical vapor deposition that are performed at high temperature and/or in high vacuum), as well as the material extraction cost—In, Ga, and Te being rare and expensive materials.<sup>2,3,5</sup>

Therefore, there is a strong push towards solution processing of photovoltaic materials using liquid precursors or colloidal nanocrystals with earth-abundant constituents in efforts to further reduce overall production costs. Todorov et. al, recently reported fabrication of  $\text{Cu}_2\text{ZnSn}(\text{S},\text{Se})_4$  thin films by a liquid-processing method, involving a slurry of the corresponding binary metal chalcogenides with additional chalcogenide in hydrazine, followed by spin coating of the resultant slurry and annealing.<sup>13</sup> Remarkably, the authors were able to produce a 9.6% efficient lab-scale solar device, demonstrating the potential of solution-processed 2<sup>nd</sup> generation devices. In a similar report, Agrawal and co-workers reported a 7.2% efficient solar cell fabricated from  $\text{Cu}_2\text{ZnSnS}_4$  (CZTS) colloidal nanocrystals that were subject to thermal annealing in Se vapor.<sup>14</sup> Nonetheless, the methods above either involve the use of toxic chemicals, such as hydrazine, and/or require a subsequent annealing step (>500 °C). Due to the difference in vapor pressure of S, Se, and Sn versus Cu and Zn, annealing at these temperatures leaves little control over the resulting film composition, further increases the cost of production, and limits scalability. Therefore, there is still a need for low-cost, solution-based processing methods for photovoltaic devices.

## 2.5 Nanocrystal Thin Film Solar Cells

A new method for scaling up solar cell production is based on nanocrystal ‘inks’, a printable solution of nanocrystals, which can be used as deposited or alternatively be thermally annealed at low temperatures (temperatures <500 °C are all that is necessary due to nanocrystal size confinement) into larger grain thin films to make solar cells using 3-D arrays of photoactive nanocrystals.<sup>15</sup> Nanocrystal inks incorporate the *advantages of*

*being deposited under ambient temperature and pressure* via printing, or spin-, drop, or dip-casting. Furthermore, the synthesis of colloidal semiconductor nanocrystals by solution-based routes is well documented in the literature.<sup>15-21</sup> Most importantly, nanocrystals also exhibit size-tunable optical properties due to quantum confinement, allowing a wider range of potentially promising materials. For semiconducting PV nanocrystals, this was initially shown with cadmium chalcogenides by Alivisatos in 1996.<sup>22</sup> Here they observed that varying the growth time of CdS, CdSe, and CdTe nanocrystals resulted in a shift of the band gap energies, where the shorter growth times lead to larger band gap energies. This was further exploited in other binary (PbS, PbSe) and ternary (CuInS<sub>2</sub>, CuInSe<sub>2</sub>) PV nanomaterials in the coming years.<sup>23,24</sup> Another way to tune the band gap is by varying the resulting composition of the nanocrystals, as this allows for a more robust method when incorporating them into thin film device structures.<sup>25</sup> Unlike materials that are quantum confined, the optical and electronic properties of compositionally controlled solid-solutions do not change when deposited into a thin film, where electronic coupling can occur from close nanocrystal proximity or thermal annealing. This affect is demonstrated particularly in alloyed semiconductor nanocrystals where either the cations or anions are substituted. In Cd-based nanocrystals, the cadmium can be replaced by zinc to shift the band gap to the blue; alternatively, creating a mixed chalcogenide can shift the band gap from blue to red depending on the use of sulfur, selenium or tellurium, respectively.<sup>25</sup> Lead salts also exhibit this property, as demonstrated by Smith et al. using PbSe<sub>x</sub>Te<sub>1-x</sub>, PbS<sub>x</sub>Te<sub>1-x</sub>, and PbS<sub>x</sub>Se<sub>1-x</sub>.<sup>26</sup> Similarly, this is also feasible with ternary and quaternary nanomaterials.<sup>30-33</sup> Chiang and Guo separately demonstrated that in the CuInS<sub>2</sub> system, a mixed sulfur-selenium composition

varied the band gap from 0.98-1.46 eV.<sup>27,28</sup> Additionally, replacing some of the indium atoms with either gallium or boron shifted the band gap to the blue.<sup>29</sup> Creating a mixed chalcogenide such as  $\text{Cu}_2\text{ZnSn}(\text{S},\text{Se})_4$  also is predicted to change the band gap from 1.0 eV for Se-rich to 1.5 eV for S-rich; however this is yet to be shown experimentally in the literature (but we will demonstrate this in Chapter 6).<sup>30,31</sup>

There have been several reports of thin film nanocrystal solar cells based on  $\text{Cu}_2\text{S}$ ,  $\text{CdX}$  and  $\text{PbX}$  ( $\text{X}=\text{S},\text{Se},\text{Te}$ ), CIGS and CZTS that have not been post-deposition annealed. Wu et al. demonstrated a 1.6% efficient solar cell using  $\text{Cu}_2\text{S}$  nanocrystals in combination with CdS nanorods.<sup>32</sup> The Nozik group from NREL showed device efficiencies of 2.1% using PbSe nanocrystals in a Schottky junction design.<sup>33</sup> Later work replacing PbSe nanocrystals with PbS nanocrystals and incorporating ZnO as a n-type layer resulted in device efficiencies of 3%.<sup>34</sup> CZTS nanocrystals have been incorporated into heterojunction PV devices using CdS as an n-type layer, showing an efficiency of 0.23%.<sup>21</sup> Unfortunately, all of these nanocrystal devices have efficiency values that are inferior to those achieved in bulk thin films.

Despite such advantages brought forth by nanocrystals, the incorporation into efficient photovoltaic devices is still in its infancy and unlike diffusion in bulk thin films, diffusion of charge carriers through a nanocrystal thin film is a tortuous path. For opto-electronic applications, nanocrystals in a thin film must be coupled electronically, preferably without sintering, such that charge transport occurs over macroscale distances.<sup>8</sup> Ultimately, the transport properties in nanocrystal thin films are determined by the nanocrystal size distribution, morphological distribution, surface chemistry, and nanocrystal proximity as well as packing order within the thin films.<sup>6,35-37</sup> These

properties are related to the photovoltaic performance, where morphological features and trap states—formed at the nanocrystal interface or by elemental defects/vacancies—affect the open-circuit voltage, while carrier mobility is directly related to the short-circuit current. As these two terms determine the overall cell efficiency, it is important to understand how to tailor the individual nanocrystals and the nanocrystal thin films in order to optimize these values based on the carrier transport properties. Before carrier transport in nanocrystal thin films can be optimized, one must first gain knowledge of the factors governing the electron transfer between individual nanocrystals.

Precise control over the nanocrystal stoichiometry, size and shape is key for the carrier transport dynamics as it affects the disorder in site energies,  $\Delta\alpha$ .<sup>7</sup> When the size of a particular material is reduced to a size smaller than the Bohr radius of that particular material, confinement gives rise to discrete electron and hole states, rather than continuous energy bands.<sup>7,9,35</sup> The energy of these discrete states is determined by the morphology and size of the nanocrystal, scaling by  $1/r^2$  ( $r$  = particle radius); therefore, size distribution amongst a collection of nanocrystals results in the finite dispersion of orbital energies (Figure 2.5a), coined the disorder in sites energy.<sup>7,8</sup> Efficiency of electron transfer between adjacent particles is maximized when the orbital energies are equal (i.e., when the particle size distribution is small, Figure 2.5b), otherwise phonons are required to assist in the transport. For example, Liu et al. observed a size-dependent charge carrier mobility in nanocrystal thin films of PbSe.<sup>36</sup> They found that the electron and hole mobilities increased nearly two orders of magnitude as the nanocrystal sized increased from 3.1 to 6.1 nm. The electron mobility was decreased by increasing the PbSe nanocrystal size further from 6.1 to 8.6 nm, while the hole mobility continued to

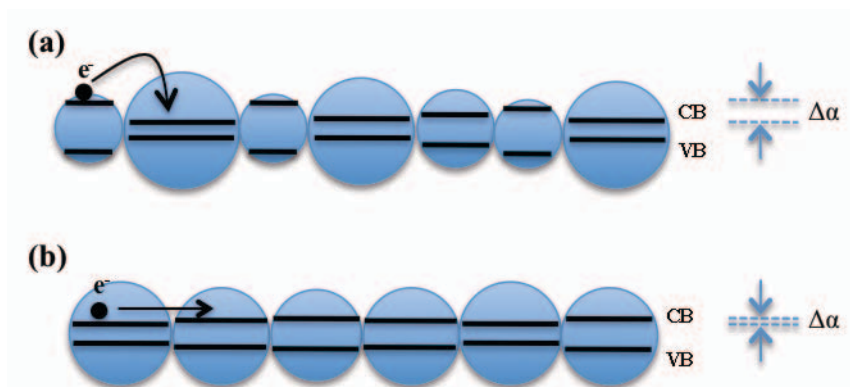


**Figure 2.5.** Illustration of charge transport through nanocrystal thin films in a sample containing (a) polydisperse size distribution and (b) monodisperse size distribution. The disorder in sites energy,  $\Delta\alpha$ , is larger for the polydisperse sample versus the monodisperse sample making charge transport more difficult in these films. This figure was adapted from reference [39].<sup>22</sup>

show a monotonic increase.<sup>36</sup> Therefore, there is a strong need for high quality nanocrystals with controlled size and morphology.

The size and morphology distribution of the nanocrystals plays a strong role in determining nanocrystal packing in thin films, further justifying the importance of controlling the nanocrystal size and shape. When two or more nanocrystals are brought into close proximity, coupling of the individual nanocrystals' wave functions occurs, which allows charges to 'tunnel' between the nanocrystals.<sup>7</sup> However, in order for the charges to travel between the individual nanocrystals, they must also travel through the interparticle medium (i.e., capping ligands), which acts as a tunneling barrier.<sup>8,35-37</sup> The tunneling rate of the charge carriers is inversely related to the separation between the nanocrystals as well as the type of interparticle medium. For this very reason, it is important to tune the nanocrystal spacing through replacement and/or removal of bulky capping ligands inherent in nanocrystal syntheses. Common capping ligands contain long hydrocarbon chains, which serve as insulating barriers. Replacing these ligands with short-chain ligands (e.g., ethylenediamine and ethanedithiol) and/or conducting

ligands (e.g, 1,2-benzenedithiol, 1,2-phenylenediamine, or  $\text{Sn}_2\text{S}_6^{4-}$ ) is one alternative route to annealing that is capable of minimizing the barrier for charge transport. In 2005, Murray and co-workers demonstrated a  $\sim 10$  order of magnitude increase in the conductance of PbSe nanocrystal thin films after treating the films with 1.0 M hydrazine in acetonitrile.<sup>38</sup> Similarly, Nozik and co-workers observed enhanced photovoltaic performance when their lead chalcogenide thin films were treated with 1,2-ethanedithiol by an in situ layer-by-layer ligand exchange method.<sup>33,39,40</sup> Additionally, Talapin and co-workers showed that replacing the inherent capping ligands on a variety of colloidal nanocrystals with metal chalcogenide ( $\text{Sn}_2\text{S}_6^{4-}$ ) ligands also lead to improved conductivities in nanocrystal thin films.<sup>41</sup>

## 2.6 Conclusions

Solar energy is capable of providing enough energy for the current world consumption in just one hour; however, it only makes up  $<0.01\%$  of the total energy production. Solar technology has not made a substantial impact on the energy market due to its limited device efficiencies and high cost. Solar cell efficiency is based on the ability of the device to generate charge carriers, separate the charge carriers and efficiently transport the charge carriers to be collected for electricity. Device costs are largely associated with the capital cost for making the device, coupled with the balance of systems cost, and annual maintenance costs. There are two approaches to make solar technology competitive with carbon-based fuels: i) reduce the fabrication costs while maintaining modest efficiencies, as accomplished by 2<sup>nd</sup> generation solar cells or ii) increase the device efficiency to offset the cost, the goal of 3<sup>rd</sup> generation devices. This chapter

focused primarily on 2<sup>nd</sup> generation devices and introduced the idea of using solution-processed solar cells to drive down the cost of PV devices. However, solution processed device efficiencies have not been comparable to bulk thin film solar cells made from the same material. Therefore, the fundamentals governing charge transport in solution-processed nanocrystal PV devices have been addressed, in efforts to rationally design more efficient solution-processed devices.

## 2.7 References

- (1) Slaoui, A.; Collins, R. T. *MRS Bull.* **2007**, *32*, 211-218.
- (2) Wadia, C.; Alivisatos, A. P.; Kammen, D. M. *Environ. Sci. Technol.* **2009**, *43*, 2072-2077.
- (3) Ginley, D.; Green, M. A.; Collins, R. *MRS Bull.* **2008**, *33*, 355-363.
- (4) Kamat, P. V. *J. Phys. Chem. C* **2007**, *111*, 2834-2860.
- (5) Habas, S.; Platt, H.; van Hest, M.; Ginley, D. *Chem. Rev.* **2010**, *110*, 6571-6594.
- (6) Nelson, J. *The Physics of Solar Cells*; Imperial College Press: London, 2003.
- (7) Talapin, D. V.; Lee, J.-S.; Kovalenko, M. V.; Shevchenko, E. V. *Chem. Rev.* **2009**, *110*, 389-458.
- (8) Hillhouse, H. W.; Beard, M. C. *Curr. Opin. Colloid Interface Sci.* **2009**, *14*, 245-259.
- (9) *Nanostructured and Photoelectrochemical Systems for Solar Photon Conversion*; Imperial College Press: London, 2008; Vol. 3.
- (10) Shockley, W.; Queisser, H. J. *J. Appl. Phys.* **1961**, *32*, 510-519.
- (11) Nozik, A. J. *Nano Lett.* **2010**, *10*, 2735-2741.
- (12) Kamat, P. *J. Phys. Chem. C* **2008**, *112*, 18737-18753.
- (13) Todorov, T. K.; Reuter, K. B.; Mitzi, D. B. *Adv. Mater.* **2010**, *22*, E156-E159.
- (14) Guo, Q.; Ford, G. M.; Yang, W.-C.; Walker, B. C.; Stach, E. A.; Hillhouse, H. W.; Agrawal, R. *J. Am. Chem. Soc.* **2010**, *132*, 17384-17386.
- (15) Panthani, M. G.; Akhavan, V.; Goodfellow, B.; Schmidtke, J. P.; Dunn, L.; Dodabalapur, A.; Barbara, P. F.; Korgel, B. A. *J. Am. Chem. Soc.* **2008**, *130*, 16770-16777.
- (16) Guo, Q.; Hillhouse, H. W.; Agrawal, R. *J. Am. Chem. Soc.* **2009**, *131*, 11672-11673.

- (17) Peng, X. G.; Manna, L.; Yang, W. D.; Wickham, J.; Scher, E.; Kadavanich, A.; Alivisatos, A. P. *Nature* **2000**, *404*, 59-61.
- (18) Peng, Z. A.; Peng, X. *J. Am. Chem. Soc.* **2002**, *124*, 3343-3353.
- (19) Riha, S. C.; Parkinson, B. A.; Prieto, A. L. *J. Am. Chem. Soc.* **2009**, *131*, 12054-12055.
- (20) Shavel, A.; Arbiol, J.; Cabot, A. *J. Am. Chem. Soc.* **2010**, *132*, 4514-4515.
- (21) Steinhagen, C.; Panthani, M. G.; Akhavan, V.; Goodfellow, B.; Koo, B.; Korgel, B. A. *J. Am. Chem. Soc.* **2009**, *131*, 12554-12555.
- (22) Alivisatos, A. P. *Science* **1996**, *271*, 933-937.
- (23) Murphy, J.; Beard, M.; Norman, A.; Ahrenkiel, S.; Johnson, J.; Yu, P.; Micic, O.; Ellingson, R.; Nozik, A. *J. Am. Chem. Soc.* **2006**, *128*, 3241-3247.
- (24) Moreels, I.; Lambert, K.; Smeets, D.; De Muynck, D.; Nollet, T.; Martins, J. C.; Vanhaecke, F.; Vantomme, A.; Delerue, C.; Allan, G.; Hens, Z. *ACS Nano* **2009**, *3*, 3023-3030.
- (25) Regulacio, M. D.; Han, M.-Y. *Acc. Chem. Res.* **2010**, *43*, 621-630.
- (26) Smith, D. K.; Luther, J. M.; Semonin, O. E.; Nozik, A. J.; Beard, M. C. *ACS Nano* **2011**, *5*, 183-190.
- (27) Chiang, M.-Y.; Chang, S.-H.; Chen, C.-Y.; Yuan, F.-W.; Tuan, H.-Y. *J. Phys. Chem. C* **2011**, *115*, 1592-1599.
- (28) Guo, Q.; Ford, G. M.; Hillhouse, H. W.; Agrawal, R. *Nano Lett.* **2009**, *9*, 3060-3065.
- (29) Chen, L.-J.; Liao, J.-D.; Chuang, Y.-J.; Fu, Y.-S. *J. Am. Chem. Soc.* **2011**, *133*, 3704-3707.
- (30) Riha, S. C.; Parkinson, B. A.; Prieto, A. L. *Manuscript in preparation* **2011**.
- (31) Chen, S.; Walsh, A.; Yang, J.-H.; Gong, X. G.; Sun, L.; Yang, P.-X.; Chu, J.-H.; Wei, S.-H. *Phys. Rev. B* **2011**, *83*, 125201.

- (32) Wu, Y.; Wadia, C.; Ma, W.; Sadtler, B.; Alivisatos, A. *Nano Lett.* **2008**, *8*, 2551-2555.
- (33) Luther, J. M.; Law, M.; Beard, M. C.; Song, Q.; Reese, M. O.; Ellingson, R. J.; Nozik, A. J. *Nano Lett.* **2008**, *8*, 3488-3492.
- (34) Luther, J.; Gao, J.; Lloyd, M.; Semonin, O. E.; Beard, M.; Nozik, A. *Adv. Mater.* **2010**, *22*, 3704-3707.
- (35) Geyer, S.; Porter, V. J.; Halpert, J. E.; Mentzel, T. S.; Kastner, M. A.; Bawendi, M. G. *Phys. Rev. B* **2010**, *82*, 155201.
- (36) Liu, Y.; Gibbs, M.; Puthussery, J.; Gaik, S.; Ihly, R.; Hillhouse, H. W.; Law, M. *Nano Lett.* **2010**, *10*, 1960-1969.
- (37) Sargent, E. H. *Nat. Photonics* **2009**, *3*, 325-331.
- (38) Talapin, D. V.; Murray, C. B. *Science* **2005**, *310*, 86-89.
- (39) Law, M.; Luther, J. M.; Song, Q.; Hughes, B. K.; Perkins, C. L.; Nozik, A. J. *J. Am. Chem. Soc.* **2008**, *130*, 5974-5985.
- (40) Luther, J. M.; Law, M.; Song, Q.; Perkins, C. L.; Beard, M. C.; Nozik, A. J. *ACS Nano* **2008**, *2*, 271-280.
- (41) Kovalenko, M. V.; Scheele, M.; Talapin, D. V. *Science* **2009**, *324*, 1417-1420.

## CHAPTER 3

### TOWARD THE SYNTHESIS OF HIGH QUALITY NANOCRYSTALS: AN OVERVIEW OF THE HOT INJECTION METHOD

#### **3.1 Overview**

Nanomaterials have been receiving increased attention due to their tunable optical and electronic properties, colloidal stability, as well as their incorporation into solution processed optoelectronic devices. However, the realization of efficient devices is still lacking due to poor electron transport properties in nanocrystal thin films. As mentioned in the previous chapter, electron transport in nanocrystal thin films is strongly dependent on the quality of the nanocrystals—size and shape distribution, surface chemistry and interparticle medium. Therefore, one prerequisite to a more complete understanding of electron transport in nanocrystal thin films is the synthesis of high quality nanocrystals. A synthesis route, known as the hot injection method, is one well-established synthetic method for the synthesis of high quality nanocrystals. The hot injection method is based on the theory of nucleation and growth, which in this method is largely controlled by three parameters: i) precursors, ii) ligands, coupled with the metal to ligand concentration ratio, and iii) temperature. The purpose of this chapter is to introduce the hot injection method and provide a brief history of the synthetic method towards high quality

nanomaterials. More specifically, this chapter highlights the versatility of the hot injection method for synthesizing a variety of binary and multinary semiconductor nanomaterials used in optoelectronic applications. Furthermore, nucleation and growth is discussed to provide a conceptual background for why the hot injection method is capable of producing high quality nanocrystals.

### **3.2 Background**

With technological advances toward making increasingly smaller electronic devices, the development of semiconducting materials on the nanoscale has been a focal point of scientific research.<sup>1-4</sup> Nanomaterials offer distinct advantages over their bulk counterparts mainly due to their tunable electronic, optical and magnetic properties, along with their ease of solution processing.<sup>1,4</sup> More importantly, the effort to reduce our dependence on carbon-based fuels, as well as our carbon footprint, has driven research towards renewable energy, and more specifically, solar power.<sup>5,6</sup> The characteristics of nanomaterials are especially crucial for photovoltaic applications, which rely on semiconducting materials with optimal band gaps that absorb the entire solar spectrum. Currently, the cost associated with manufacturing solar devices is too high to compete with carbon-based fuels.<sup>5,6</sup> As mentioned in Chapter 2, solution processed nanomaterials, in principle, have the potential to remedy this issue and make photovoltaic devices more economically viable. Nanocrystals, for example, can be either ink jet printed, spin-, drop-, dip- or spray-cast onto virtually any substrate, offering a significant cost reduction with regards to processing and flexibility in substrate choice.<sup>5,7,8</sup> Unfortunately, the incorporation of nanomaterials into efficient thin film photovoltaic and other electronic

devices still remains a challenge, as their efficiency is ultimately limited by poor charge transport through the nanocrystal thin film.<sup>9,10</sup> Therefore, a strong emphasis must be placed on the fundamental understanding of charge transport in nanocrystal thin films.

Charge transport in nanocrystal thin films, as alluded to in Chapter 2 of this dissertation, is strongly dependent on the quality of the nanocrystals. The size and morphology distribution, composition, surface chemistry and interparticle medium all play a crucial role in determining how well charge carriers propagate through the nanocrystal thin film.<sup>1,11-13</sup> To understand the physics that govern charge transport, one must start with high quality nanocrystals made by a controllable and reproducible synthesis method, so that one can determine the properties inherent to the nanocrystals apart from properties that arise due to variation in the sample quality. In order to achieve this, the synthetic method must adhere to the following requirements: i) be a solution-based route to allow for ease of processing of the resulting nanocrystals; ii) be reproducible for a large quantity of uniformly sized nanocrystals; iii) be applicable to a wide range of semiconducting materials; and iv) use simple experimental equipment and readily available chemicals to allow for low cost.<sup>3,4,14</sup> One such synthetic method meeting the above criteria is referred to as the hot injection method. Figure 3.1 is a pictorial illustration of the hot injection method, which involves the rapid injection of a ‘cold’ solution of precursors into a hot (~300 °C) liquid.<sup>2,3,14</sup>

### **3.3 A Brief History Detailing the Hot Injection Method**

In 1988, Steigerwald et al. demonstrated that growing CdSe in the presence of surfactants resulted in the arrested precipitation of CdSe nanoclusters with more

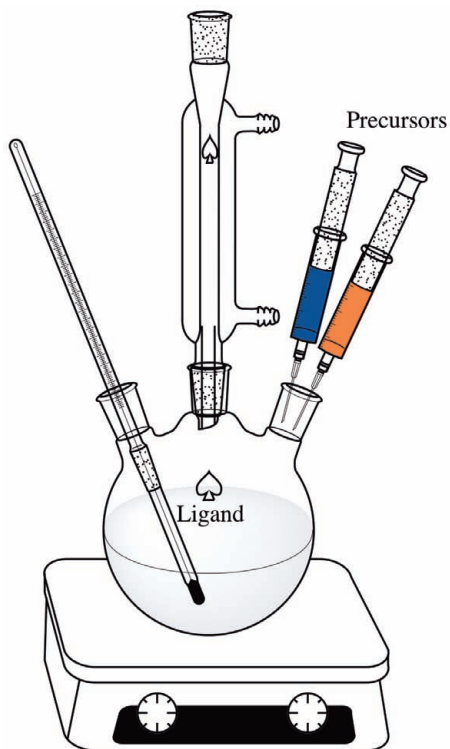


**Figure 3.1.** Typical experimental set-up for the hot injection method. The ligand, which also serves as the solvent, is heated in a 3-neck round-bottom flask equipped with a reflux condenser, stir bar and thermocouple. The flask is attached to a Schlenk line to provide an inert atmosphere. The precursors are rapidly injected into the ligand creating a burst of nucleation, followed by nanocrystal growth.

controlled size distribution due to surface passivation by organoselenides.<sup>15</sup> The concept of using long-chain organics to control the size distribution of nanocrystals was the inspiration for the hot injection method. The history of the hot injection method dates back to 1993 with the pioneering work by Murray et al. towards the synthesis of high quality CdE (E = S, Se, Te) nanocrystals.<sup>14</sup> In their synthesis, highly reactive dimethylcadmium ( $\text{Cd}(\text{CH}_3)_2$ ) and elemental selenium were separately mixed with TOP (trioctylphosphine), while TOPO (trioctylphosphine oxide) was heated to 300 °C in a 3-neck flask. The Cd and Se precursors were combined and rapidly injected into the TOPO flask, initiating nucleation and dropping the temperature to 180 °C. The growth temperature was between 230-260 °C, and aliquots were taken at 5-10 minute intervals.

Based on the time of the aliquot, the nanocrystal size could be varied from 1.2 nm–11.5 nm. The authors used size selective precipitation to narrow the size distribution, which initially was around 10%. This was achieved by suspending the nanocrystals in 1-butanol and then adding methanol dropwise until the solution becomes turbid. The solution was centrifuged and the precipitate collected—the precipitate consisted of the largest nanocrystals. The process was repeated until no size sharpening was observed in the optical absorption spectra. A few years later, Peng et al. described a way to focus the size distribution without the need for size selective precipitation.<sup>16</sup> In this work, they used a similar preparation method as Murray et al., where TOPO was heated in a 3-neck flask to 360 °C and a solution of Se, Cd(CH<sub>3</sub>)<sub>2</sub>, and TBP (tributylphosphine) was rapidly injected. The growth temperature was lowered to 300 °C and aliquots were taken at various time intervals. After 190 min, a second solution of Se, Cd(CH<sub>3</sub>)<sub>2</sub> and TBP was slowly injected into the reaction mixture to increase the monomer concentration and “shift the critical nuclei radius”. The details of these focusing/defocusing steps will be discussed in greater detail later within this chapter.

The same authors showed that adjusting the precursor reactivity and the resulting monomer concentration could also help control the morphology, much like it controlled the size distribution.<sup>17</sup> At this time TOPO was the most common ligand used in these reactions; however, it was quickly realized that results varied batch to batch when using technical grade TOPO and did not work well with purified TOPO. The impurities were determined to be alkylphosphonic acids, which were found to play a crucial role in the synthesis. Therefore, Peng et al. controllably added hexylphosphonic acid (HPA) as a way to tune the morphology. They found that higher HPA concentrations lead to nanorod

formation and explained this phenomenon by an increase in the growth rate and preferential binding by the HPA to certain crystallographic planes. In a follow up paper by the same group, they extended this to the synthesis of a variety of shapes, including rods, arrows, teardrops and tetrapods.<sup>18</sup> They determined that varying the HPA concentration lead to dots, rods and arrows, while multiple injections and changes in the injection rate could tune the aspect ratio, creating teardrops and tetrapods.

The synthesis of Cd-chalcogenides by means of the hot injection synthesis has been well documented in the literature, and therefore, is a high quality model system for the creation of a multitude of nanocrystal sizes and morphologies.<sup>9,14,16,17,19-22</sup> Furthermore, this synthetic method has been extended to the synthesis of a other II-VI materials and a multitude of binary and multinary chalcogenides, highlighting the versatility of the hot injection method. In 1998, Peng et al. demonstrated that InAs nanocrystals could be prepared using indium chloride and tris(trimethylsilyl) arsine in TOP, which was subsequently injected into TOP at 300 °C.<sup>16</sup> Lead chalcogenide nanocrystals have been prepared using lead salts, oleic acid and a non-coordinating solvent such as 1-octadecene, TOP and elemental chalcogenides.<sup>23-26</sup> Copper sulfides and selenides have been prepared by similar methods using TOPO, oleylamine (OLA), TOP, metal salts and elemental chalcogenides.<sup>27-29</sup> Iron disulfide nanocrystals were synthesized by Law and co-workers using iron chloride, elemental sulfur, diphenyl ether, and octadecylamine.<sup>30</sup> More recently, the hot injection method has also been used in the synthesis of more complex multinary chalcogenides, including  $\text{CuIn}(\text{S},\text{Se})_2$  (CIS),  $\text{Cu}(\text{In}_{1-x}\text{Ga}_x)(\text{S}_{1-x}\text{Se}_x)_2$  (CIGS), and  $\text{Cu}_2\text{ZnSn}(\text{S},\text{Se})_4$  (CZTS).<sup>10,31-36</sup> The versatility of the hot injection method has been demonstrated for a wide range of materials; however, other than the Cd-chalcogenide

nanocrystals, the system details are not well understood for many of these materials. As more and more complex materials are synthesized (i.e., CIS, CIGS, CZTS), a much more in depth understanding of the synthetic conditions will be required given that the nanocrystal composition is also a competing factor along with size and morphology.

### **3.4 Nucleation and Growth**

The ability to synthesize high quality nanomaterials by the hot injection method has often been explained in the literature by the theory of nucleation and growth. The mechanistic literature regarding the theory of nucleation and growth with respect to nanocrystalline materials dates back to 1950 and the classical work of LaMer towards the synthesis of monodisperse sulfur hydrosols.<sup>37</sup> LaMer found that controlling the amount of sulfur in solution determined the nucleation rate, while the temperature, concentration of sulfur post nucleation, and the diffusion of sulfur were significant for controlling the growth of the nuclei. In this theory, the nuclei are treated as having a planar surface and the same density as the bulk material at equilibrium. Therefore, it is doubtful that this classical nucleation theory can be quantitatively applied to that of nucleation and growth in the hot injection method.<sup>3,38</sup> This is because nuclei formed by the hot injection method are far from equilibrium. They consist of only a few hundred atoms, have a sharp radius of curvature, and are coated with a monolayer average of surfactant, which affects the surface free energy.<sup>38,39</sup> Because the hot injection method is such a complex system, however, it is commonly accepted in the literature to use this theory to conceptually explain experimental observations.

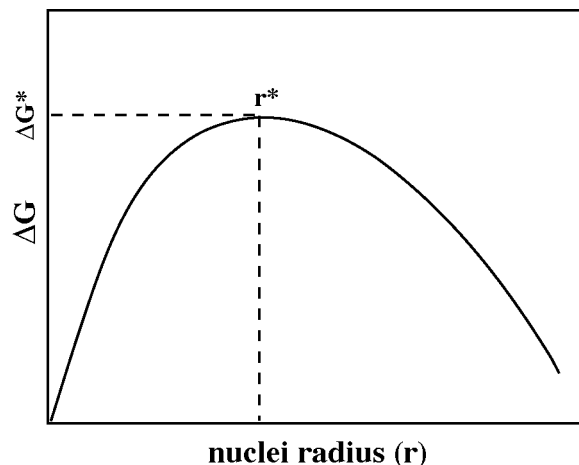


**Figure 3.2.** Free energy,  $\Delta G$ , diagram as a function of the nuclei radius. The maximum free energy,  $\Delta G^*$ , corresponds to the critical radius,  $r^*$ . This figure has been adapted from reference [25].

Nucleation refers to the formation of a discrete particulate of a different phase in a previously single-phase system.<sup>40</sup> In the hot injection method, the rapid injection of precursors causes a substantial increase in monomers—reactive species, formed by precursor decomposition or reaction—resulting in an abrupt supersaturation. This supersaturation is reduced by a short burst of nucleation.<sup>14,16,39</sup> The theory predicts that there is some minimal stable nuclei size, termed the critical nuclei radius,  $r^*$ , where nuclei have an equal chance to decompose to the reactants or grow with the addition of monomers left in the reaction flask. This can be described in terms of free energy and is illustrated in Figure 3.2.<sup>2,3,38</sup> In a supersaturated solution of monomers, the monomers combine to form small, unstable clusters of increasing free energy,  $\Delta G$ , which is a function of the radius,  $r$ . The maximum free energy,  $\Delta G^*$ , occurs at the ‘transition state’ where there is equal probability for the nuclei to decompose or grow and that corresponds to  $r^*$ . The depletion of monomers below the critical supersaturation threshold is a result of nucleation and the sudden drop in temperature—a consequence of the injection of

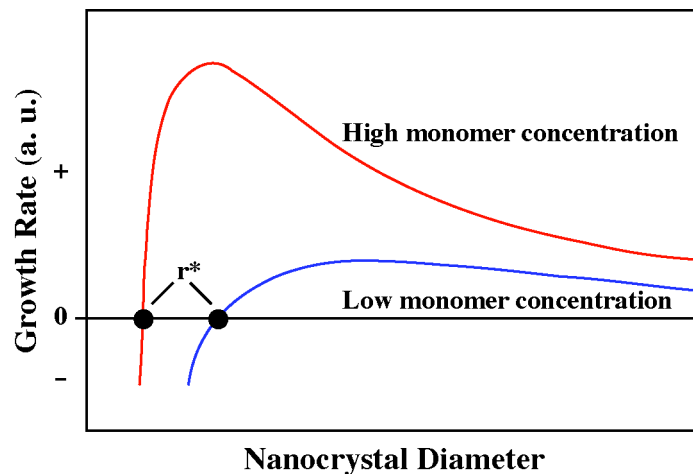


**Figure 3.3.** Growth rate as a function of size at high (red trace) and low (blue trace) monomer concentrations. At high monomer concentrations, the critical radius is small, and smaller particles grow faster than larger particles, allowing for size focusing. With low monomer concentrations, the critical radius is larger than at high monomer concentrations. Smaller nanocrystals are depleted at the expense of the larger ones growing, resulting in a defocusing of the size distribution.

lower temperature precursors—prevents further nucleation events from occurring, at which point growth begins.

Growth is defined as the process whereby additional monomer left in the reaction flask deposits on the nuclei, resulting in a size increase. The final size depends on three variables: i) the number of nuclei formed, ii) the amount of monomer left in the reaction flask, and iii) the diffusion coefficient.<sup>37</sup> Assuming a homogeneous distribution of monomer throughout the reaction flask, the amount of monomer added to each nucleus is equal to

$$\frac{1}{n}C^*$$

where  $n$  is the number of nuclei and  $C^*$  is the monomer concentration post-injection. The total monomer concentration left post-nucleation is equal to the difference between the initial monomer concentration and that consumed during nucleation. Figure 3.3 illustrates

growth rates as a function of high (red) and low (blue) monomer concentrations. If the monomer concentration is high, there is a large difference between the chemical potential of the bulk solution versus in the diffusion sphere—the area immediately surrounding the nuclei—so diffusion to the nuclei surface is fast and growth is therefore fast. This can sometimes lead to anisotropic morphologies because higher energy facets will have preferential growth.<sup>17,21</sup> However, smaller crystallites larger than  $r^*$  will grow at a faster rate than larger particles due to higher surface energy, which allows for size focusing that leads to a narrow size distribution.<sup>16</sup> At low monomer concentrations, however, the chemical potential gradient between the bulk solution and the diffusion sphere is small, which means the diffusion to the surface of the nuclei is much slower. This slower growth rate usually results in round crystals that are at equilibrium because the additional species can rearrange on the surface to reduce surface energy.<sup>17,18,21</sup> Finally, the diffusion coefficient is another determining factor for growth, and is directly related to the growth temperature and indirectly related to the solution viscosity.<sup>37</sup> The diffusion of monomers to the nuclei surface is also dependent on the chemical potential gradient between the bulk solution and that in the diffusion sphere.

### **3.5 Hot Injection Parameters Affecting Nucleation and Growth**

***Precursors.*** Three key parameters can be manipulated to control nucleation and growth and obtain high quality nanocrystals by the hot injection method, namely the precursors, the ligands (or surfactants), and the temperature.<sup>3,39</sup> While each of these will be considered as an independent variable here, they are all interrelated in many regards. To start, the rate of nucleation is directly proportional to the concentration of monomer

and the degree of supersaturation.<sup>4,17</sup> The precursor reactivity can determine the rate at which the precursors react or decompose to form the monomer species, which directly affects the monomer concentration. A higher monomer concentration leads to fast nucleation and results in a large amount of smaller critical nuclei; a low monomer concentration slows the nucleation producing a smaller amount of larger critical nuclei, which as discussed above can lead to a larger size distribution.<sup>4</sup> For this reason, the precursors need to rapidly decompose or react to yield a supersturation of monomers immediately following injection.<sup>39</sup> Simple molecules that have leaving groups that readily detach are optimal choices for precursors. For example, Urban et al. have shown that a variation in the reactivity of different lead precursors can lead to different nanocrystal sizes.<sup>26</sup> When they used lead acetate,  $\text{Pb}(\text{OAc})_2$ , with a small amount of oleic acid, versus using a  $\text{Pb}(\text{OAc})_2$  with a large amount of oleic acid, the nucleation and growth kinetics were affected. Using a large amount of oleic acid leads to the complexation of oleic acid with lead to form lead oleate, which is more stable and reacts more slowly than  $\text{Pb}(\text{OAc})_2$ . The resulting nanocrystals were much larger with lead oleate, compared with those made using only a small amount of oleic acid, which the authors attributed to a smaller number of larger nuclei formed. In a related example, it has been demonstrated by Peng et al. that there is a difference in the reactivity of cationic and anionic precursors.<sup>21</sup> The formation of Cd-TDPA and TBPSe occurs when tetradecylphosphonic acid (TDPA) and TBP are used in the synthesis of CdSe nanocrystals. Cd-TDPA is more stable and therefore much slower to react than TBPSe. By increasing the ratio of Cd-TDPA to TBPSe, they were able to achieve faster nucleation kinetics.

The concentration of monomers also affects the growth kinetics as observed by Peng<sup>16,17</sup> and Manna.<sup>18</sup> The authors suggested that a high monomer concentration led to fast growth conditions producing either anisotropic shapes or monodisperse nanocrystals. With a low monomer concentration left after nucleation, a broad size distribution resulted, which they attributed to Ostwald ripening. It is often reported that Ostwald ripening occurs because as the monomer concentration decreases with an increase in the growth time, the critical radius shifts to larger values,  $r^*$ .<sup>39</sup> Smaller nanocrystals in solution, with  $r < r^*$ , will begin dissolving, while larger particles continue to grow at their expense, termed size defocusing. In order to circumvent this issue, and as described earlier, a second injection of monomers will increase the monomer concentration and shift  $r^*$  back to smaller values and size focusing will resume.<sup>16</sup> Peng et al. demonstrated that the size of the nanocrystals could be focused and defocused by adjusting the concentration of monomers.<sup>16,17</sup> Initially, the nanocrystals had a large size distribution of 20%; with a high monomer concentration, smaller nanocrystals grew faster than larger ones, and over a period of 22 minutes the size was focused and the distribution reduced to 7.7%. The authors observed that after 22 minutes, the monomer concentration dropped as a result of growth, the size began to defocus, as a result of a shift in  $r^*$ , and the size distribution increased to 10.9%. A second injection supplied additional monomers to the growth medium, increasing the monomer concentration, and the size distribution was again reduced to 8.7%. Peng et al. also demonstrated an affect of lowering the initial monomer concentration on the time before defocusing occurred; this was achieved by changing the ratio of Cd-TDPA to TBPSe. When the ratio was 1.4:1, it took 22 minutes before defocusing occurred. Increasing the ratio to 1.9:1 increased the time to hours

before defocusing dominated, and decreasing the ratio to 1.1:1 resulted in a rapid occurrence of size defocusing. Similar results were observed by Manna et al., when they changed the injection volume of precursors for the synthesis of anisotropic CdSe morphologies.<sup>18</sup> They found that increasing the injection volume lead to an increase in the growth rate. Because higher energy facets grow faster, they were able to produce rods with very high aspect ratios.

All of the above examples are based on binary semiconducting materials with the elements being in their most common oxidation state. The precursor reactivity is less influential on the composition as it is on the size and morphology, as a result. However, as the hot injection method is applied to other binary, ternary and quaternary materials, where the metals have multiple oxidation states possible, the precursor reactivity and relative concentration becomes even more important. Balancing the precursor reactivity is critical to obtain the desired composition and minimize the formation of impurities, such as the formation of binary and ternary impurities in a quaternary material synthesis.

**Ligands.** As the concentration of monomers affects the nucleation and growth kinetics, it is important to note that the ligands affect the monomer concentration due to their interaction with the precursors.<sup>3,23</sup> More specifically, as the concentration of ligand is increased, they either coordinate with the precursors forming more stable precursors or reduce the overall monomer concentration. The concentration of nuclei decreases, as a consequence of a lower nucleation rate, creating larger nuclei.<sup>3</sup> One example, as mentioned above is the complexation of oleic acid and lead to form a more stable lead oleate, which slowed the nucleation kinetics.<sup>26</sup> Another example is the affect of chain length on the nucleation rate. Dai et al. observed that TBPSe was less stable and reacted

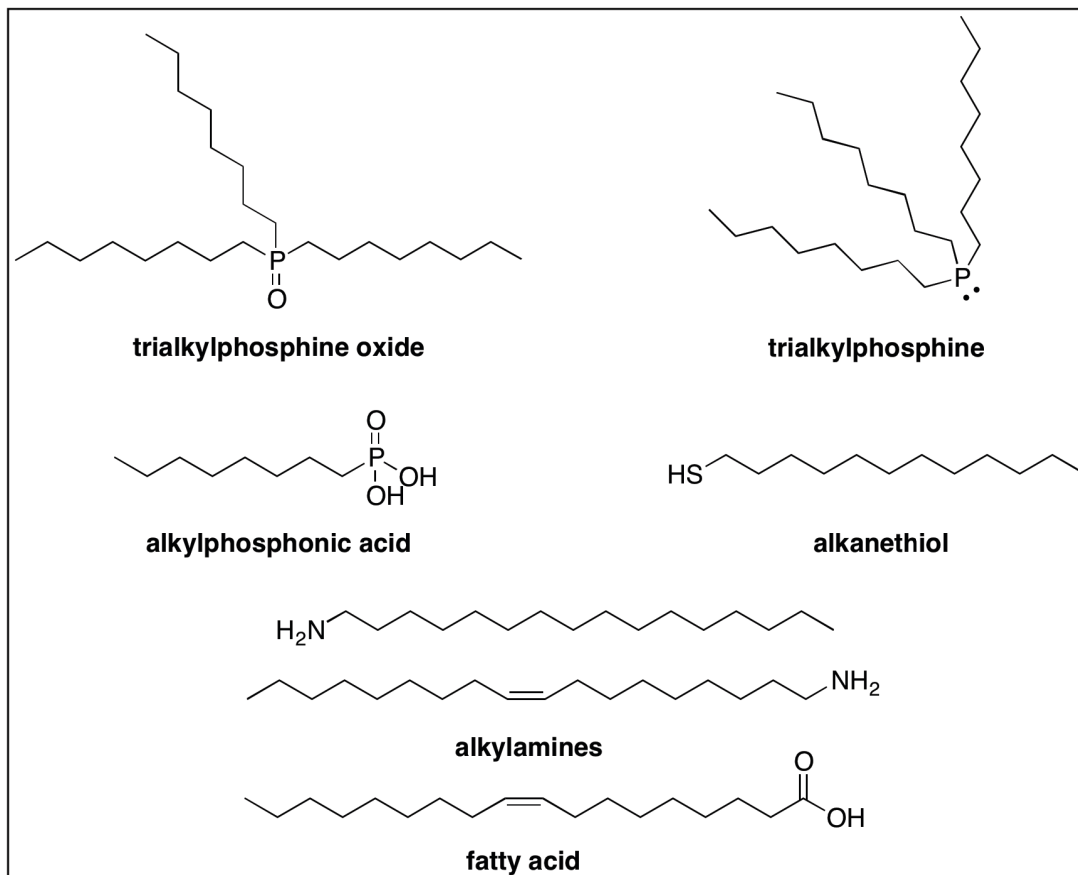


**Figure 3.4.** Chemical structures of typical ligands used in the hot injection synthesis method. Going from top to bottom, left to right, the ligands illustrated are trioctylphosphine oxide (TOPO), trioctylphosphine (TOP), octylphosphonic acid (OPA), dodecanethiol (DDT), hexadecylamine (HAD), oleylamine (OLA), and oleic acid (OA).

faster than TOPSe, creating smaller nanocrystals as a consequence of the increase in the number of nucleation events.<sup>23</sup>

In addition to affecting the nucleation rate, the growth rate can be influenced by not only the ligand to monomer concentration but also by the type of ligand. Figure 3.4 shows typical ligands containing coordinating head groups and generally hydrophobic tails, which fall into the following categories: i) alkylphosphine oxides, ii) alkylphosphines, iii) alkylphosphonic acids, iv) alkylamines, v) alkanethiols, and vi) fatty acids.<sup>4,39,41,42</sup> TOPO is the most commonly used surfactant in nanocrystal synthesis by the

hot injection method and was used in the pioneering hot injection synthesis by Murray et al.<sup>43</sup> TOPO has several advantages, including a high boiling point, allowing for higher temperatures for precursor decomposition. It is robust and its long chains and sterics help with morphology, size and solubility in nonpolar solvents. Binding typically occurs through the lone pair on the oxygen, which is donated to the unsaturated surface metal atom.<sup>41</sup> However, it was found that in technical grade TOPO, alkylphosphonic acids are a significant impurity, which often resulted in better size control and anisotropic morphologies. The precise role of alkylphosphonic acids has been demonstrated by Manna et al.; controlling the ratio of HPA to TOPO resulted in different morphologies.<sup>16</sup> When the ratio of HPA to TOPO was 0-10%, spherical nanocrystals were formed. At 20% HPA, they were able to synthesize nanorods with high aspect ratios, while at 60% HPA the authors observed arrow-shaped crystals. They explained this by the preferential binding of the phosphonic acid to certain facets helping control the growth direction. Therefore, it is generally accepted that purified TOPO alone will not produce high quality nanocrystals with narrow size distribution.

Similar to TOPO are the alkylphosphines, and in particular TOP and TBP. Coordination generally occurs with the surface selenium sites or with elemental Se to make TBPSe/TOPSe. Therefore, alkylphosphines are used both as surfactants for more complete surface passivation, as well as Se delivery agents.<sup>41</sup> Alkylamines and alkanethiols are potentially better than TOPO/TOP because they have less steric hindrance, leading to more complete surface passivation. Theoretically, it was determined that primary amines can cover ~100% of the nanocrystal surface whereas TOPO can cover only 30%.<sup>41</sup> Amines bind through the lone pair on the nitrogen, while the binding in

thiols occurs through the sulfur—the thiol can either keep or lose the hydrogen depending on the reaction conditions. Both amines and thiols bind to either cation or anion species, but amines prefer the anion and thiols prefer the cation. Unlike most ligands listed, which are lewis bases, fatty acids are lewis acids and exhibit extremely tight binding in comparison.<sup>41</sup> The use of fatty acids, and in particular oleic acid, predates the TOPO/organometallic routes. In terms of nanocrystal size control, they are particularly versatile. Qu et al. were able to synthesize a range of CdSe nanocrystal sizes from 2 to >25 nm with the use of fatty acids; however, when they used TOPO, they were only able to obtain a maximum of 11 nm diameter nanocrystals.<sup>22</sup> However, the authors added that because of tight binding due to bidentate coordination, slower nucleation occurs when using fatty acids, which made it more difficult to obtain the smaller sized nanocrystals. The ligands listed above can be broken into 2 groups: L-type and X-type.<sup>42</sup> L-type ligands consist of TOPO, TOP, amines, and thiols that coordinate by donating their lone pair. These ligands are generally more labile and help passivate the nanocrystal surface. X-type ligands are the phosphonic acids and fatty acids that can either bind through the OH group or by the lone pair on the double-bond oxygen, or through both groups, making them stronger binding ligands. The multidentate coordination increases the binding strength in comparison to L-type ligands. It is often found in the literature that optimal nucleation and growth kinetics require the use of a mixed ligand system containing a pair of weakly and strongly binding ligands.<sup>1</sup>

Furthermore, ligands are crucial for nanocrystals to be solution processable; they prevent nanocrystals from aggregating, functionalize the surface and help promote the stable suspension of the nanocrystals in a variety of solvents, preserve the core character,

and assist in substrate adhesion.<sup>23,41,42</sup> Even though ligands have varying binding strengths, they, in general, are relatively labile in solution and can easily be exchanged post-synthesis at room temperature.<sup>11,13,24,25,44</sup> This surface functionalization allows for solubility in a variety of solvents (i.e., non-polar to very polar), as well as control the optical and electronic properties.

**Temperature.** The energy with which surfactants adhere to the nanocrystal surface is important such that they can exchange on/off and allow regions of the nanocrystal surface to be accessible for growth.<sup>39</sup> Ultimately, the temperature affects the binding strength of the ligand.<sup>23</sup> At very high reaction temperatures, the ligand is not well-attached to the surface, which could lead to fast and uncontrolled growth. On the other hand, if the temperature is too low, then the ligands have a stronger attraction to the nanocrystal surface slowing growth. Because the temperature affects the binding strength of the ligands and also the precursor reactivity, it directly affects the nucleation and growth kinetics.<sup>14</sup> There are two temperatures used in the hot injection method, the injection temperature (nucleation) and the growth temperature; because the activation energy is higher for nucleation than for growth, the temperature can be optimized for each regime.<sup>3,4</sup> The injection temperature needs to be high enough for the precursors to decompose/react to form a supersaturation of monomers.<sup>1</sup> Precursor decomposition and/or reaction has thermal barriers so the temperature must be hot enough to allow this rearrangement to occur. The temperature for rearrangement is based off the melting point of the material—melting point depression occurs in nanocrystals, which allows the temperature to be lower than bulk, ~200-400 °C.<sup>39</sup> A higher temperature usually makes the precursors less stable, permitting the easy formation of supersaturated monomers,

which results in a faster nucleation and a large concentration of small nuclei.<sup>3</sup> However, too high of a growth temperature can also lead to uncontrolled growth. For this reason, the growth temperature is typically lower than the nucleation temperature.<sup>39</sup> The growth temperature also affects the size distribution as well as the morphology. For example, when Urban et al. used a growth temperature  $>200$  °C for the PbTe nanocrystal synthesis, they obtained large polydisperse cubic structures.<sup>26</sup> However, when the temperature was less than 170 °C, they observed smaller monodisperse cuboctahedral nanocrystals. Furthermore, the chain length of the surfactant used can also influence the growth temperature and resulting size dispersion. Murray et al. observed that the growth temperature required to synthesize monodisperse nanocrystals decreased with decreasing chain length. When TOPO/TOP was used, the reaction temperature was 280 °C. Reducing the chain length from an 8-carbon chain to a 4-carbon chain (TBP) decreased the temperature to  $<230$  °C. Further reduction to triethyl- and trimethylphosphine and phosphine oxides reduced the temperatures to  $<100$  and  $<50$  °C, respectively. Therefore, controlling the nucleation and growth kinetics in the hot injection method relies on an interplay between the precursors, ligands, their relative concentrations with each other, and the injection and growth temperatures.

### **3.6 Conclusions**

Since its introduction by Murray et al. in 1993, the hot injection method has become a versatile tool for the synthesis of high quality nanomaterials. Its ability to produce high quality nanomaterials stems from the theory of nucleation and growth. Separation of

nucleation and growth is achieved by manipulation of the monomer concentration through precursor reactivity, ligand choice and temperature. This allows a multitude of nanocrystal shapes and morphologies to be realized. Therefore, it is possible to get a better understanding of the electronic properties of nanocrystals—now that high quality synthesis methods have been realized—and improve on the incorporation in optoelectronic devices. Furthermore, the synthetic method has been shown to be 43 applicable toward a wide range of materials used in many optoelectronic applications. The examples discussed above are a model system for the syntheses of these more complex materials, such as the ones discussed in this dissertation. As composition now becomes a competing factor with size distribution and morphology, an even stronger emphasis is placed on optimizing the precursor reactivities.

### 3.7 References

- (1) Burda, C.; Chen, X. B.; Narayanan, R.; El-Sayed, M. A. *Chem. Rev.* **2005**, *105*, 1025-1102.
- (2) Cushing, B. L.; Kolesnichenko, V. L.; O'Connor, C. J. *Chem. Rev.* **2004**, *104*, 3893-3946.
- (3) de Mello Donega, C.; Liljeroth, P.; Vanmaekelbergh, D. *Small* **2005**, *1*, 1152-1162.
- (4) Talapin, D. V.; Lee, J.-S.; Kovalenko, M. V.; Shevchenko, E. V. *Chem. Rev.* **2010**, *110*, 389-458.
- (5) Ginley, D.; Green, M. A.; Collins, R. *MRS Bull.* **2008**, *33*, 355-363.
- (6) Slaoui, A.; Collins, R. T. *MRS Bull.* **2007**, *32*, 211-218.
- (7) Habas, S.; Platt, H.; van Hest, M.; Ginley, D. *Chem. Rev.* **2010**, *110*, 6571-6594.
- (8) Hillhouse, H. W.; Beard, M. C. *Curr. Opin. Colloid Interface Sci.* **2009**, *14*, 245-259.
- (9) Geyer, S.; Porter, V. J.; Halpert, J. E.; Mentzel, T. S.; Kastner, M. A.; Bawendi, M. G. *Phys. Rev. B* **2010**, *82* (15), 155201.
- (10) Guo, Q.; Ford, G. M.; Hillhouse, H. W.; Agrawal, R. *Nano Lett.* **2009**, *9* (8), 3060-3065.
- (11) Kovalenko, M. V.; Scheele, M.; Talapin, D. V. *Science* **2009**, *324*, 1417-1420.
- (12) Sargent, E. H. *Nat. Photonics* **2009**, *3*, 325-331.
- (13) Talapin, D. V.; Murray, C. B. *Science* **2005**, *310*, 86-89.
- (14) Murray, C. B.; Norris, D. J.; Bawendi, M. G. *J. Am. Chem. Soc.* **1993**, *115*, 8706-8715.
- (15) Steigerwald, M. L.; Alivisatos, A. P.; Gibson, J. M.; Harris, T. D.; Kortan, R.; Muller, A. J.; Thayer, A. M.; Duncan, T. M.; Douglass, D. C.; Brus, L. E. *J. Am. Chem. Soc.* **1988**, *110*, 3046-3050.
- (16) Peng, X.; Wickham, J.; Alivisatos, A. P. *J. Am. Chem. Soc.* **1998**, *120*, 5343-5344.

- (17) Peng, X. G.; Manna, L.; Yang, W. D.; Wickham, J.; Scher, E.; Kadavanich, A.; Alivisatos, A. P. *Nature* **2000**, *404*, 59-61.
- (18) Manna, L.; Scher, E. C.; Alivisatos, A. P. *J. Am. Chem. Soc.* **2000**, *122*, 12700-12706.
- (19) Morgan, N. Y.; Leatherdale, C. A.; Drndic, M.; Jarosz, M. V.; Kastner, M. A.; Bawendi, M. *Phys. Rev. B* **2002**, *66* (7), 075339.
- (20) Peng, Z.; Peng, X. *J. Am. Chem. Soc.* **2001**, *123* (1), 183-184.
- (21) Peng, Z. A.; Peng, X. *J. Am. Chem. Soc.* **2002**, *124* (13), 3343-3353.
- (22) Qu, L.; Peng, Z. A.; Peng, X. **2001**, *1* (6), 333-337.
- (23) Dai, Q.; Zhang, Y.; Wang, Y.; Wang, Y.; Zou, B.; Yu, W. W.; Hu, M. Z. *J. Phys. Chem. C* **2010**, *114*, 16160-16167.
- (24) Law, M.; Luther, J. M.; Song, Q.; Hughes, B. K.; Perkins, C. L.; Nozik, A. J. *J. Am. Chem. Soc.* **2008**, *130*, 5974-5985.
- (25) Luther, J. M.; Law, M.; Song, Q.; Perkins, C. L.; Beard, M. C.; Nozik, A. J. *ACS Nano* **2008**, *2*, 271-280.
- (26) Urban, J. J.; Talapin, D. V.; Shevchenko, E. V.; Murray, C. B. *J. Am. Chem. Soc.* **2006**, *128*, 3248-3255.
- (27) Riha, S. C.; Johnson, D. C.; Prieto, A. L. *J. Am. Chem. Soc.* **2011**, *133*, 1383-1390.
- (28) Deka, S.; Genovese, A.; Zhang, Y.; Miszta, K.; Bertoni, G.; Krahne, R.; Giannini, C.; Manna, L. *J. Am. Chem. Soc.* **2010**, *132*, 8912-8914.
- (29) Wu, Y.; Wadia, C.; Ma, W.; Sadtler, B.; Alivisatos, A. *Nano Lett.* **2008**, *8*, 2551-2555.
- (30) Puthussery, J.; Seefeld, S.; Berry, N.; Gibbs, M.; Law, M. *J. Am. Chem. Soc.* **2011**, *133*, 716-719.
- (31) LaMer, V.; Dinegar, R. *J. Am. Chem. Soc.* **1950**, *72*, 4847-4854.
- (32) Guo, Q.; Kim, S.; Kar, M.; Shafarman, W.; Birkmire, R.; Stach, E.; Agrawal, R.; Hillhouse, H. *Nano Lett.* **2008**, *8* (9), 2982-2987.
- (33) Riha, S. C.; Parkinson, B. A.; Prieto, A. L. *J. Am. Chem. Soc.* **2009**, *131* (34), 12054-12055.

- (34) Riha, S. C.; Parkinson, B. A.; Prieto, A. L. *Manuscript in preparation* **2011**.
- (35) Shavel, A.; Arbiol, J.; Cabot, A. *J. Am. Chem. Soc.* **2010**, *132* (13), 4514-4515.
- (36) Guo, Q.; Hillhouse, H. W.; Agrawal, R. *J. Am. Chem. Soc.* **2009**, *131* (33), 11672-11673.
- (37) LaMer, V.; Dinegar, R. *J. Am. Chem. Soc.* **1950**, *72* (11), 4847-4854.
- (38) Finney, E. E.; Finke, R. G. *J. Colloid Interface Sci.* **2008**, *317*, 351-374.
- (39) Yin, Y.; Alivisatos, A. P. *Nature* **2005**, *437*, 664-670.
- (40) Turkevich, J.; Stevenson, P. C.; Hillier, J. *Discuss. Faraday Soc.* **1951**, *11*, 55-75.
- (41) Green, M. *J. Mater. Chem.* **2010**, *20*, 5797-5809.
- (42) Morris-Cohen, A.; Donakowski, M.; Knowles, K.; Weiss, E. *J. Phys. Chem. C* **2009**, *114*, 897-906.
- (43) Wang, F.; Tang, R.; Buhro, W. *Nano Lett.* **2008**, *8*, 3521-3524.
- (44) Luther, J. M.; Law, M.; Beard, M. C.; Song, Q.; Reese, M. O.; Ellingson, R. J.; Nozik, A. J. *Nano Lett.* **2008**, *8*, 3488-3492.

## CHAPTER 4

### SOLUTION-BASED SYNTHESIS AND CHARACTERIZATION OF $\text{Cu}_2\text{ZnSnS}_4$ NANOCRYSTALS

The contents in this dissertation chapter include a communication published in *The Journal of the American Chemical Society* **2009**, *131*, 12054-12055 and is available on-line at <http://dx.doi.org/10.1021/ja9044168>. This chapter presents one of the first solution-based synthetic routes to a quaternary nanomaterials, namely  $\text{Cu}_2\text{ZnSnS}_4$ .

The synthetic method was developed by Shannon C. Riha, who also prepared the manuscript with helpful insights, discussions, and editing by Prof. Bruce A. Parkinson and Prof. Amy L. Prieto.

## 4.1 Overview

Recent advances have been made in thin-film solar cells using CdTe and  $\text{CuIn}_{1-x}\text{Ga}_x\text{Se}_2$  (CIGS) nanoparticles, which have achieved impressive efficiencies. Despite these efficiencies, CdTe and CIGS are not amenable to large-scale production because of the cost and scarcity of Te, In, and Ga.  $\text{Cu}_2\text{ZnSnS}_4$  (CZTS), however, is an emerging solar cell material that contains only earth-abundant elements and has a near-optimal direct band gap of 1.45–1.65 eV and a large absorption coefficient. Here we report the direct synthesis of CZTS nanocrystals using the hot-injection method. In-depth characterization indicated that pure stoichiometric CZTS nanocrystals with an average particle size of  $12.8 \pm 1.8$  nm were formed. Optical measurements showed a band gap of 1.5 eV, which is optimal for a single-junction solar device.

## 4.2 Communication

Thin film solar cells offer the promise of both low cost and scalability, features that are vital for any approach toward providing large amounts of carbon free power.<sup>1</sup> In a recent review by Wadia et al., 23 thin film absorber materials were compared in terms of their extraction costs and annual electricity potential.<sup>2</sup> Of those 23 materials, CdTe and  $\text{CuIn}_{1-x}\text{Ga}_x\text{Se}_2$  (CIGS) are two materials that are currently being commercialized for thin film photovoltaic devices, reducing the cost per watt of solar electricity below that of conventional silicon solar cells.<sup>1-3</sup> Due to both the cost and scarcity of Te, In and Ga, neither of these thin film technologies are likely amenable for large-scale production.<sup>2,3</sup> New thin film photovoltaic absorber materials containing only earth abundant elements are desperately needed for large-scale photovoltaic production.  $\text{Cu}_2\text{ZnSnS}_4$  (CZTS) is an

emerging solar cell material that contains earth abundant elements, has a near optimum direct band gap energy of  $\sim 1.5$  eV and a large absorption coefficient,  $>10^4$   $\text{cm}^{-1}$ .<sup>4-6</sup> Furthermore, CZTS is a p-type semiconductor that crystallizes in the kesterite crystal system with copper and zinc sharing the same Wyckoff position.<sup>7</sup> This, combined with being a quaternary material, allows one to tune the composition and, hence, the material properties, which is an advantage over potential binary materials for thin film absorbers. Thin film solar cells with efficiencies of up to 6.7% have been fabricated from CZTS using costly and low throughput sputtering and vapor deposition techniques (which are also mainly used for CdTe and CIGS production).<sup>1,4-6</sup>

A new method for scaling up solar cell production is based on the synthesis of nanocrystals either dispersed in an “ink” that can be thermally annealed into larger grain thin films, or used to make solar cell devices using as-deposited three dimensional arrays of photoactive nanocrystals.<sup>8</sup> These approaches have spurred interest in the synthesis of ternary nanoparticles such as  $\text{CuIn}(\text{S},\text{Se})_2$ .<sup>9-11</sup> Herein we report the synthesis of CZTS nanocrystals, the key first step in the fabrication of both nanoparticle inks and photoactive nanocrystal arrays.<sup>12</sup>

We used the hot-injection solution synthesis method to prepare CZTS nanocrystals. This method involves injecting a cold solution of precursors into a hot surfactant solution, leading to the immediate nucleation and growth of nanocrystals.<sup>13,14</sup> We chose this route because it has been successful for the syntheses of a wide range of semiconducting chalcogenide nanocrystals, such as  $\text{CdX}$  ( $\text{X}=\text{S}, \text{Se}, \text{Te}$ ) and CIGS, with exquisite control over composition and morphology. This approach will enable low-cost fabrication of solar cell devices through techniques such as drop casting, dip coating, spin coating, or

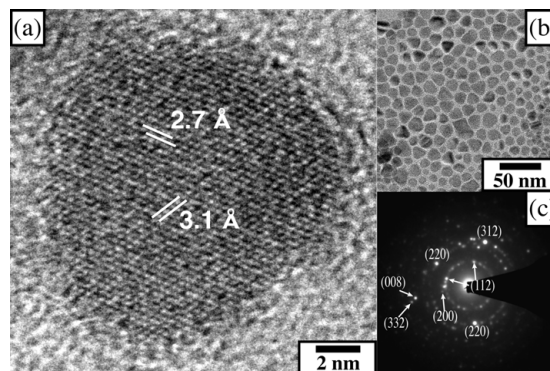


**Figure 4.1.** TEM images of  $\text{Cu}_2\text{ZnSnS}_4$  nanocrystals. The HR-TEM image in (a) shows an interplanar spacing of 2.7 and 3.1 Å corresponding to the (200) and (112) planes, respectively, and the CZTS nanocrystals in (b) have an average size of  $12.8 \pm 1.8$  nm. The SAED in (c) was indexed to CZTS.

printing of the resulting CZTS nanocrystal solution.<sup>9,10,15-17</sup> To our knowledge this is the first reported synthesis of  $\text{Cu}_2\text{ZnSnS}_4$  nanocrystals, and the first directed synthesis of quaternary nanoparticles.

In a typical synthesis, stoichiometric amounts of copper (II) acetylacetonate, zinc acetate, and tin (IV) acetate were combined under inert conditions in oleylamine and heated to 150 °C under vacuum; the temperature was reduced to 125 °C after 0.5 h. In a separate vial, sulfur powder was sonicated in oleylamine until an orange-red solution was obtained. Trioctylphosphine oxide (TOPO) was heated to 300 °C and the S and metal precursors were rapidly injected. Aliquots were taken every fifteen minutes over a 75 minute total reaction time.

Figure 4.1 shows TEM images representative of the CZTS nanocrystals synthesized at 300 °C for 45 minutes; additional TEM images and size distribution plots for all aliquots are shown in Figure S4.1. Figure 4.1b is a lower magnification TEM image of triangular and round CZTS nanocrystals with an average particle size of  $12.8 \pm 1.8$  nm (Figure S4.1h). High-resolution TEM (Figure 4.1a) shows that the nanocrystals are single crystalline. The selected area electron diffraction (SAED) pattern shown in Figure

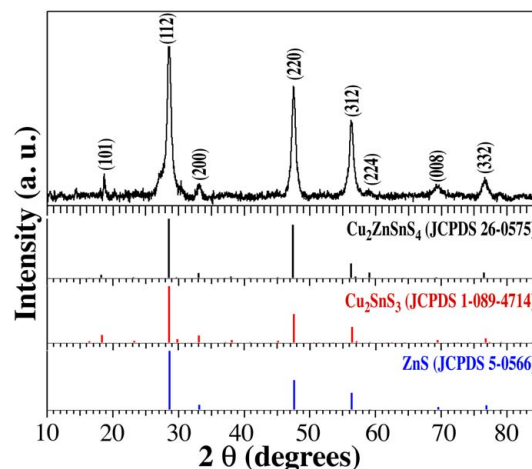


**Figure 4.2.** XRD pattern ( $\lambda = 1.54 \text{ \AA}$ ) for the  $\text{Cu}_2\text{ZnSnS}_4$  nanocrystals. The peaks have been indexed to tetragonal CZTS (JCPDS 26-0575). Below the XRD pattern are the standards for CZTS (black), CTS (red), and ZnS (blue), indicating the three materials have similar diffraction patterns.

4.1c matches the structure of CZTS (JCPDS 26-0575, indexed using the method of relative ratios) as indicated by the diffraction spots corresponding to the (112), (200), (220), (312), (008), and (332) planes. Large area, scanning electron microscopy (SEM) images show that the CZTS nanocrystals are of similar size and pack uniformly (Figure S4.2a).

The structure and composition of the CZTS nanocrystals were confirmed with X-ray diffraction (XRD, Figure 4.2) and energy dispersive spectroscopy (EDS taken in both the SEM and TEM, Figures S4.2b and S4.3). The diffraction pattern shown in Figure 4.2 was indexed to tetragonal  $\text{Cu}_2\text{ZnSnS}_4$  and the average nanocrystal size, evaluated using the Williamson-Hall method, was consistent with the particle sizes measured by TEM (Figure S4.4). However, the diffraction patterns of stoichiometric tetragonal  $\text{Cu}_2\text{SnS}_3$  (JCPDS 01-089-4714) and cubic ZnS (JCPDS 5-0566), have very similar lattice parameters. EDS of various areas of the CZTS sample showed a stoichiometric ratio for Cu:Zn:Sn:S of 2:1:1:4 (Figures S4.2b and S4.3). XPS analysis was used to confirm the

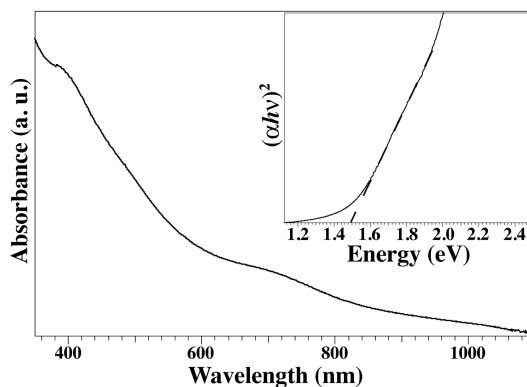


**Figure 4.3.** UV-VIS absorption spectrum of  $\text{Cu}_2\text{ZnSnS}_4$  nanocrystals. The inset shows an obtained band gap of 1.5 eV.

presence of all four elements in their expected oxidation states (Figure S4.5). To rule out the possibility that the samples were a coincidental stoichiometric mixture of  $\text{Cu}_2\text{SnS}_3$ :ZnS phases, differential thermal analysis (DTA) of the nanocrystals was performed.

In the bulk, these materials all have high melting points ( $\text{Cu}_2\text{SnS}_3$  has a phase transition at 775 °C from triclinic to cubic, and melts at 850 °C,<sup>18,19</sup> CZTS melts at 991 °C,<sup>19</sup> and ZnS undergoes a phase transition from cubic to wurtzite at 1020 °C and melts at 1650 °C<sup>20</sup>); however, for nanocrystals, these temperatures could be depressed. Differential thermal analysis (DTA) (Figure S4.6) for two preparations of CZTS nanocrystals,  $\text{Cu}_2\text{SnS}_3$  nanocrystals and a mixture of  $\text{Cu}_2\text{SnS}_3$  and ZnS (synthesis and XRD of ZnS and  $\text{Cu}_2\text{SnS}_3$  given in Supporting Information, Figure S4.7)<sup>21</sup> revealed that the two samples of CZTS each show a single phase-transition temperature below 830 °C, while the  $\text{Cu}_2\text{SnS}_3$  nanoparticles show a transition at 747 °C. The mixture of  $\text{Cu}_2\text{SnS}_3$  and ZnS exhibits two phase transitions: one at 736 °C, which can be attributed to  $\text{Cu}_2\text{SnS}_3$ , and a second at 816 °C. This transition point could be attributed to either ZnS or  $\text{Cu}_2\text{ZnSnS}_4$ , which may have formed as the mixture was heated. The clear difference

between the CZTS as prepared samples, and the intentionally mixed  $\text{Cu}_2\text{SnS}_3$  and ZnS sample indicate that the synthesized nanocrystals are pure  $\text{Cu}_2\text{ZnSnS}_4$  rather than a mixture of  $\text{Cu}_2\text{SnS}_3$  and ZnS.

UV-VIS absorption spectroscopy was used to evaluate the optical properties of the nanocrystals (Figure 4.3). Plotting the square of the absorption coefficient,  $a$ , multiplied by the photon energy,  $(\alpha h\nu)^2$  versus the photon energy,  $h\nu$ , shows a band gap of 1.5 eV, consistent with the literature values of 1.45-1.6 eV.<sup>4-6</sup> This value is near the optimum for photovoltaic solar conversion in a single band gap device. The band gap of  $\text{Cu}_2\text{SnS}_3$  is 0.93 eV, further evidence that this phase is not present.<sup>18</sup> Preliminary experiments show that dip-cast CZTS nanocrystal films exhibit a clear photoresponse (Figure S4.8). An in depth investigation of these properties will be reported shortly.<sup>22</sup>

We have shown for the first time that homogeneous, nearly monodisperse CZTS nanocrystals can be synthesized in solution through the hot-injection method. XRD, EDS, XPS, and thermal analysis confirmed that the structure and composition of the as synthesized nanocrystals correspond to pure  $\text{Cu}_2\text{ZnSnS}_4$ . UV-VIS data indicate an optical band gap of 1.5 eV for the CZTS nanocrystals, optimal for photovoltaic applications, and preliminary results indicate that films of these nanoparticles exhibit a clear photoresponse.

### 4.3 Experimental Details

**CZTS Nanocrystal Synthesis.** Copper(II) acetylacetonate ( $\text{Cu}(\text{acac})_2$ , Aldrich, 99.99%), tin(IV) acetate ( $\text{Sn}(\text{OAc})_4$ , Aldrich), zinc acetate ( $\text{Zn}(\text{OAc})_2$ , Fisher), sulfur powder (S, Aldrich), trioctylphosphine oxide (TOPO, Aldrich, 99%), and oleylamine

(OLA, Aldrich, 70%) were purchased and used as received. All reaction conditions were kept under inert atmosphere to prevent the formation of oxides. In a typical synthesis, a mixture of 0.5 mmol Cu(acac)<sub>2</sub>, 0.25 mmol Zn(OAc)<sub>2</sub>, 0.25 mmol Sn(OAc)<sub>4</sub>, and 4 mL OLA was prepared in a 25 mL 3-neck round-bottom reaction flask and heated under vacuum to 150 °C for 30 minutes. During heating the solution turned from a dark blue to a brown-green color, indicating the formation of the Cu-, Zn-, and Sn-oleylamine complexes. The temperature was lowered to 125 °C and the mixture remained at this temperature under vacuum until injection. In a 20 mL scintillation vial, 1.0 mmol S powder and 1 mL OLA was sonicated until the S dissolved and a red-orange solution formed (15-30 minutes). In a 50 mL 3-neck round-bottom reaction flask, 10 mmol TOPO was heated to 300 °C on an Ar Schlenk line. When the temperature of the TOPO reaction flask reached 100 °C, the flask was pumped and purged three times, then flushed with Ar and kept under Ar for the remainder of the experiment. When the TOPO reaction temperature reached 300 °C, the S and metal precursors were rapidly injected simultaneously via two gas-tight Luer-Lock syringes. The reaction solution immediately changed from clear and colorless to a clear dark brown solution. Aliquots were taken every 15 minutes for a total of 75 minutes.

Methanol was added to each of the aliquots to precipitate the nanocrystals, followed by 10 minutes of centrifugation at 3500 rpm. The supernatant, containing unreacted material was discarded, while the remaining precipitate was then redispersed in hexanes. Methanol was again added and the solution was centrifuged for 10 minutes. This process was repeated for a total of three washes. The final precipitate was resuspended in

hexanes and then centrifuged for 10 minutes to remove any agglomerated or bulk constituents.

***Cu<sub>2</sub>SnS<sub>3</sub> Nanocrystal Synthesis.*** A similar procedure to the one above was used for the synthesis of CTS nanocrystals. Appropriate amounts of Cu(acac)<sub>2</sub> and Sn(OAc)<sub>4</sub> were mixed with OLA and heated under vacuum to 150 °C. TOPO was heated in a separate round bottom flask to 300 °C on an Ar Schlenk line. S powder was dissolved in OLA through sonication. When the reaction temperature reached 300 °C, the S and metal precursors were rapidly injected and the solution changed from clear and colorless to dark brown.

***ZnS Nanocrystal Synthesis.*** ZnS nanocrystals were synthesized following a literature preparation (Gu, F.; Li, C. Z.; Wang, S. F.; Lu, M. K. *Langmuir* **2006**, 22, 1329-1332). In a typical synthesis, 1 g zinc nitrate hexahydrate (Zn(NO<sub>3</sub>)<sub>3</sub>, Fisher), 0.667 g thioacetamide (Fisher), and 50 mL distilled water were combined in a 100 mL 3-neck round-bottom flask equipped with a Teflon stir bar, thermocouple, and reflux condenser. The reaction solution was vigorously stirred until the Zn(NO<sub>3</sub>)<sub>3</sub> and thioacetamide dissolved completely. The reaction temperature was then brought to 103 °C at a rate of 500 °C/h. After 15 minutes at the target temperature, the reaction solution changed from clear and colorless to a turbid off-white color. The reaction was quenched after 25 minutes by removing the heating mantle and letting the reaction cool to room temperature. The ZnS nanoparticles were precipitated by centrifuging the sample at 3500 rpm for 10 minutes and then decanting the supernatant. The remaining solid was washed three times with ethanol and water and dried for thermal analysis.

**Materials Characterization.** HR-TEM images were taken using a Phillips CM200 STEM with an accelerating voltage of 200 kV. The TEM is equipped with a Princeton Gamma Tech Prism 2000 EDS detector, which we used for elemental analysis of the CZTS nanocrystals. Low-resolution TEM images were obtained on a JEOL JEM 2000 at an accelerating voltage of 160 kV. TEM samples were prepared by dip-casting CZTS nanocrystals dispersed in hexanes onto either carbon-coated copper TEM grids (200 mesh, Ted Pella) or onto lacy carbon-coated nickel TEM grids (200 mesh, Structure Probe, Inc.). SEM imaging was performed using a JEOL JSM 6500F FE-SEM equipped with a Thermo Electron EDS detector. Images were acquired under an accelerating voltage of 15 kV and a working distance of 10 mm. XRD was performed on a Scintag X-2 Advanced Diffraction System equipped with Cu K $\alpha$  radiation ( $\lambda=1.54 \text{ \AA}$ ) using a dried powder sample of the CZTS nanocrystals. High-resolution XPS data was obtained using a Physical Electronics PHI 5800 ESCA System. DTA was acquired using a TA Instruments 1600 DTA with a ramp rate of 10 °C/min to 1100 °C. UV-VIS absorbance spectra were collected on an Agilent Technologies 8453 spectrometer. Photoelectrochemical measurements were taken using an aqueous solution of 0.1 M KCL/0.1 M Eu(NO<sub>3</sub>)<sub>3</sub> electrolyte with a platinum mesh basket counter and Ag/AgCl reference electrode. Photocurrent response was produced using a green laser (532 nm) with an output power of 17 mW and a chopping frequency of 5 Hz. Current-voltage (I-V) plots were recorded by cathodically scanning the potential at a rate of 2 mV/s from 0 V to -0.7 V. Stability testing was done by chronoamperometric techniques with an applied potential of -0.6 V.

#### **4.4 Acknowledgements**

We thank Dr. John Chandler and Dr. Gary Zito at the Colorado School of Mines (HR-TEM) and Dr. Sandeep Kohli (Colorado State University, DTA) for their assistance. We thank the CSU Clean Energy Supercluster and the Center for Revolutionary Solar Photoconversion (CRSP) for funding.

## 4.5 References

- (1) Gingley, D.; Green, M. A.; Collins, R. *MRS Bulletin* **2008**, *33*, 355-363.
- (2) Wadia, C.; Alivisatos, A. P.; Kammen, D. M. *Environ. Sci. Technol.* **2009**, *43*, 2072-2077.
- (3) Scragg, J. J.; Dale, P. J.; Peter, L. M.; Zoppi, G.; Forbes, I. *Phys. Status Solidi B* **2008**, *245*, 1772-1778.
- (4) Jimbo, K.; Kimura, R.; Kamimura, T.; Yamada, S.; Maw, W. S.; Araki, H.; Oishi, K.; Katagiri, H. *Thin Solid Films* **2007**, *515*, 5997-5999.
- (5) Katagiri, H. *Thin Solid Films* **2005**, *480-481*, 426-432.
- (6) Katagiri, H.; Saitoh, K.; Washio, T.; Shinohara, H.; Kurumadani, T.; Miyajima, S. *Sol. Energy Mater. Sol. Cells* **2001**, *65*, 141-148.
- (7) Schorr, S.; Gonzalez-Aviles, G. *physica status solidi (a)* **2009**, *206*, 1054-1058.
- (8) Panthani, M. G.; Akhavan, V.; Goodfellow, B.; Schmidtke, J. P.; Dunn, L.; Dodabalapur, A.; Barbara, P. F.; Korgel, B. A. *J. Am. Chem. Soc.* **2008**, *130*, 16770-16777.
- (9) Koo, B.; Patel, R. N.; Korgel, B. A. *J. Am. Chem. Soc.* **2009**, *131*, 3134-3135.
- (10) Tang, J.; Hinds, S.; Kelley, S. O.; Sargent, E. H. *Chem. Mater.* **2008**, *20*, 6906-6910.
- (11) Koo, B.; Patel, R. N.; Korgel, B. A. *Chem. Mater.* **2009**, *21*, 1962-1966.
- (12) Luther, J. M.; Law, M.; Beard, M. C.; Song, Q.; Reese, M. O.; Ellingson, R. J.; Nozik, A. J. *Nano Lett.* **2008**, *8*, 3488-3492.
- (13) Yin, Y.; Alivisatos, A. P. *Nature* **2004**, *437*, 664-670.
- (14) Peng, Z. A.; Peng, X. *J. Am. Chem. Soc.* **2002**, *124*, 3343-3353.
- (15) Cushing, B. L.; Kolesnichenko, V. L.; O'Connor, C. J. *Chem. Rev.* **2004**, *104*, 3893-3946.
- (16) Milliron, D. J.; Hughes, S. M.; Cui, Y.; Manna, L.; Li, J.; Wang, L. W.; Alivisatos, A. P. *Nature* **2004**, *430*, 190-195.

- (17) Peng, X. G.; Manna, L.; Yang, W. D.; Wickham, J.; Scher, E.; Kadavanich, A.; Alivisatos, A. P. *Nature* **2000**, *404*, 59-61.
- (18) Fiechter, S.; Martinez, M.; Schmidt, G.; Henrion, W.; Tomm, Y. **2003**, 1859-1862.
- (19) Moh, G. H.; Heidelberg *Chem. Erde* **1975**, *34*, 1-61.
- (20) Qadri, S. B.; Skelton, E. F.; Hsu, D.; Dinsmore, A. D.; Yang, J.; Gray, H. F.; Ratna, B. R. *Phys. Rev. B* **1999**, *60*, 9191-9193.
- (21) Gu, F.; Li, C. Z.; Wang, S. F.; Lu, M. K. *Langmuir* **2006**, *22*, 1329-1332.
- (22) Riha, S. C.; Fredrick, S. J.; Sambur, J. B.; Liu, Y.; Prieto, A. L.; Parkinson, B. A. *ACS Appl. Mater. Interfaces* **2010**, *3*, 58-66.

Supporting Information for:

**Solution-Based Synthesis and Characterization of  $\text{Cu}_2\text{ZnSnS}_4$  Nanocrystals**

*Shannon C. Riha, Bruce A. Parkinson, and Amy L. Prieto*

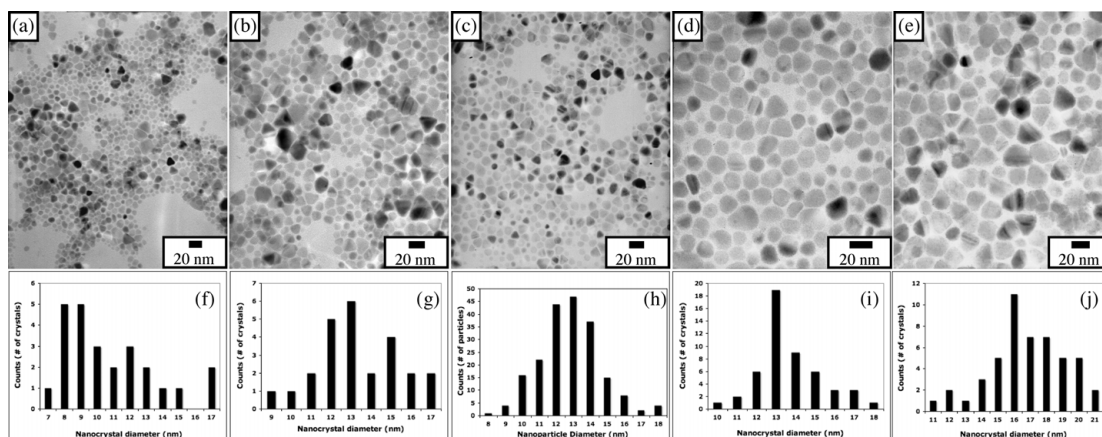


**Figure S4.1.** TEM images (a-e) and the corresponding size distribution plots (f-j) for each aliquot (a), (f) 15 minutes, (b), (g) 30 minutes, (c), (h) 45 minutes, (d), (i) 60 minutes, and (e), (j) 75 minutes. The 15, 30, and 75 minute aliquots show a wide size distribution (>15%), while the 45 minute aliquot shows a 14% size distribution and the 60 minute shows a 12% size distribution. The average size of the CZTS nanocrystals was  $10.8 \pm 2.7$  nm after 15 minutes,  $13.3 \pm 2.1$  nm after 30 minutes,  $12.8 \pm 1.8$  nm after 45 minutes,  $13.7 \pm 1.7$  nm after 60 minutes, and  $17.0 \pm 2.5$  nm after 75 minutes. The size distribution becomes narrower with time, until after 60 minutes. At this point, the particles start to become more polydisperse and begin dissolving back into solution, as observed by the course edges of the nanocrystals. A similar phenomenon was also observed in [8]

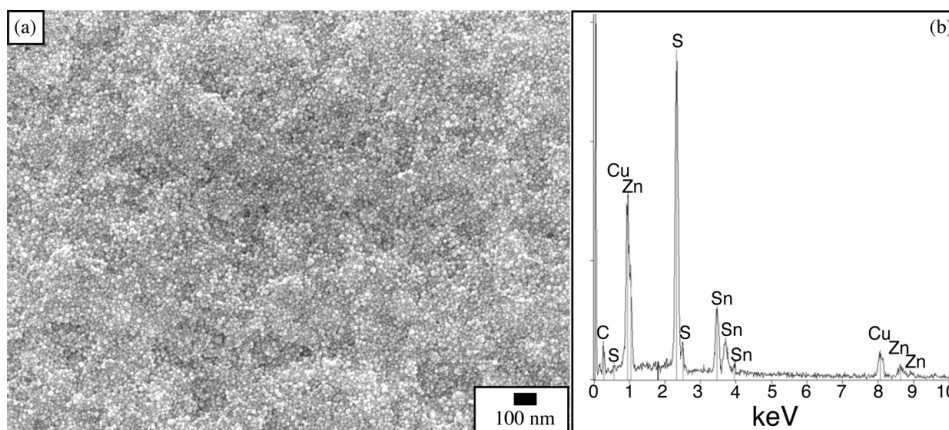


**Figure S4.2.** SEM image and EDS of CZTS nanocrystals. The SEM image (a) shows the nanocrystals are uniformly distributed over the substrate and are of similar size and (b) is the corresponding EDS spectrum. The relative elemental ratios for Cu:Zn:Sn:S were consistent with the 2:1:1:4 stoichiometry.

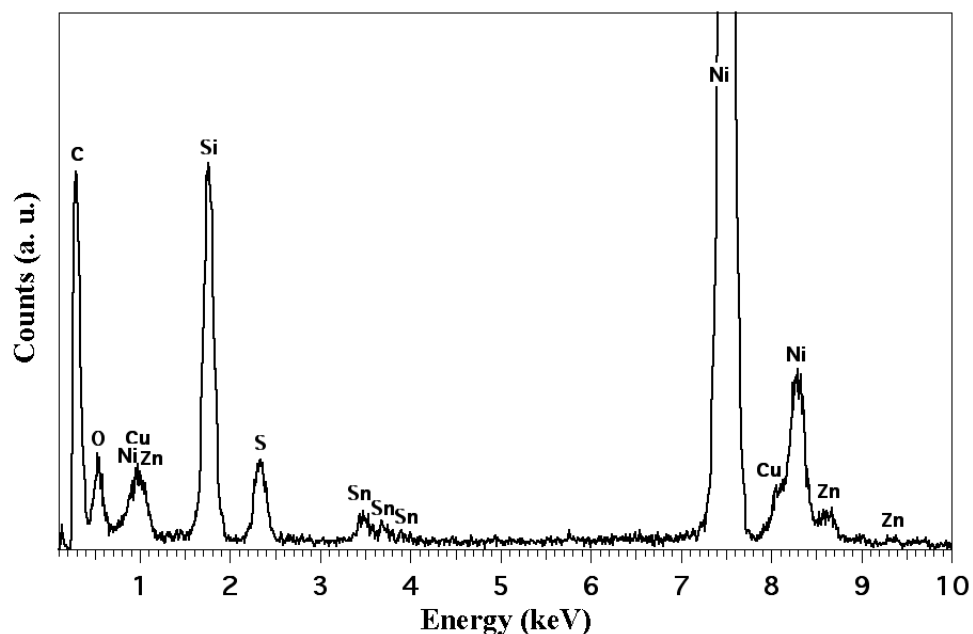


**Figure S4.3.** EDS spectrum (taken in the TEM) of the CZTS nanocrystals shown in Figure 4.1a. The relative elemental ratios for Cu:Zn:Sn:S were consistent with the 2:1:1:4 stoichiometry. The Ni, C, O, and Si signals resulted from the lacy carbon-coated Ni-TEM grid.

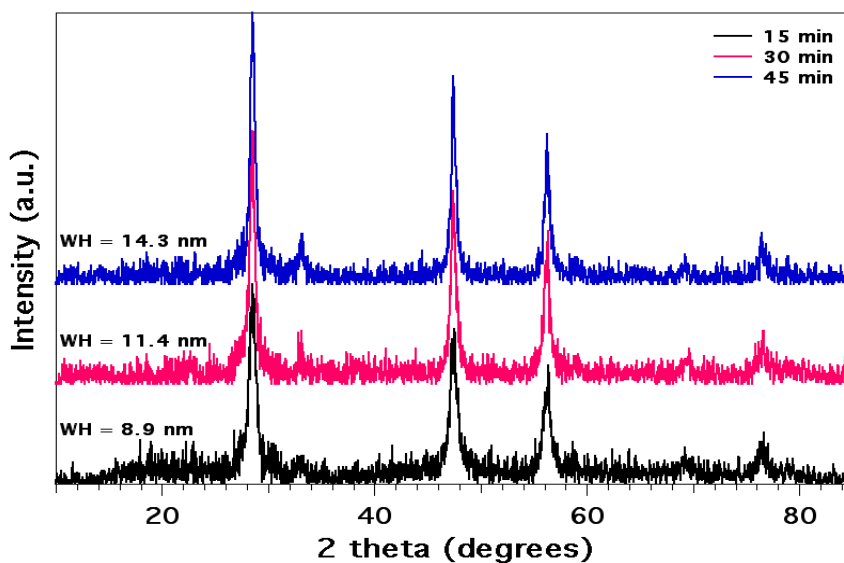


**Figure S4.4.** XRD patterns of the first three aliquots: 15 minutes (black), 30 minutes (red), and 45 minutes (blue). The Williamson-Hall method was used to evaluate the full width at half max in each of the patterns. The calculated CZTS nanocrystal size was 8.9 nm for the 15 minute aliquot, 11.4 nm for the 30 minute aliquot, and 14.3 nm for the 45 minute aliquot, all consistent with the data shown in the TEM images (Figure S4.1).

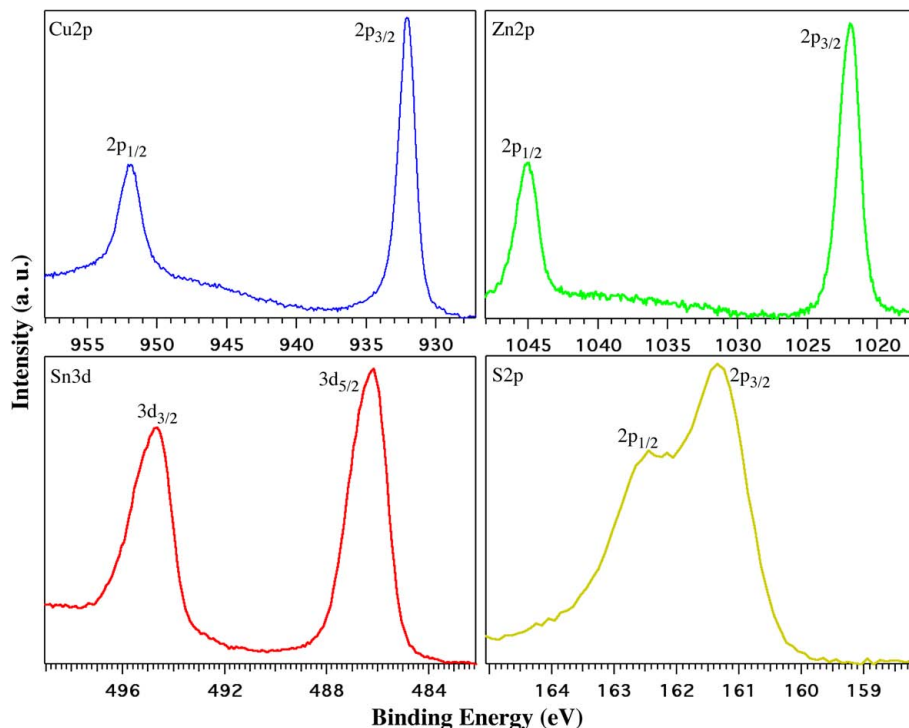


**Figure S4.5.** High-resolution XPS analysis of the four constituent elements: copper 2p (blue), zinc 2p (green), tin 3d (red), and sulfur 2p (yellow). The copper HR-XPS spectrum shows two narrow and symmetric peaks at 932 and 952 eV, indicative of Cu(I) with a peak splitting of 19.8 eV. The zinc 2p peaks located at 1022 and 1045 eV show a peak separation of 23 eV, consistent with the standard splitting of 22.97 eV, suggesting zinc(II). The tin 3d<sub>5/2</sub> peaks located at 486.2 and 494.9 eV, and a peak splitting of 8.4 eV indicates Sn(IV). The S 2p<sub>3/2</sub> peak for sulfides lies between 160 and 164 eV with a peak splitting of 1.18 eV. The sulfur 2p<sub>3/2</sub> and 2p<sub>1/2</sub> peaks in the spectra are located at 161.3 and 162.45 eV, which are consistent with the 160-164 eV range expected for S in sulfide phases.

Differential thermal analysis (DTA) was the ultimate characterization technique to confirm phase-purity. Because the main impurities probable in CZTS are similar in structure and in composition, the above mentioned characterization techniques alone do not provide direct evidence for a pure CZTS sample. However, thermal analysis is one of the few ways to determine if structurally similar impurities exist because the melting points of such impurities are different. Two CZTS samples from different reaction

batches were analyzed and compared to a sample of just  $\text{Cu}_2\text{SnS}_3$  and a mixture of  $\text{Cu}_2\text{SnS}_3$  and  $\text{ZnS}$ . All materials were synthesized in our lab and a total of  $\sim 10$  mg of sample were used for each run. From the data shown below in Figure S4.6, it becomes clear that there is only one material present in the CZTS samples based on only one melting point, that differs from both  $\text{Cu}_2\text{SnS}_3$  and  $\text{ZnS}$ .

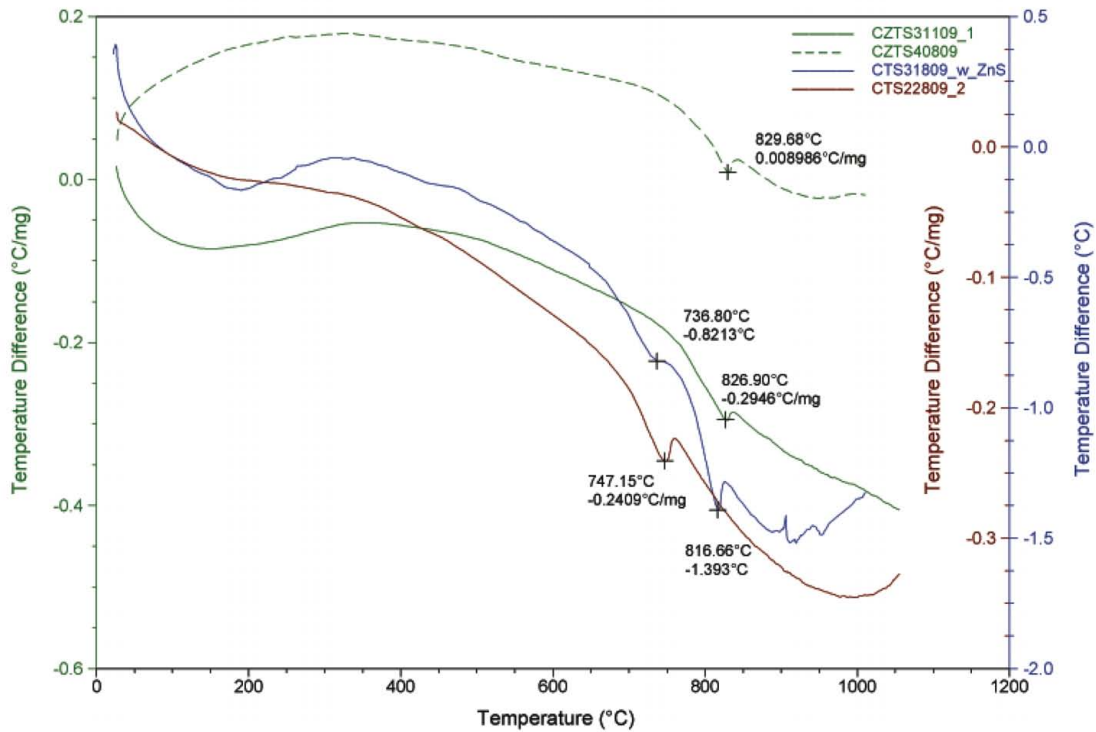


**Figure S4.6.** DTA analysis of two different batches of CZTS nanocrystals (green, dashed green), CTS nanocrystals (maroon), and a mixture of CTS and ZnS nanocrystals (blue). The data suggests that the CZTS nanocrystals are pure CZTS and not a mixture of CTS and ZnS nanocrystals. Note that the mixture of CTS and ZnS exhibits 2 transition temperatures while the as prepared CZTS samples show only one transition temperature higher than either observed in the mixture.

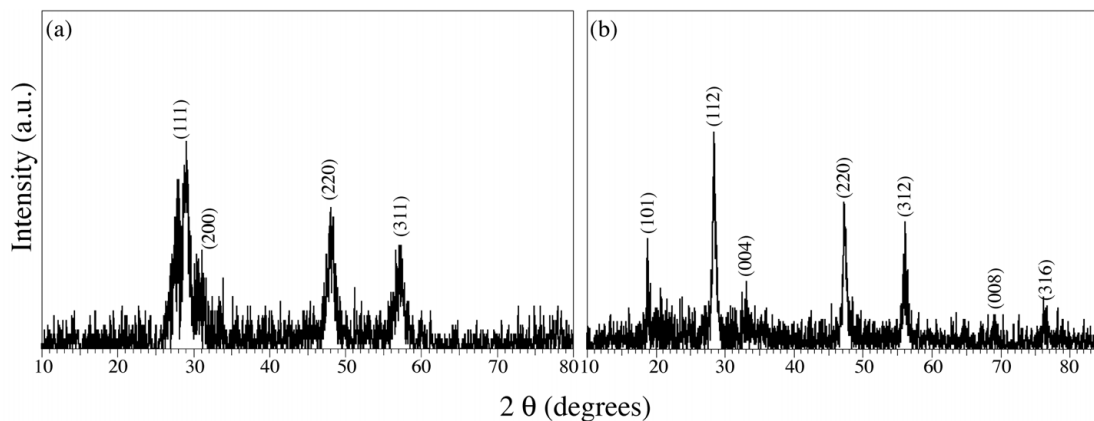


**Figure S4.7.** XRD pattern for the ZnS (a) and Cu<sub>2</sub>SnS<sub>3</sub> (b) nanocrystals. The peaks in (a) have been indexed to cubic ZnS (JCPDS 5-0566), and the peaks in (b) were indexed to tetragonal Cu<sub>2</sub>SnS<sub>3</sub> (JCPDS 01-089-4714).

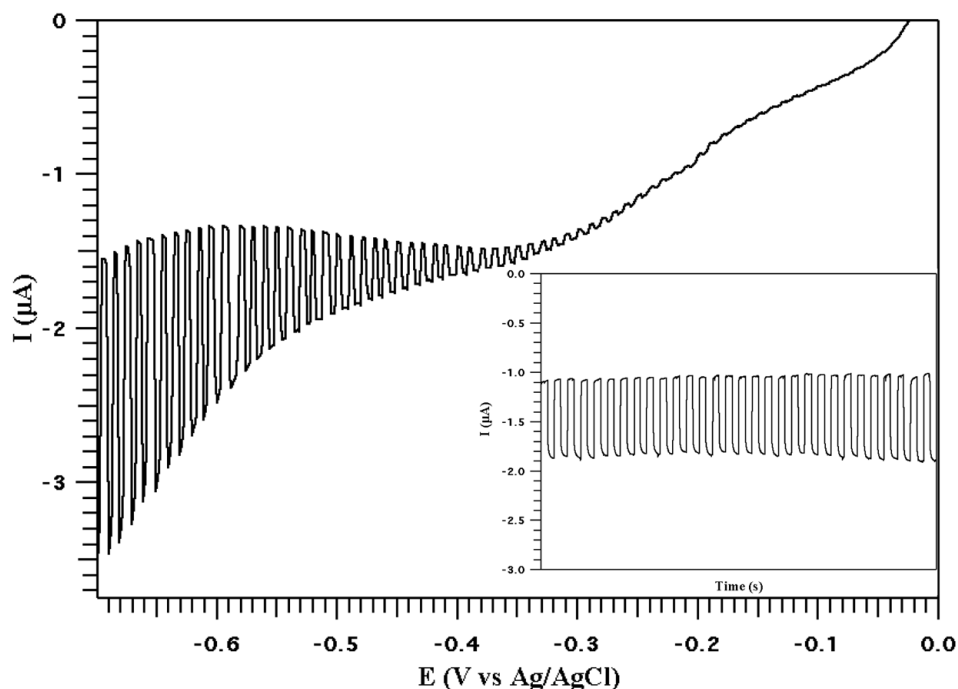


**Figure S4.8.** Current-voltage plot of a CZTS nanocrystal thin film. Films were prepared by a method similar to that reported in [11], in which an FTO-substrate was first dipped into a solution of CZTS nanocrystals followed by a solution of 0.01M ethanedithiol (EDT) in acetonitrile, and then back into the CZTS nanocrystals. This process was repeated a total of 50 times. The I-V plot shows an onset of photocurrent at 0.1 V vs Ag/AgCl which continues to increase with more negative applied bias. The inset shows the photostability of the CZTS nanocrystal thin film using an applied bias of -0.6 V vs Ag/AgCl over 500 seconds.

## CHAPTER 5

### PHOTOELECTROCHEMICAL CHARACTERIZATION OF NANOCRYSTALLINE THIN FILM $\text{Cu}_2\text{ZnSnS}_4$ PHOTOCATHODES

The contents in this dissertation chapter include the manuscript of a full article published in *ACS Applied Materials and Interfaces* **2011**, *3*, 58-66 and is available online at <http://dx.doi.org/10.1021/am1008584>. This chapter explores the effect of composition on the photovoltaic properties with regards to the copper to zinc ratio. Additionally, the charge carrier transport dynamics in  $\text{Cu}_2\text{ZnSnS}_4$  nanocrystal photocathodes have been studied and a major recombination mechanism has been deduced.

The initial studies and the manuscript were prepared by Shannon C. Riha. Sarah J. Fredrick assisted in the confirmation of the nanocrystal synthesis, fabrication of photocathodes, and collection of photoelectrochemical data, based on one wavelength of light. Yuejiao Liu assisted in the collection of the incident photon to current efficiency data. Justin B. Sambur, Amy L. Prieto, and Bruce A. Parkinson provided intellectual insights, and additionally Amy and Bruce provided editing of the manuscript.

## 5.1 Overview

$\text{Cu}_2\text{ZnSnS}_4$  (CZTS) nanocrystals, synthesized by a hot injection solution method, have been fabricated into thin films by dip-casting onto fluorine doped tin oxide (FTO) substrates. The photoresponse of the CZTS nanocrystal films was evaluated using absorbance measurements along with photoelectrochemical methods in aqueous electrolytes. Photoelectrochemical characterization revealed a p-type photoresponse when the films were illuminated in an aqueous  $\text{Eu}^{3+}$  redox electrolyte. The effects of CZTS stoichiometry, film thickness and low-temperature annealing on the photocurrents from front and back illumination suggest that the minority carrier diffusion and recombination at the back contact (via reaction of photogenerated holes with  $\text{Eu}^{2+}$  produced from photoreduction by minority carriers) are the main loss mechanisms in the cell. Low-temperature annealing resulted in significant increases in the photocurrents for films made from both Zn-rich and stoichiometric CZTS nanocrystals.

## 5.2 Introduction

Interest in the development and commercialization of thin film solar cells has been growing over the past decade due to their low cost and scalability—two key factors needed to make solar technologies competitive with carbon-based fuels.<sup>1</sup> Recent advances in CdTe and  $\text{CuIn}_{1-x}\text{Ga}_x\text{Se}_2$  (CIGS) thin film solar cells have resulted in commercially viable photovoltaic modules.<sup>1-3</sup> Despite having moderate efficiencies, CdTe and CIGS are not amenable for eventual terrawatt-scale production due to the cost and scarcity of Te, In, and Ga.<sup>2-4</sup> Therefore, one major challenge of thin film technology

is to develop materials composed of earth abundant and non-toxic elements that can be used to manufacture efficient photovoltaic devices.

$\text{Cu}_2\text{ZnSnS}_4$  (CZTS) is an emerging solar absorber that is structurally similar to CIGS, but contains only earth abundant, non-toxic elements and has a near optimal direct band gap energy of 1.4-1.6 eV and a large absorption coefficient of  $\sim 10^4 \text{ cm}^{-1}$ .<sup>4-6</sup> Katagiri and co-workers have fabricated CZTS thin film solar cells by sputtering and vapor deposition techniques with efficiencies of up to 6.7%.<sup>4,7</sup> However, these methods for thin film fabrication are costly, have low throughput, and can lead to inhomogeneous film composition.<sup>8</sup> To reduce fabrication costs and overcome these drawbacks, many groups have employed other methods for thin-film solar cell fabrication such as spray pyrolysis,<sup>9,10</sup> sol-gel sulfurization,<sup>11-14</sup> electro- and photo-chemical deposition followed by sulfurization,<sup>2,15</sup> and liquid-precursor deposition.<sup>16</sup> Kamoun and Kumar reported the spray pyrolysis of CZTS thin films using metal salts and thiourea precursors sprayed directly onto heated substrates.<sup>9,10</sup>  $\text{Cu}_x\text{S}$  impurities were found in films fabricated using various substrate temperatures and deposition times, while Kumar reported the films were Zn-rich and S-deficient. Uchiki and co-workers utilized a sol-gel method that involved spin-casting and drying CZTS precursor solutions containing metal salts, a solvent, and a stabilizer.<sup>11-14</sup> After the sol-gel had been spin-cast onto the substrate, the precursor films were annealed in  $\text{N}_2 + \text{H}_2\text{S}$  gas at 500 °C for 1 h. The resulting films contained near-stoichiometric CZTS; however, due to the high vapor pressure of sulfur, they were sulfur deficient.

Another low-cost and scalable alternative to vacuum deposition is electrodeposition of the metals followed by a thermal reaction in sulfur vapor.<sup>15,17-23</sup> Scragg, et al. earlier

reported the electrochemical deposition of metal layers where the film thickness was monitored by the charge passed.<sup>2</sup> Films consisting of a 1 mm thick, three layer stack of Cu, Sn, and Zn were annealed at 550 °C in a quartz tube furnace for 2 hrs in a sulfur atmosphere. The authors reported that the films were predominately CZTS but had trace amounts of binary impurities such as SnS<sub>2</sub> and ZnS. In all cases the films were Zn-rich but the Zn composition varied across the film. Recently the authors reported using a rotating disk electrode and a Cu/Sn/Cu/Zn stack followed by sulfurization, which lead to a more uniform Cu<sub>2</sub>ZnSnS<sub>4</sub> composition with small amounts of Cu<sub>2</sub>S impurities.<sup>17</sup> Alternatively, Pawar, et al. reported a similar synthesis method involving a single-step electrodeposition of all elements to eliminate the post sulfurization process. In order to obtain a crystalline sample, the authors reported annealing the films at 550 °C under Ar for 1 h.<sup>18</sup> Although all of the above-mentioned methods offer a cost-effective and scalable alternative to vacuum deposition techniques of CZTS thin films, a majority of the techniques require additional annealing in a sulfur atmosphere at temperatures above 500 °C and the film stoichiometries obtained were not consistent and often contained binary and ternary impurity phases.

Recently Todorov et al. reported a liquid processed, slurry-based coating method for fabricating high performance solar cell devices of Cu<sub>2</sub>ZnSn(S,Se)<sub>4</sub> reaching 9.6% efficiency without any H<sub>2</sub>S processing step.<sup>19</sup> Their process allowed for the in situ formation of CZT(S,Se) directly onto a conducting substrate simply by combining a slurry of Cu-Sn chalcogenides in hydrazine with Zn-chalcogenide precursors (ZnX(N<sub>2</sub>H<sub>4</sub>) where X=S, Se, or Te). One drawback of this technique is that in order to crystallize the precursors into single-phase CZTS, the process required annealing at 540 °C, leaving

minimal control over impurity phases. Fischereder et al. presented a similar method using solutions of metal salts and thioacetamide, which allowed for lower annealing temperatures (180-450 °C).<sup>16</sup> However, they could not rule out the presence of impurity phases in the lower temperature annealed samples.

To overcome the issues addressed above, a new method for scaling up solar cell production is based on nanocrystal “inks,” a printable solution of nanocrystals, which can either be thermally annealed into larger grain thin films or used as deposited to make solar cells using 3-D arrays of photoactive nanocrystals.<sup>20,21</sup> The idea of having a printable ink has spurred interest in the synthesis of ternary nanocrystals such as  $\text{CuIn(S,Se)}_2$  for photovoltaics.<sup>22-24</sup> Recently, our group,<sup>25</sup> along with others,<sup>26-28</sup> have reported the direct synthesis of quaternary CZTS and CZTSe using the hot injection method, a first step towards developing photoactive nanocrystal arrays from solution-processable inks.<sup>29</sup> However, precise control over the solution phase synthesis (i.e., size, shape, doping concentration), characterization and device fabrication of quaternary nanocrystals is in its infancy. It is therefore necessary to develop methods capable of quickly and effectively screening materials to optimize their syntheses. One way to do this is by using photoelectrochemical (PEC) techniques, which were used for the characterization of CZTS thin films by Scragg and Pawar.<sup>2,18</sup> In addition, Kameyama et al. used PEC measurements to characterize layer-by-layer dipped CZTS nanocrystalline thin films.<sup>30</sup> Herein, we report the fabrication and characterization of thin film photoelectrochemical photovoltaic cells in an aqueous electrolyte utilizing stoichiometric and Cu-poor/Zn-rich CZTS nanocrystal inks.

### 5.3 Results and Discussion

$\text{Cu}_2\text{ZnSnS}_4$  nanocrystals were synthesized using the hot injection solution synthesis method, which has been successful for the syntheses of a wide range of semiconducting chalcogenide nanocrystals, such as  $\text{CdX}$  ( $X=\text{S}, \text{Se}, \text{Te}$ ) and CIGS.<sup>22,24,31,32</sup> We chose this method because it not only provides control over composition and morphology, but also enables low-cost and scalable fabrication of solar cells through drop-casting, dip-coating, spin-coating, or printing the nanocrystals on an appropriate substrate.<sup>22,24,31,33,34</sup> The hot injection method involves the injection of a cold solution of precursors into a hot surfactant solution, initiating the nucleation and growth of the nanocrystals.<sup>32,35</sup> The best reported CZTS photovoltaic conversion efficiencies were obtained when the material was Zn-rich;<sup>4,7,19</sup> therefore, we synthesized CZTS samples that were near stoichiometric along with Zn-rich CZTS. The synthesis was carried out as previously described<sup>25</sup> with slight modifications presented in the Supporting Information. Briefly, appropriate amounts of copper (II) acetylacetonate, zinc acetate, and tin (IV) acetate were mixed under inert conditions in oleylamine (refer to Table S5.1 in the Supporting Information). In a separate vial, sulfur powder and oleylamine were sonicated until a red-orange solution was obtained. The reaction flask, containing trioctylphosphine oxide (TOPO) was heated to 300 °C, followed by the simultaneous injection of the S and metal precursors. The reaction was quenched after 45 minutes by removing the product solution from the reaction flask and injecting minimal amounts of hexanes to prevent solidification when cooled to room temperature.

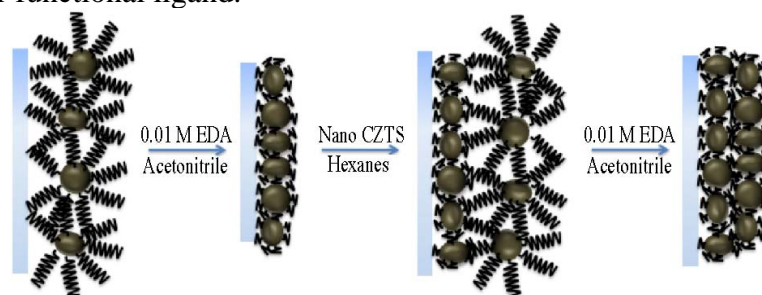
Analysis of the transmission electron microscopy (TEM) images of the resulting CZTS nanocrystals from the two reactions (stoichiometric versus Cu-poor/Zn-rich)

showed that the CZTS particles from both reaction sets exhibit both triangular and spherical morphologies with the spherical morphology being more abundant. (Figure S5.1 in the Supporting Information) The two different morphologies are consistent with the results of Guo, as well as Steinhagen, using similar synthesis procedures.<sup>26,28</sup> Size analysis reveals that the nanocrystals have similar average sizes of  $10.3 \pm 1.3$  nm for the stoichiometric and  $9.7 \pm 1.3$  nm for the Zn-rich composition (Figure S5.1).

To confirm the composition and structure of the CZTS nanocrystals, energy dispersive x-ray analysis (EDX) and x-ray diffraction (XRD) were performed on a solid sample of dried nanocrystals from each reaction. Compositional analysis from EDX reveals a near stoichiometric ratio of  $\text{Cu}_{2.0}\text{Zn}_{1.0}\text{Sn}_{1.1}\text{S}_{3.9}$ , while for the Cu-poor/Zn-rich sample, an average composition of  $\text{Cu}_{1.9}\text{Zn}_{1.2}\text{Sn}_{1.0}\text{S}_{3.9}$  was determined. The XRD patterns (Figure S5.2a) for stoichiometric and Zn-rich samples were indexed to tetragonal  $\text{Cu}_2\text{ZnSnS}_4$  (JCPDS 26-0575, Figure S5.2b), and the average crystallite size, calculated by the Williamson-Hall method, was consistent with the particle size measured in the TEM images. No peaks consistent with  $\text{Cu}_x\text{S}$  or  $\text{SnS}_x$  were present in either pattern; however, it was not possible to rule out the presence of ZnS nor  $\text{Cu}_2\text{SnS}_3$  impurities as their diffraction patterns contain peaks overlapping CZTS. A more in-depth analysis to confirm the phase purity of the CZTS nanocrystals can be found in our previous paper.<sup>25</sup>

Thin films of CZTS nanocrystals, with thicknesses ranging from 50-650 nm, were prepared by a dip-casting procedure similar to that reported by Nozik and co-workers.<sup>29,36</sup> Glass slides with a 400 nm layer of fluorine-doped tin oxide (FTO) were used as a conducting substrate. The FTO substrates were mechanically dipped at a rate of 260 mm/min into a concentrated suspension of CZTS nanocrystals in a hexanes/toluene

**Scheme 5.1.** Ligand exchange mechanism for the in situ replacement of bulky insulating ligands (introduced from the synthetic method) to a short chain (less insulating) bi-functional ligand.



mixture, and then slowly removed from the suspension and allowed to dry. To remove the insulating TOPO capping ligands an in situ ligand exchange was performed by dipping the substrate into a 0.01 M solution of ethylenediamine (EDA) in acetonitrile followed by slow removal and drying. The FTO substrate was then dipped back into the solution of nanocrystals and the process was repeated until a desired thickness was obtained. It has been shown that short chain ligands in acetonitrile will replace long chain ligands, which in turn decreases inter-nanocrystal spacing, Scheme 5.1, thereby facilitating the charge transfer through the nanocrystal film.<sup>37,38</sup> ATR-IR spectra taken of films prepared without ligand exchange show a stretch around  $1140\text{ cm}^{-1}$ , corresponding to phosphine oxide (Figure S5.3). This suggests that the particles are TOPO capped. The ATR data for the ligand exchanged films do not show this stretch. Rather, peaks were present at  $1000\text{ cm}^{-1}$  and  $890\text{ cm}^{-1}$  corresponding to the  $\nu\text{CN}$  stretch and  $\nu\text{NH}$  bend of ethylenediamine.<sup>39</sup> There is also an  $\text{NH}_2$  stretch at  $3200\text{ cm}^{-1}$ ; however, the resolution is low, making this a difficult stretch to observe. Overall the IR data supports the proposed ligand exchange mechanism in Scheme 5.1.

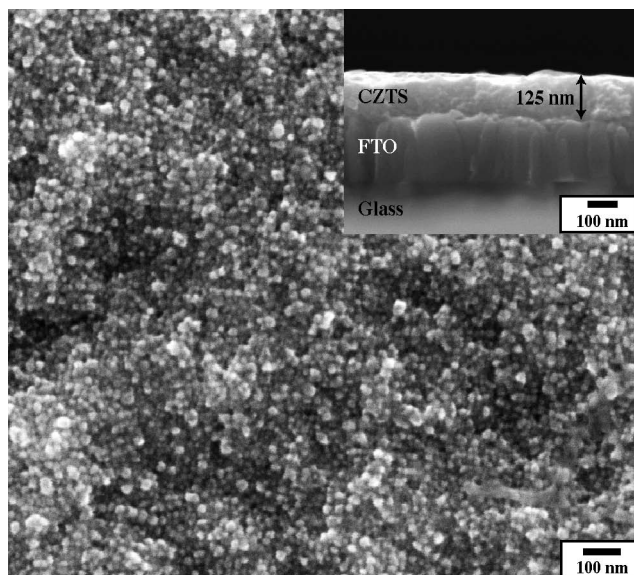


**Figure 5.1.** SEM image of a CZTS film prepared by dip-casting with an *in-situ* ligand exchange to EDA. The top profile shows the CZTS nanocrystals are tightly packed. The inset is the side profile of the film, which is 150 nm thick.

Figure 5.1 shows representative scanning electron microscopy (SEM) images of the surface and cross section of an as-prepared CZTS nanocrystal thin film. The top view image reveals that the nanocrystals are densely packed and distributed evenly throughout the entire surface of the film and that it is devoid of cracks. The cross-sectional image of a CZTS nanocrystal thin film dipped 20 times is shown in the inset of Figure 5.1 and shows that the film is approximately 125 nm thick. Considering the particles are ~10 nm in diameter, this implies that each successive dip resulted in submonolayer deposition of nanocrystals.

Optical absorbance measurements were also used to monitor the thickness of the nanocrystal films. Figure 5.2 (solid lines) displays the UV-vis spectra of as-deposited thin films from each reaction that were used to determine an absorption coefficient. Extrapolating the linear portion of the plot  $(\alpha h\nu)^2$ —the square of the absorption coefficient ( $\alpha$ ) multiplied by the photon energy ( $h\nu$ )—versus the photon energy yields

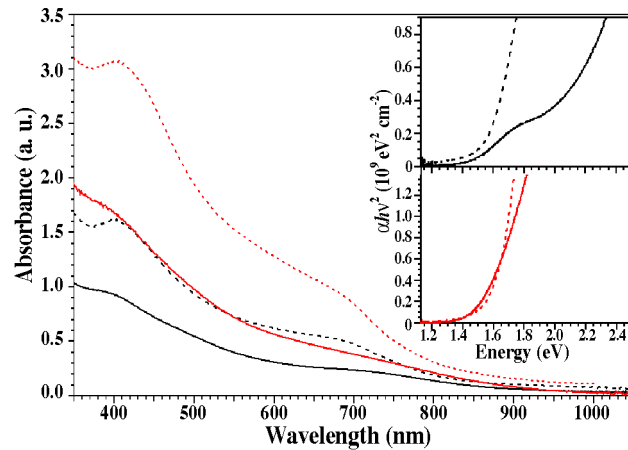


**Figure 5.2.** Optical absorption measurements of as-deposited (solid lines) and annealed (dashed lines) CZTS thin films. The black traces correspond to a 150 nm thick stoichiometric CZTS film and the red traces are for a 20 nm thick Zn-rich film. The absorption coefficient at the band gap is larger for the Zn-rich composition. Upon annealing, the band gaps slightly increase and become more direct.

direct band gaps of 1.45 eV and 1.52 eV for stoichiometric (black solid trace) and Zn-rich compositions (red solid trace), respectively. These values are consistent with literature values and are near optimal for solar conversion efficiency in a single junction device.<sup>4-6</sup> Unpassivated nanocrystal surfaces have surface states that allow for transitions leading to the small absorption at sub-band gap energies. In addition, atomic disorder in the crystal structure can result in defect states that shift the band gap to lower energies, producing an indirect band gap not present in the ordered bulk crystal. One way to induce order within the nanocrystals is through annealing. Therefore, after dip casting, films were annealed under Ar in the presence of additional CZTS nanopowder at 350 °C (1000 Torr) for 1.5 h. The heat treatment, even though it is only 50 °C hotter than the synthesis temperature, drastically changed the absorbance of the CZTS films to have a much steeper onset or more like a direct transition (Figure 5.2, dashed lines). In addition, the band gap slightly increased to 1.56 and 1.59 eV for the stoichiometric and Zn-rich analogs, respectively.

Possible explanations for these optical absorption changes are that low-temperature annealing leads to ordering within the nanocrystal, at a lower temperature than would be expected for macroscopic crystals, and that the annealing step leads to grain growth which reduces the number of sub-band gap surface states. We can test the hypothesis for grain growth with SEM and XRD. SEM images show that after annealing, the film thickness (Figure S5.4) decreases from about 440 nm to 340 nm or by about 20%, indicating that the nanocrystals are more densely packed. In addition, Scherrer analysis of the x-ray diffraction patterns of an as-deposited film and a film annealed 1.5 h at 350 °C revealed an increase in average grain size from  $12.7 \pm 1.0$  nm, consistent with the TEM results, to  $47.8 \pm 11.1$  nm, an almost 4-fold increase that may reduce the number of surface states (Figure S5.5). Therefore, the outcome of low temperature annealing results in condensing the film and increases the grain size, reducing the number of grain boundaries and the surface area with potentially fewer surface states. It is also probable that annealing produced more ordering in the metal sublattice, which would increase the density of states at the  $\Gamma$  point and correspond to the direct optical transition observed in the UV-vis. This may account for the up to a factor of 10 increase in the optical absorption despite the same amount of CZTS material in the optical path length. Similar effects were observed when cation disorder was present in the chalcopyrite structure of  $\text{ZnSnP}_2$  resulting in an indirect band gap at lower energies rather than a direct gap in the ordered material.<sup>40</sup>

We next investigated the photoresponse of the as-deposited films and compared them with the annealed thin films to determine if the improvements in absorption properties and changes in morphology lead to better photoelectrochemical properties. The

nanocrystalline films, both as-dipped and annealed, were used as photoelectrodes in a 3-electrode photoelectrochemical cell with a platinum mesh basket counter electrode and saturated Ag|AgCl reference electrode. The electrolyte contained aqueous 0.1 M KCl and 0.1 M Eu(III)(NO<sub>3</sub>)<sub>3</sub> which served as the redox mediator. The photocurrent, produced by illuminating the films with a chopped ~17 mW 532 nm green laser, was measured using a CH-Instruments potentiostat.

Photoelectrochemical characterization was chosen over preparing solid-state devices as it allows for a rapid, non-destructive evaluation of the CZTS thin films and eliminates electrical shorting from a vapor-deposited metal back contact penetrating through the pores in the film to the front contact. In addition, the conformal contact of electrolyte with the nanocrystals in the film minimizes the distance minority carriers (electrons) must diffuse to reduce the Eu<sup>3+</sup> to Eu<sup>2+</sup> before they can recombine with the photogenerated holes. The solution-based measurements allowed us to quickly test a variety of films in order to determine the optimal thickness and composition, as well as compare as-deposited and annealed films.

Figure 5.3a shows a current-voltage (IV) curve of an as-deposited, stoichiometric, 205 nm thick CZTS nanocrystal thin film. The cathodic photocurrent increased gradually with increasing negative potential, indicating that the thin films were p-type.<sup>2</sup> In a solid thin film, this would be attributed to an increase in the depletion layer thickness; however, the size of the nanocrystals cannot support a depletion layer since the space charge region is large compared to the particle size and the mobile ions in the electrolyte neutralize any electric field. The reduction potential of Eu<sup>3+</sup> to Eu<sup>2+</sup> is -550 mV vs Ag | AgCl so we attribute the increase in dark current at potentials more negative than -550

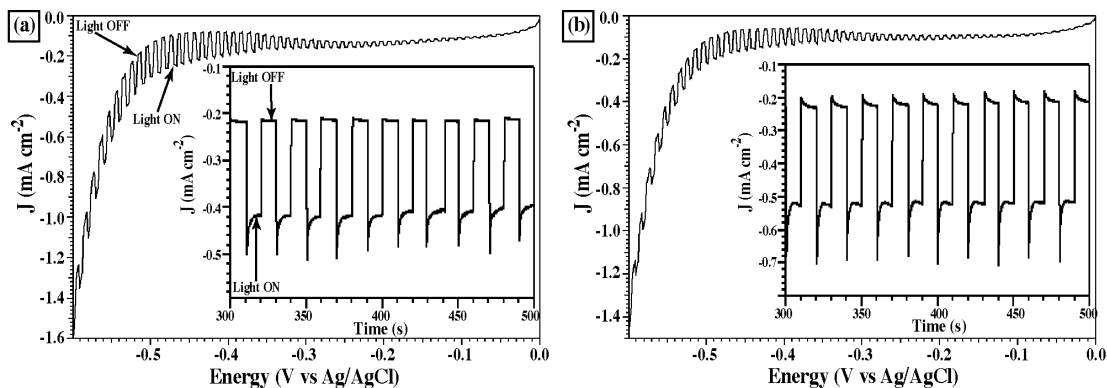


**Figure 5.3.** J-V plots of the photocurrent response of 205 nm thick, stoichiometric (a) and Zn-rich (b), as-deposited CZTS nanocrystal thin films scanned cathodically from 0 to -600 mV vs Ag | AgCl at a scan rate of 2 mV/s using a 17 mW, 532 nm laser. The photocurrents increased with a more negative applied potential for both reactions. The insets are photo-stability measurements at -500 mV vs Ag|AgCl showing the photocurrent is quite stable at this potential. Both experiments were performed in a 0.1 M  $\text{Eu}(\text{NO}_3)_3$  aqueous electrolyte.

mV to the reduction of  $\text{Eu}^{3+}$  to  $\text{Eu}^{2+}$  on the film and on the FTO substrate. For this reason, we focus on photocurrents produced at potentials more positive of -550 mV where photogenerated carriers in CZTS are from the uphill reduction of  $\text{Eu}^{3+}$ .

The stability of the photocurrent of an as-deposited thin film was evaluated at a constant potential of -500 mV by chopping the light with 10 sec on and 10 sec off, and the results are plotted in the inset of Figure 5.3a. The CZTS nanocrystal film showed a constant photocurrent-density of  $0.19 \text{ mA cm}^{-2}$  that remained stable over time despite being immersed in an aqueous electrolyte. Similar results were also obtained with thin films of the Cu-poor/Zn-rich CZTS nanocrystals as displayed in Figure 5.3b (as-deposited). This composition showed a slightly higher photocurrent-density response than the stoichiometric CZTS nanocrystals, consistent with current CZTS thin film literature.<sup>4,7</sup> The same photostability test (Figure 5.3b inset) showed a stable photocurrent-density of around  $0.3 \text{ mA cm}^{-2}$ .

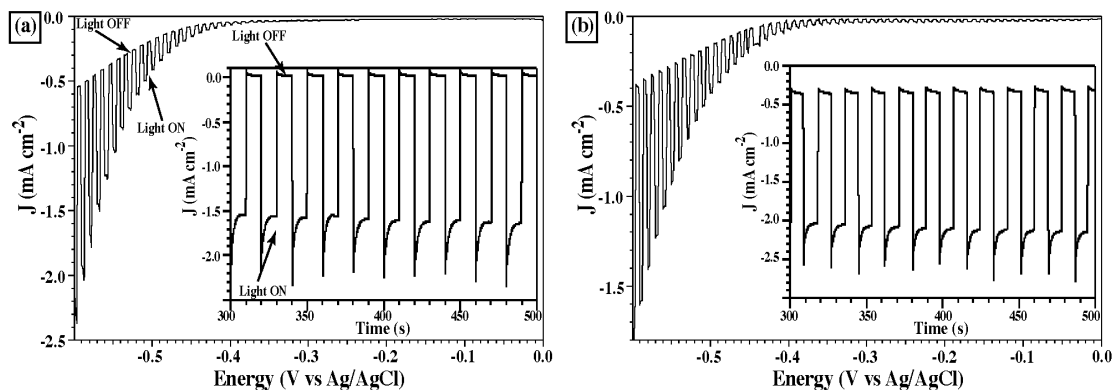


**Figure 5.4.** J-V plots of the photocurrent response from annealed, 150 nm thick CZTS nanocrystal thin films from stoichiometric (a) and Zn-rich (b) reactions, with the insets displaying the photostability measurements using a 0.1 M  $\text{Eu}(\text{NO}_3)_3$  aqueous electrolyte. The dark current is reduced compared to the as-deposited films and the photocurrent density increases with a more negative applied potential. The annealed thin films both produced close to a 10-fold increase in the stable photocurrent density at -500 mV vs Ag|AgCl under illumination from a 17 mW, 532 nm laser.

As was previously displayed in the UV-vis spectra (Figure 5.2), annealing the CZTS nanocrystal thin films at 350 °C leads to better absorption properties and a more direct band gap transition. As-deposited films, similar to those tested in Figure 5.3a, were annealed at 350 °C for 1.5 h under 1000 Torr of Ar. The film thickness for each sample decreased by about 20% (Figure S5.4b). Figure 5.4a shows the current-density voltage curve of an annealed stoichiometric CZTS nanocrystal thin film, while Figure 5.4b displays the current-density voltage plot of an annealed Zn-rich CZTS nanocrystal thin film (220 nm) under illumination from a 17 mW, 532 nm laser. In comparison to the as-deposited films, the dark current is considerably reduced and the photocurrent density increases more rapidly. The SEM images show that the thin films became more condensed, resulting in the area of the exposed conducting substrate and dark current being reduced (Figure S5.4). The insets of Figure 5.4a and 5.4b again show the photostability tests for both sets of annealed thin films using the same 532 nm laser source. From the as-deposited to the annealed films, there is an almost 10-fold increase

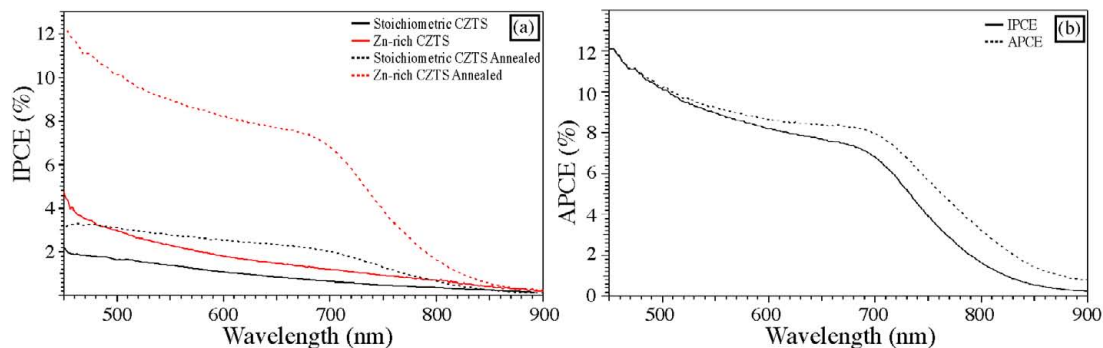


**Figure 5.5.** (a) IPCE measurements taken of as-deposited (solid) and annealed (dashed) stoichiometric CZTS film (black trace) and Zn-rich film (red trace). The measured IPCE mirrors the UV-vis and shows a more direct onset of IPCE for the annealed films. At 500 nm the IPCE for the stoichiometric film was 1.8% and 3.1% for as-deposited and annealed respectively. The IPCE increased for the Zn-rich composition from 2.8% (as-deposited) to 10.1% (annealed film). (b) APCE values (dashed line) calculated from the IPCE and LHE values of an annealed Zn-rich CZTS film.

in photocurrent density to 1.65 and 1.8 mA cm<sup>-2</sup> for both the stoichiometric and Cu-poor/Zn-rich CZTS reactions, respectively. All the chopped photocurrents show decay transients indicative of recombination of photogenerated carriers through mechanisms that will be discussed below.

To study the effects of low-temperature annealing and stoichiometry on the spectral response of the films, we measured the incident photon to current efficiency (IPCE) spectra of the CZTS nanocrystal thin films at -0.35 V vs Ag|AgCl in 0.05 M Eu<sup>3+</sup> (pH 4). For comparison we show the results from the stoichiometric as-deposited film (black solid trace) and the Zn-rich as-deposited film (red solid trace) in Figure 5.5. The IPCE for the stoichiometric CZTS film is 1.8% at 500 nm, whereas the IPCE for the Zn-rich CZTS film is 2.8% at 500 nm. The increase in IPCE for the Zn-rich sample was consistent with the photocurrent measurements above, as well as with previous reports.<sup>6,7,19,41</sup> However, these values are rather low and do not exhibit a sharp onset of

photoresponse when compared to those reported by Katagiri and Todorov for CZTS thin films.<sup>7,19</sup>

From Figure 5.5 it is clear that after annealing, the CZTS films of both the stoichiometric (dashed black curve) and the Zn-rich composition (dashed red curve) show a significantly enhanced photocurrent response. The onset of photocurrent is more pronounced with an overall increase of IPCE throughout the visible region for both annealed films but especially in the Zn-rich sample. In fact, at 500 nm the IPCE for the stoichiometric composition showed an increase from 1.8% to 3.1% after annealing whereas the Zn-rich composition exhibited an over 3.5 times increase from 2.8% to 10.1%. Based on the UV-vis absorption spectra in Figure 5.2, the absorption coefficients for the Zn-rich sample are larger than those for the stoichiometric sample leading to better light absorption over all wavelengths.

Although annealing produced significant improvements in the photoresponse of the nanocrystal films, the values are less than those measured in polycrystalline thin film CZTS devices. Photocurrents in a photoconversion system depend on the separation of carriers in a space charge field, diffusion lengths and recombination velocities of the photogenerated carriers.<sup>42</sup> Since the nanocrystals are immersed in an electrolyte containing mobile ions, a space charge field is not present since it will be cancelled by the mobile ionic charges. Therefore these devices should act much like the dye sensitized solar cell (DSSC), which operates on chemical potential gradients rather than electric field gradients. The majority carrier holes (in a typical DSSC they are electrons) must diffuse through the nanocrystal network to be collected at the back FTO contact before they can recombine with a photogenerated electron or reoxidize  $\text{Eu}^{2+}$  in the electrolyte.

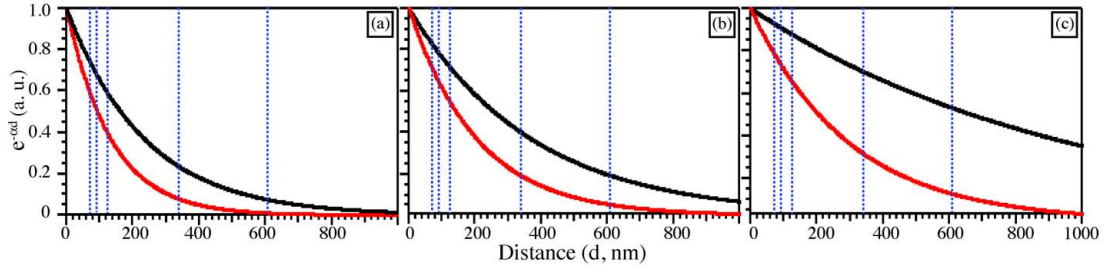


**Figure 5.6.** Absorption profiles calculated based on  $\exp(-\alpha d)$ , where  $\alpha$  is the absorption coefficient for (a) 473 nm, (b) 532 nm, and (c) 632 nm and  $d$  is the distance. The red traces correspond to the Zn-rich annealed films, while the black traces are for the stoichiometric annealed films. Nearly 80% of the incident short wavelength light is absorbed in the first couple hundred nanometers of the film but as the wavelength increases, the light penetrates deeper into the films and more passes through the film. The blue traces indicate the various film thicknesses tested.

The diffusion of carriers depends on the concentration gradients in the device as well as the number and energy distribution of recombination centers. The absorption profile of the incident light defines the concentration profile for the photogeneration of carriers and can be calculated by plotting  $e^{-\alpha d}$ , where  $\alpha$  is the absorption coefficient, as a function of distance,  $d$ . The absorption profiles for our films calculated for three different wavelengths, 473 nm, 532 nm and 632 nm, are shown in Figure 5.6 where the red curves are for the Zn-rich annealed films and the black curves represent the stoichiometric annealed films. The photocurrent in these devices, as in many thin film solar cells, is a trade off between absorbing all the light in a thicker film and collecting the majority carriers at the back contact via diffusion through the film. The majority carrier diffusion is particularly problematic in nanocrystal devices since they must traverse a tortuous path through many nanocrystals where interface states can act as recombination centers. Since the nanocrystal devices are porous and immersed in a redox electrolyte the collection of the minority carriers should be relatively facile because they need to diffuse at most only

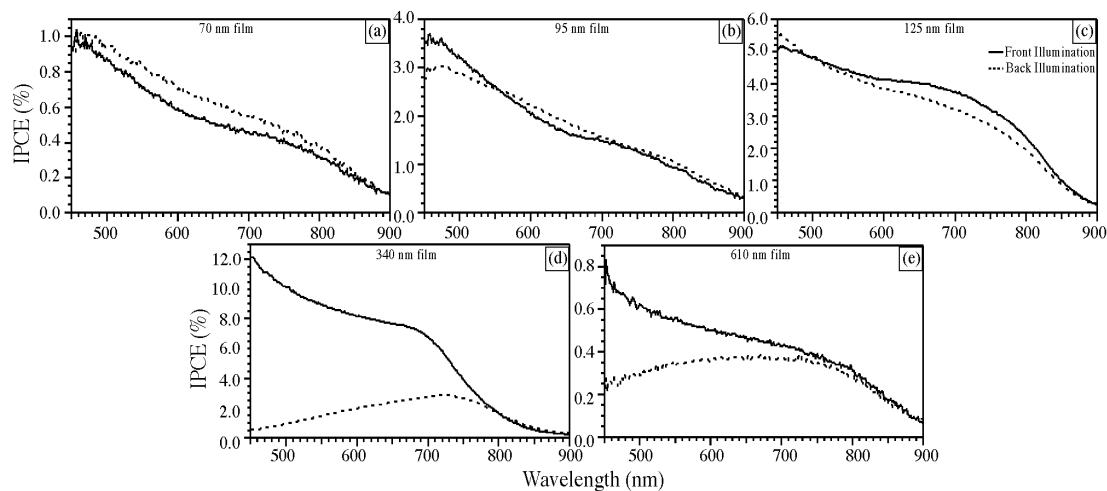


**Figure 5.7.** Photocurrent spectra recorded as a function of Zn-rich annealed films of various thickness with front and back illumination. The film thicknesses investigated were (a) 70 nm, (b) 95 nm, (c) 125 nm, (d) 340 nm, and (e) 610 nm.

half the distance of the nanocrystal diameter, less than 10 nm for the as-deposited films and between 15 and 25 nm for annealed film, to reduce a  $\text{Eu}^{3+}$  to  $\text{Eu}^{2+}$ .

We can estimate the diffusion length of holes by examining the absorbed photon to current efficiency (APCE), a function of the IPCE values for the 340 nm thick film. The APCE, shown in Figure 5.5b, is calculated by taking the IPCE and dividing it by the light harvesting efficiency (LHE), where LHE is equal to  $1 - 10^{-\text{Abs}}$ . In our case the best films have higher APCE values at all wavelengths beyond 550 nm and nearly identical APCE as IPCE values at lower wavelengths. According to the absorption profiles in Figure 5.6, at longer wavelengths of light, photogenerated charge carriers are produced throughout the film, requiring the holes to have much shorter diffusion lengths. On the contrary, based on the APCE value at 473 nm and Figure 5.6a, for front illumination, 80% of the light at this wavelength is absorbed and creates most of the charge carriers in the first 250 nm of the film. Therefore most of the collected holes at the back contact must have diffused over 100 nm, an impressive distance for such a disordered low band gap

nanocrystal film. However, in comparison the electrons in a nanocrystalline TiO<sub>2</sub> cell can diffuse many microns.

To elucidate the role of carrier diffusion in these devices we measured IPCE spectra for both front illumination and back illumination (through the transparent substrate) in the redox electrolyte. Figure 5.7 shows a series of the front and back illumination IPCE spectra for the non-stoichiometric (Zn-rich) annealed film with film thicknesses ranging from 70 nm to 610 nm. The thinner 70 nm, 95 nm and 125 nm thick films in 5.7(a-c), show only small differences in the shape of the IPCE spectra when illuminated from the back or the front but with an increase in the overall IPCE values as the films get thicker. The absorption profiles in Figure 5.6 reveal that a majority of the light still passes through the film resulting in a more uniform generation of carriers throughout the film and thus there is very little difference in the ability of the minority carriers to reach the back contact. However, once the film thickness increased to 340 nm (Figure 5.7d), there is a striking difference between front and back illumination. Longer wavelengths gave similar IPCE values for both front and back illumination but as the wavelength decreases, IPCE values for front illumination continued to increase whereas for back illumination the IPCE values decreased more than an order of magnitude when compared to front illumination. A similar trend was also observed for a 610 nm thick film but with much smaller IPCE values at all wavelengths as shown in Figure 5.7e. Figure 5.8 summarizes IPCE values taken from plots Figure 5.7a-e at 473 nm, 532 nm, and 632 nm as a function of film thickness showing that as the film thickness increases the IPCE values produced from front illumination increased almost linearly up until a film thicknesses of 340 nm and then decreased for a thicker 610 nm film whereas the back illumination IPCE values

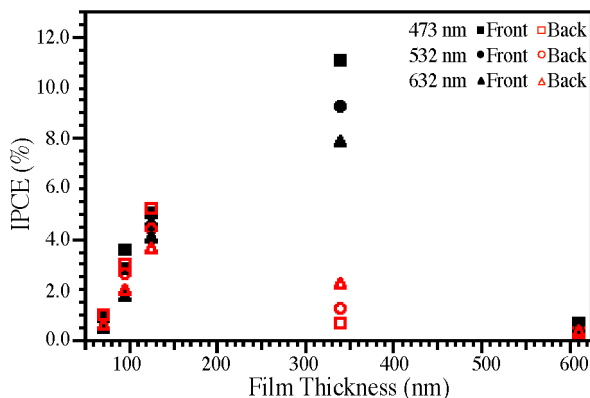


**Figure 5.8.** Plot of the IPCE values for both front (solid) and back (open) illumination at 473 nm (squares), 532 nm (circles), and 632 nm (triangles) wavelengths taken from the data in Figure 5.7. There is a general increase in front illuminated IPCE values with increasing film thickness up to 350 nm, after which the IPCE values significantly decrease. Back illumination IPCE values follow the same trend for films thinner than 125 nm, but as the film thickness increase the IPCE values deviate substantially from those produced by front illumination.

only increased until the film thickness reached 125 nm and then decreased. At film thicknesses up to 125 nm, front and back illumination give similar IPCE values.<sup>43</sup>

The absorption profiles in Figure 5.6 show that the majority (>80%) of the incoming light is absorbed when the film is thicker than 200 nm for 473 nm illumination, 260 nm for a 532 nm illumination and almost 450 nm at 632 nm illumination. The greater light absorption in the thicker films produces both more total photogenerated carriers and a concentration gradient of carriers across the film, the direction of which is determined by the illumination direction. These trends can be understood by considering the absorption profiles shown in Figure 5.6. The thinner nanocrystal films will have low light absorption at all wavelengths resulting in nearly uniform generation of electron-hole pairs in the film with either front or back illumination and relatively small photocurrents. The redox couple can easily scavenge the small concentration of minority carriers, resulting in very low concentrations of reduced europium, and the holes have a relatively short distance to diffuse to the back FTO contact. As the films get thicker the majority of the

electron-hole pairs are created near the front or back of the film depending on front or back illumination respectively, especially for the short wavelengths where the extinction coefficient is largest. The thicker films show nearly identical front and back illumination IPCE values in their photoresponse spectra at wavelengths red of about 780 nm where the light is not strongly absorbed. The large decrease in photoresponse from back illumination in the blue region of the spectra is most likely due to recombination at the back contact. A large concentration of photogenerated electrons created near the back contact will produce a high concentration of  $\text{Eu}^{2+}$  near this contact. If the exchange current density for the usually slow electron transfer reaction of the  $\text{Eu}^{3+}/\text{Eu}^{2+}$  couple is much faster on the FTO surface than on the CZTS surface then the holes that make it to the back contact will simply reoxidize the  $\text{Eu}^{2+}$  created from the photogenerated electrons. This usually slow electron transfer reaction must not have a high exchange current on semiconducting CZTS due to the low dark currents in pure  $\text{Eu}^{3+}$  solutions, especially considering the extremely high surface area of the nanocrystal films.

Kinetic discrimination of redox processes is similar to the DSSC where the  $\text{TiO}_2$  surface has very slow kinetics for reduction of triiodide and the cells are very inefficient with faster redox couples such as ferrocene/ferrocenium or when fabricated on bare metal substrates. Indeed a much faster redox mediator, the reduction of cobaltacenium to cobaltacene ( $\text{Co(III)/Co(II)}$ ), with our CZTS nanocrystal thin film produces very poor photoresponse when in our CZTS films because the holes will quickly reoxidize any cobaltacene that was produced by photoreduction (Figure S5.6). One way to improve the device efficiency by slowing the electron transfer reaction is by using a blocking layer on the back contact. Indeed, the DSSC efficiency is improved by coating the conducting

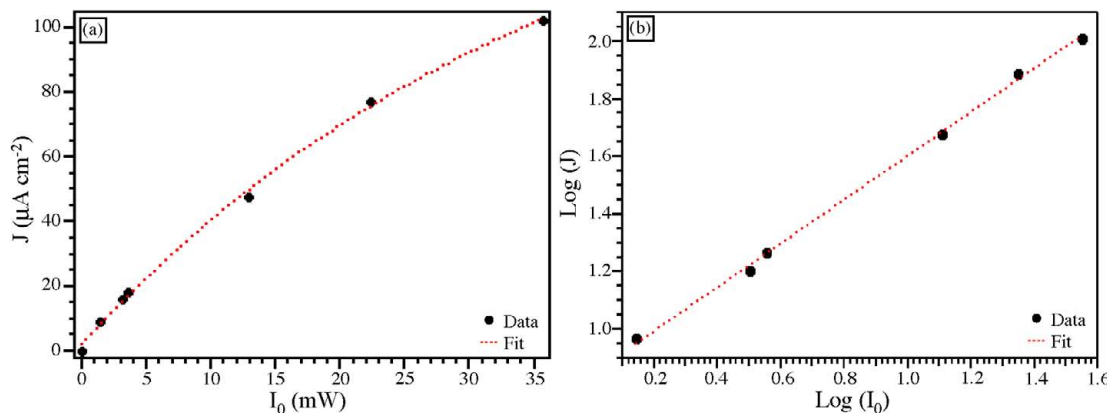


**Figure 5.9.** Steady-state photocurrent density, recorded 8 s after illumination from a 532 nm light source, as a function of light intensity at -500 mV vs Ag|AgCl. The data is plotted on (a) a linear scale and (b) in a log-log plot. The data in the log-log plot has a slope of 0.75 ( $R^2=0.999$ ).

oxide back contact with a thin layer of  $\text{TiO}_2$ .<sup>48,49</sup> The addition of a thin blocking layer to the FTO surface, which has a low exchange current density for the  $\text{Eu}^{3+}/\text{Eu}^{2+}$  couple, is currently under investigation to improve the photoresponse in our devices.

However, additional recombination processes in these films may be occurring as suggested by the low APCE values, calculated from the IPCE and LHE results, for the CZTS nanocrystal thin films. Some insight into these processes can come from the light-intensity ( $I_0$ ) dependence of the photocurrent density ( $J$ ) because at reasonable light intensities there is a linear relationship between these parameters. Since all the photocurrents in our CZTS films show a transient response that decays to a more steady state value (Figures 5.3 and 5.4) it is apparent that there is a fast recombination process that may not be associated with the timescale for carrier diffusion. The results of the intensity dependence of the steady state photocurrent, measured 8 seconds after illumination in a 0.1 M Eu(III) electrolyte, for the 340 nm thick films at an applied bias of -500 mV vs Ag|AgCl are presented in Figure 5.9. In an ideal system the short-circuit,

$J_{SC}$ , scales linearly with  $I_0$  however Figure 5.9a shows that it is not linear in our devices. Figure 5.9b shows the same data plotted on a log-log scale where a linear dependence is observed with a slope of 0.75 ( $R^2=0.999$ ). Recombination is often a second order process, since it is dependent on both the concentration of electrons and holes, but in our case it may also be influenced by the diffusion of  $Eu^{3+}$  and  $Eu^{2+}$  that react with minority and majority carriers respectively resulting in a power dependence close to 0.75. Further investigation of the time, potential and intensity dependence of the transient photocurrents will be necessary to elucidate the competing recombination pathways in these devices.

#### 5.4 Conclusions

Stoichiometric and Cu-poor/Zn-rich CZTS nanocrystals have been synthesized using the hot-injection method. We have shown that CZTS nanocrystal thin films, fabricated by dip casting onto FTO substrates and ligand exchanged with ethylenediamine and immersed in a  $Eu^{3+}$  containing redox electrolyte, exhibit p-type photocurrents that increase with negative applied bias. The influence of film thickness and low temperature annealing on the photocurrent response was studied on both stoichiometric and Zn-rich films. Low-temperature annealing of the as-deposited films at 350 °C for 1.5 h greatly improved the IPCE for both the stoichiometric and Zn-rich CZTS films from 1.8% to 3.1% (stoichiometric) and 2.8% to 10.1% (Zn-rich) at 500 nm respectively. Although these photoconversion efficiencies are low in comparison to the bulk counterparts, our studies were aimed at investigating the carrier transport processes in the semiconducting nanocrystalline thin films. Optical absorbance measurements and photocurrent

spectroscopy with both front and back illumination revealed that the CZTS nanocrystal thin films behave like a p-type version of the nanocrystalline TiO<sub>2</sub> scaffold in a dye sensitized solar cell, and that a major loss mechanism in this cell is recombination via the redox couple at the back contact. This is due to oxidation of Eu<sup>2+</sup> produced by the photogenerated electrons with the photogenerated holes diffusing to the back contact, which is due to the higher exchange current for this redox couple on FTO than on the surface of the CZTS nanocrystals.

## 5.5 Experimental Details

**CZTS Nanocrystal Synthesis.** Copper(II) acetylacetonate (Cu(acac)<sub>2</sub>, Aldrich, 99.99%), tin(IV) acetate (Sn(OAc)<sub>4</sub>, Aldrich), zinc acetate (Zn(OAc)<sub>2</sub>, Fisher), sulfur powder (S, Aldrich), trioctylphosphine oxide (TOPO, Aldrich, 99%), and oleylamine (OLA, Aldrich, 70%) were purchased and used as received. All reaction conditions were kept inert to prevent the formation of an oxide. For stoichiometric CZTS, 0.50 mmol Cu(acac)<sub>2</sub>, 0.25 mmol Zn(OAc)<sub>2</sub>, 0.25 mmol Sn(OAc)<sub>4</sub>, and 4 mL OLA were prepared in a 25 mL 3-neck round-bottom reaction flask and heated under vacuum to 150 °C for 15 minutes. The temperature was lowered to 125 °C and the mixture remained at this temperature under vacuum until injection. In a 20 mL scintillation vial, 1.0 mmol S powder and 1 mL OLA was sonicated until the S had dissolved. In a 50 mL 3-neck round-bottom reaction flask, 10 mmol TOPO was heated to 300 °C on an Ar Schlenk line. When the TOPO reaction temperature reached 300 °C, simultaneously the S and metal precursors were rapidly injected via two gas-tight Luer-Lock syringes. The reaction was quenched at 45 minutes by extracting the product solution from the reaction

flask and adding minimal amounts of hexanes to prevent it from solidifying when cooled to room temperature. Methanol was added to the product, which was subsequently centrifuged to precipitate the particles from solution. The CZTS nanocrystals were washed 3x with hexanes and methanol, and then resuspended in hexanes. The reaction for Cu-poor/Zn-rich CZTS was similar with adjustments to the precursor ratios, shown in Table S5.1.

**Film Fabrication.** Colloidal suspensions of CZTS nanocrystal ‘inks’ were deposited on fluorine-doped tin oxide (FTO) substrates and assembled into thin films according to the layer-by-layer method (LbL).<sup>37,38</sup> The FTO substrates were first dipped at a speed of 260 mm/min (Dip Coater 1000, G & R Equipment, LLC) into a solution of CZTS nanoparticles suspended in a mixture of hexanes and toluene. The substrate was immersed for 2 sec and then removed at a rate of 450 mm/min and allowed to dry for 2 sec followed by damping onto a drying cloth. The dry substrate was then dipped into a 0.01 M solution of ethylenediamine (EDA) in acetonitrile, soaked for 2 sec and then dried for 2 sec before damping with a drying cloth. This process was repeated until the desired thickness was achieved, as determined by UV-VIS and SEM.

To further increase the conductivity of the films, some were also annealed to remove the organic ligands and sinter the particle together. The films were loaded into a quartz tube with the presence of additional CZTS nanocrystal powder and placed in a horizontal tube furnace. The tube was pumped and purged 3x with Ar and then the pressure was raised to 1000 Torr where it remained for the entire annealing process. The temperature was ramped to 350 °C at a rate of 10 °C/min. It was held at 350 °C for 1.5 hrs before self-cooling to room temperature.

**Materials Characterization.** Low-magnification TEM images were obtained on a JEOL JEM 2000 at a working voltage of 160 kV. TEM samples were prepared by dip-casting CZTS nanocrystals dispersed in hexanes onto carbon-coated copper TEM grids (200 mesh, Structure Probe, Inc.). SEM imaging was performed using a JEOL JSM 6500F FE-SEM and a JEOL JSM 7000F FE-SEM that was equipped with EDAX Genesis energy dispersive spectroscopy detector. Images were acquired under a working voltage of 15 kV and working distance of 10 mm. XRD was performed on a Scintag X-2 Advanced Diffraction System equipped with Cu K $\alpha$  radiation ( $\lambda=1.54 \text{ \AA}$ ) using a dried powder sample of the CZTS nanocrystals. UV-vis spectra were collected for CZTS thin films using a dual beam Cary 500 UV-VIS-NIR spectrophotometer, with an FTO-coated glass substrate as the reference/blank. The thin films were prepared by dip-casting onto FTO-coated glass substrates. Absorption coefficients,  $\alpha$ , were calculated by  $\text{Abs}/l$ , where  $l$  is the film thickness determined by SEM. Photoelectrochemical measurements were carried out in a 3-arm van Dyne electrochemical cell with a Ag/AgCl reference electrode and a platinum basket auxiliary electrode, using a CH Instruments potentiostat. The electrolyte was a 0.1 M KCl/0.1 M Eu(NO<sub>3</sub>)<sub>3</sub> aqueous solution. The photocurrent was measured through an optical window using a 532 nm laser with 17 mW intensity. IPCE data was collected under illumination from filtered (450 nm cutoff filter), collimated light from a 150W Oriel halogen lamp passed through a grating monochromator, with an applied bias of -350 mV vs Ag/AgCl and using the same conditions described above.

## **5.6 Acknowledgements**

We thank Dr. John Chandler and Dr. Gary Zito at the Colorado School of Mines (HR-TEM and SEM) for their assistance. Additional TEM imaging was supported in part by the Microscopy Imaging Network core infrastructure grant from Colorado State University. We thank the CSU Clean Energy Supercluster, the Center for Revolutionary Solar Photoconversion (CRSP) and DuPont for funding.

## 5.7 References

- (1) Ginley, D.; Green, M. A.; Collins, R. *MRS Bull.* **2008**, *33*, 355-363.
- (2) Scragg, J. J.; Dale, P. J.; Peter, L. M.; Zoppi, G.; Forbes, I. *Phys. Status Solidi B* **2008**, *245*, 1772-1778.
- (3) Wadia, C.; Alivisatos, A. P.; Kammen, D. M. *Environ. Sci. Technol.* **2009**, *43*, 2072-2077.
- (4) Jimbo, K.; Kimura, R.; Kamimura, T.; Yamada, S.; Maw, W. S.; Araki, H.; Oishi, K.; Katagiri, H. *Thin Solid Films* **2007**, *515*, 5997-5999.
- (5) Katagiri, H. *Thin Solid Films* **2005**, *480-481*, 426-432.
- (6) Katagiri, H.; Saitoh, K.; Washio, T.; Shinohara, H.; Kurumadani, T.; Miyajima, S. *Sol. Energy Mater. Sol. Cells* **2001**, *65*, 141-148.
- (7) Katagiri, H.; Jimbo, K.; Yamada, S.; Kamimura, T.; Maw, W. S.; Fukano, T.; Ito, T.; Motohiro, T. *Appl. Phys. Express* **2008**, *1*, 041201(1-2).
- (8) Tanaka, T.; Nagatomo, T.; Kawasaki, D.; Nishio, M.; Guo, Q.; Wakahara, A.; Yoshida, A.; Ogawa, H. *J. Phys. Chem. Solids* **2005**, *66*, 1978-1981.
- (9) Kamoun, N.; Bouzouita, H.; Rezig, B. *Thin Solid Films* **2007**, *515*, 5949-5952.
- (10) Kumar, Y. B. K.; Babu, G. S.; Bhaskar, P. U.; Raja, V. S. *Sol. Energy Mater. Sol. Cells* **2009**, *93*, 1230-1237.
- (11) Miyamoto, Y.; Tanaka, K.; Oonuki, M.; Moritake, N.; Uchiki, H. *Japanese Journal of Applied Physics* **2008**, *47*, 596-597.
- (12) Tanaka, K.; Moritake, N.; Oonuki, M.; Uchiki, H. *Japanese Journal of Applied Physics* **2008**, *47*, 598-601.
- (13) Tanaka, K.; Moritake, N.; Uchiki, H. *Sol. Energy Mater. Sol. Cells* **2007**, *91*, 1199-1201.
- (14) Tanaka, K.; Oonuki, M.; Moritake, N.; Uchiki, H. *Sol. Energy Mater. Sol. Cells* **2009**, *93*, 583-587.

- (15) Moriya, K.; Watabe, J.; Tanaka, K.; Uchiki, H. *Phys. Status Solidi C* **2006**, *3*, 2848-2852.
- (16) Fischereder, A.; Rath, T.; Haas, W.; Amenitsch, H.; Albering, J.; Meischler, D.; Larissegger, S.; Edler, M.; Saf, R.; Hofer, F.; Trimmel, G. *Chem. Mater.* **2010**, *22*, 3399-3406.
- (17) Scragg, J. J.; Dale, P. J.; Peter, L. M. *Thin Solid Films* **2009**, *517*, 2481-2484.
- (18) Pawar, S. M.; Pawar, B. S.; Moholkar, A. V.; Choi, D. S.; Yun, J. H.; Moon, J. H.; Kolekar, S. S.; Kim, J. H. *Electrochim. Acta* **2010**, *55*, 4057-4061.
- (19) Todorov, T. K.; Reuter, K. B.; Mitzi, D. B. *Adv. Mater.* **2010**, *22*, E156-E159.
- (20) Panthani, M. G.; Akhavan, V.; Goodfellow, B.; Schmidtke, J. P.; Dunn, L.; Dodabalapur, A.; Barbara, P. F.; Korgel, B. A. *J. Am. Chem. Soc.* **2008**, *130*, 16770-16777.
- (21) Basol, B. M.; Kapur, V. K.; Norsworthy, G.; Halani, A.; Leidholm, C. R.; Roe, R. *Electrochem. Solid-State Lett.* **1998**, *1*, 252-254.
- (22) Koo, B.; Patel, R. N.; Korgel, B. A. *J. Am. Chem. Soc.* **2009**, *131*, 3134-3135.
- (23) Koo, B.; Patel, R. N.; Korgel, B. A. *Chem. Mater.* **2009**, *21*, 1962-1966.
- (24) Tang, J.; Hinds, S.; Kelley, S. O.; Sargent, E. H. *Chem. Mater.* **2008**, *20*, 6906-6910.
- (25) Riha, S. C.; Parkinson, B. A.; Prieto, A. L. *J. Am. Chem. Soc.* **2009**, *131*, 12054-12055.
- (26) Guo, Q.; Hillhouse, H. W.; Agrawal, R. *J. Am. Chem. Soc.* **2009**, *131*, 11672-11673.
- (27) Shavel, A.; Arbiol, J.; Cabot, A. *J. Am. Chem. Soc.* **2010**, *132*, 4514-4515.
- (28) Steinhagen, C.; Panthani, M. G.; Akhavan, V.; Goodfellow, B.; Koo, B.; Korgel, B. A. *J. Am. Chem. Soc.* **2009**, *131*, 12554-12555.
- (29) Luther, J. M.; Law, M.; Beard, M. C.; Song, Q.; Reese, M. O.; Ellingson, R. J.; Nozik, A. J. *Nano Lett.* **2008**, *8*, 3488-3492.

- (30) Kameyama, T.; Osaki, T.; Okazaki, K.-i.; Shibayama, T.; Kudo, A.; Kuwabata, S.; Torimoto, T. *J. Mater. Chem.* **2010**, *20*, 5319-5324.
- (31) Peng, X. G.; Manna, L.; Yang, W. D.; Wickham, J.; Scher, E.; Kadavanich, A.; Alivisatos, A. P. *Nature* **2000**, *404*, 59-61.
- (32) Peng, Z. A.; Peng, X. *J. Am. Chem. Soc.* **2002**, *124*, 3343-3353.
- (33) Cushing, B. L.; Kolesnichenko, V. L.; O'Connor, C. J. *Chem. Rev.* **2004**, *104*, 3893-3946.
- (34) Milliron, D. J.; Hughes, S. M.; Cui, Y.; Manna, L.; Li, J.; Wang, L. W.; Alivisatos, A. P. *Nature* **2004**, *430*, 190-195.
- (35) Yin, Y.; Alivisatos, A. P. *Nature* **2004**, *437*, 664-670.
- (36) Liu, Y.; Gibbs, M.; Puthussery, J.; Gaik, S.; Ihly, R.; Hillhouse, H. W.; Law, M. *Nano Lett.* **2010**, *10*, 1960-1969.
- (37) Luther, J. M.; Law, M.; Song, Q.; Perkins, C. L.; Beard, M. C.; Nozik, A. J. *ACS Nano* **2008**, *2*, 271-280.
- (38) Law, M.; Luther, J. M.; Song, Q.; Hughes, B. K.; Perkins, C. L.; Nozik, A. J. *J. Am. Chem. Soc.* **2008**, *130*, 5974-5985.
- (39) Smith, B. *Infrared Spectral Interpretation: A Systematic Approach*; CRC Press: Boca Raton, Fla, 1999.
- (40) Ryan, M. A.; Turner, J. A.; Williamson, D.; Peterson, M. W.; Frye, J. S.; Maciel, G. E.; Parkinson, B. A. *J. Mater. Res.* **1987**, *2*, 528-537.
- (41) Scragg, J. J.; Berg, D. M.; Dale, P. J. *J. Electroanal. Chem.* **2010**, *646*, 52-59.
- (42) Peter, L. M. *Chem. Rev.* **1990**, *90*, 753-769.
- (43) Films of each thickness were prepared and tested in triplicate from three different reaction batches of both stoichiometric and Zn-rich compositions. All sets showed similar trends between front and back illumination, in addition to the maximum current for films around 300 nm. However, the magnitude of the IPCE values or photocurrent was not consistent, therefore we did not show error bars in our figures.

Supporting Information for:

**Photoelectrochemical Characterization of Nanocrystalline Thin Film  $\text{Cu}_2\text{ZnSnS}_4$**

**Photocathodes**

*Shannon C. Riha, Sarah J. Fredrick, Justin B. Sambur, Yuejiao Liu, Amy L. Prieto, and*

*Bruce A. Parkinson*

**Table S5.1.** The molar ratios of reaction precursors used in the synthesis of stoichiometric and Cu-poor/Zn-rich CZTS nanoparticles.

Reaction	Cu(acac) <sub>2</sub>	Zn(OAc) <sub>2</sub>	Sn(OAc) <sub>4</sub>	S powder
Stoichiometric	0.5 mmol	0.25 mmol	0.25 mmol	1 mmol
Cu-poor/Zn-rich	0.4675 mmol	0.2875 mmol	0.25 mmol	1 mmol

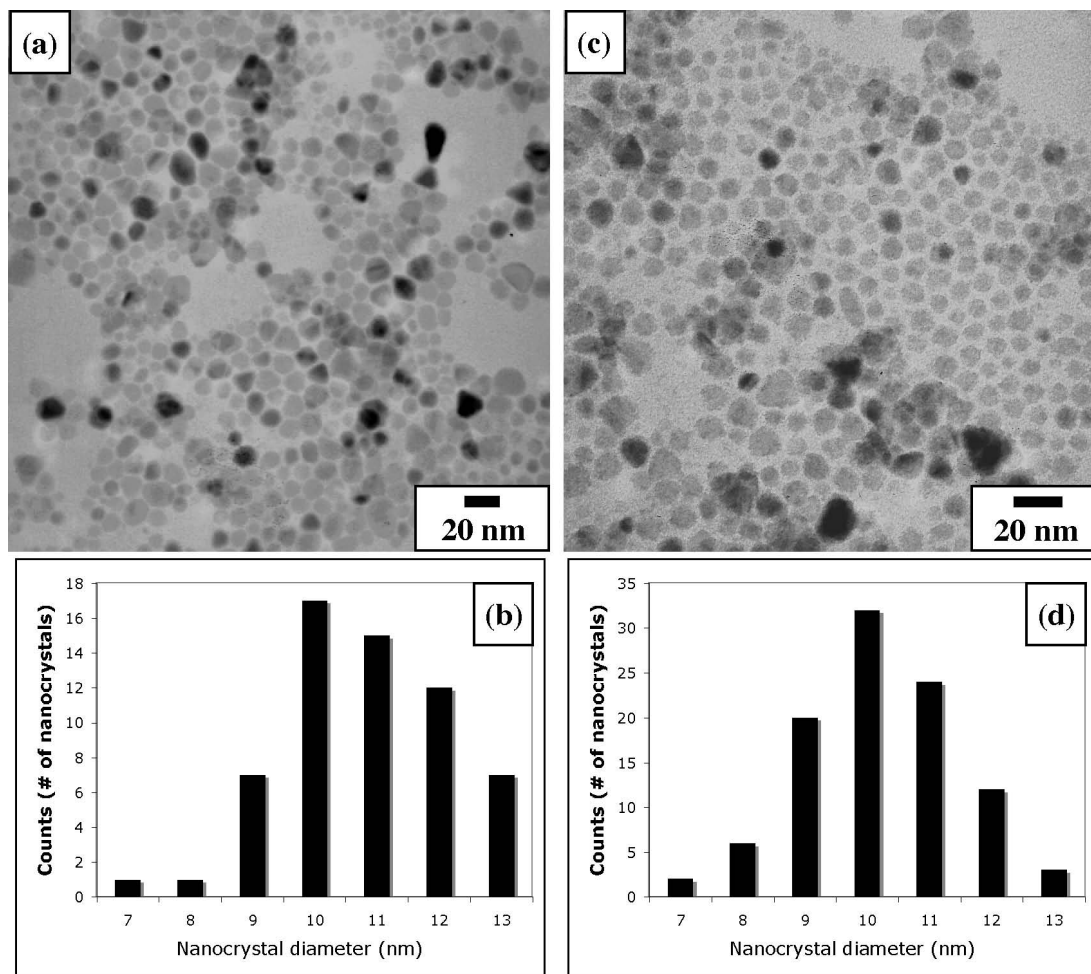


**Figure S5.1.** Low-magnification TEM of the different CZTS reactions and their corresponding size analysis. (a) Stoichiometric CZTS shows an average size of  $10.3 \pm 1.3$  nm (b), and (c) Zn-rich CZTS shows a similar size of  $9.7 \pm 1.3$  nm (d).

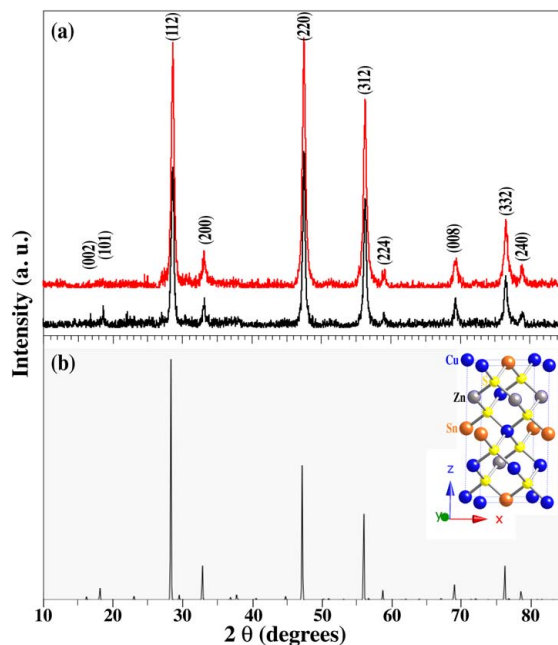


**Figure S5.2.** XRD patterns taken on CZTS nanocrystal powders from stoichiometric and Zn-rich reactions. (a) The diffraction patterns from stoichiometric (black trace) and Zn-rich compositions (red trace) were indexed to tetragonal CZTS (JCPDS 26-0575). W-H method gave an average crystallite size of 15.1 nm, consistent with TEM size analysis. (b) Simulated XRD pattern from the CZTS chalcopyrite crystal structure shown in the inset.

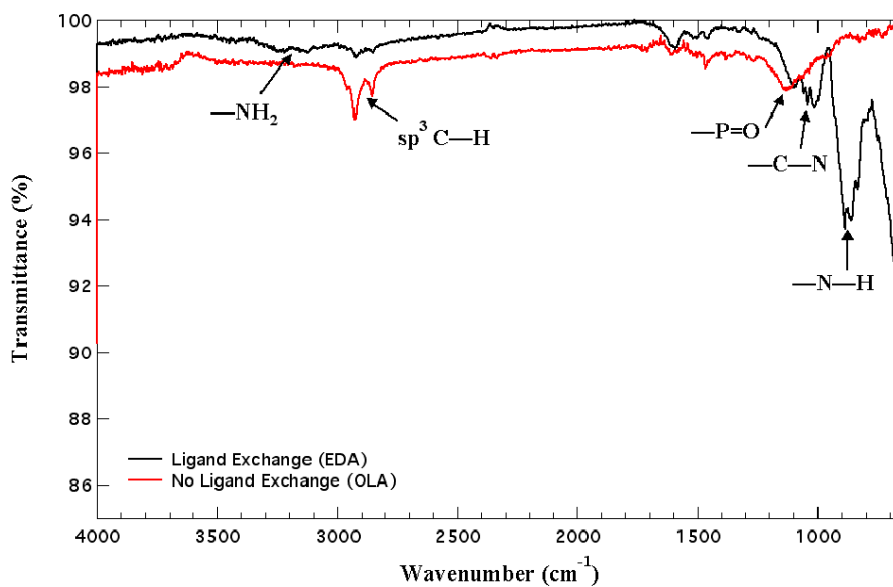


**Figure S5.3.** ATR-IR of CZTS films with (red) and without (black) ligand exchange.

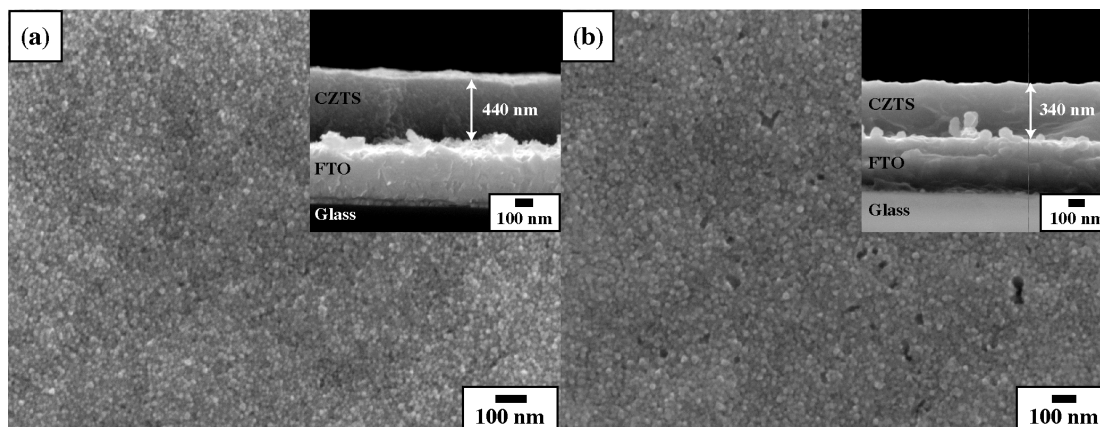


**Figure S5.4.** SEM images before (a) and after (b) annealing at 350 °C. The side profiles, shown in the insets of each figure, illustrate that the film thickness decreases after low-temperature annealing. These results suggest the film becomes thinner as a result of the removal of the organic ligands bringing the nanoparticles closer together.

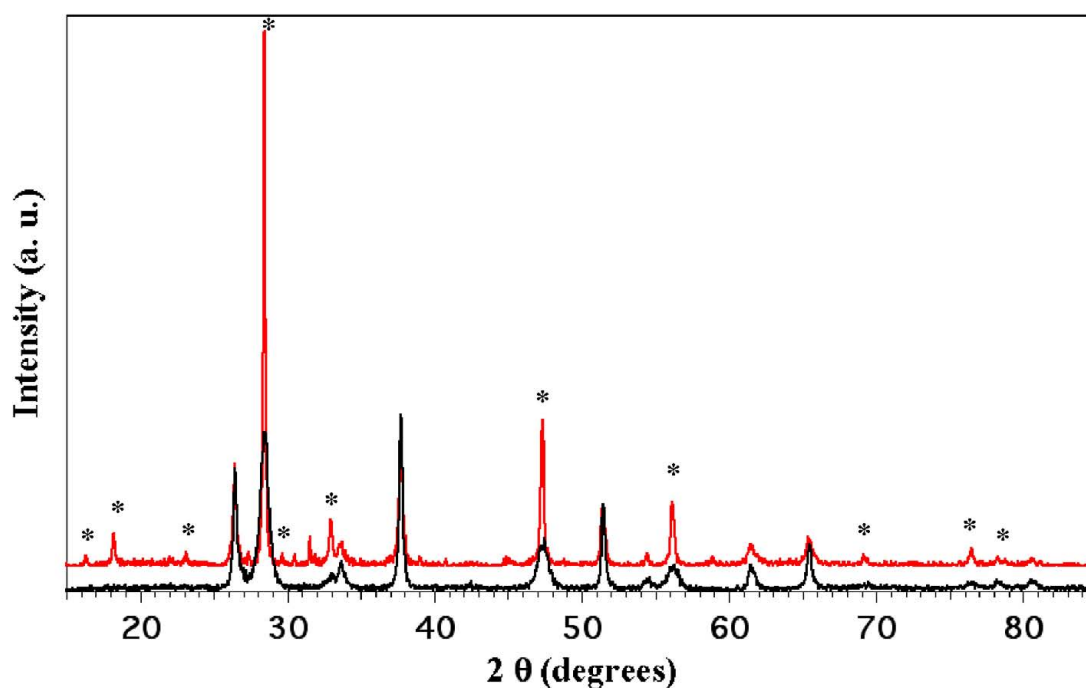


**Figure S5.5.** XRD patterns of CZTS thin films. Scherrer analysis of the as-deposited thin films (black trace) reveals an average particle size of  $12.7 \pm 1.0$  nm, which are similar results to the TEM size analysis. After annealing the film at 350 °C for 1.5 hrs, the diffraction peaks become narrower and more intense (red trace). Scherrer analysis of the annealed film shows an increase in grain size to  $47.8 \pm 11.1$  nm.

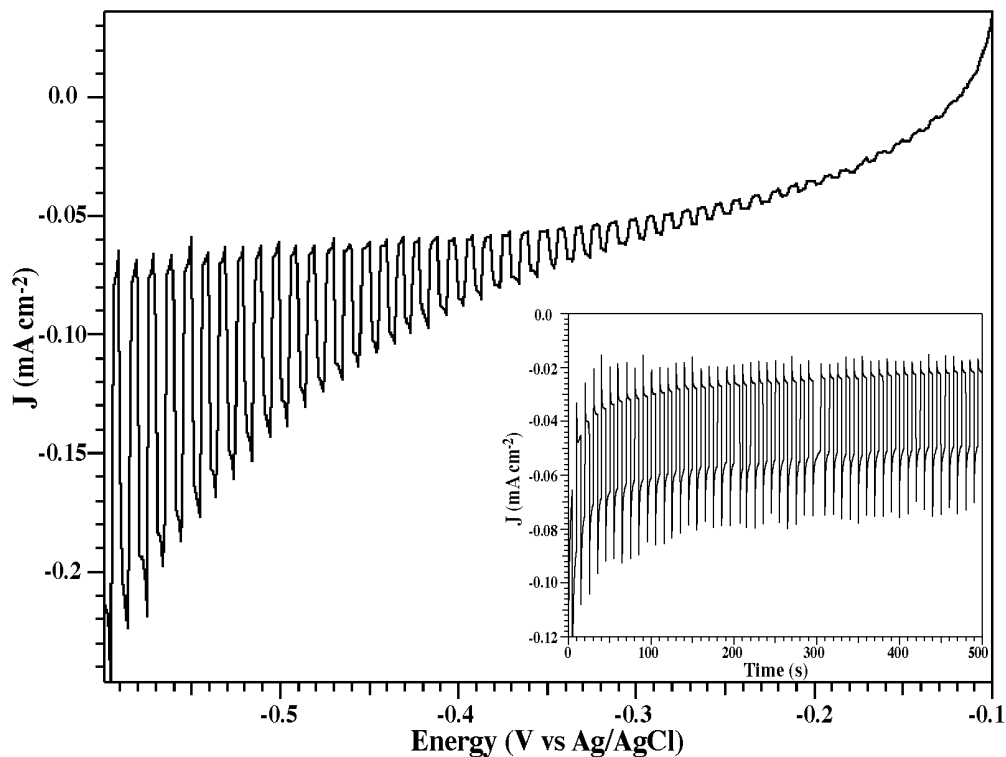


**Figure S5.6.** J-V plots of a 205 nm thick, stoichiometric as-deposited CZTS nanocrystalline thin film. These measurements were taken using 0.05 M cobaltacene redox mediator in acetonitrile with a Ag wire pseudo-reference electrode. The illumination source was a 17 mW, 532 nm laser. These results indicate a substantial decrease in photocurrent density in comparison to the as-deposited films when using the Eu(III) mediator. The inset shows the photostability measurements at -500 mV vs Ag wire under the same illumination source.

## CHAPTER 6

### COMPOSITIONALLY TUNABLE $\text{Cu}_2\text{ZnSn}(\text{S}_{1-x}\text{Se}_x)_4$ NANOCRYSTALS: PROBING THE EFFECT OF SE-INCLUSION IN MIXED CHALCOGENIDE THIN FILMS

The contents in this dissertation chapter include a communication to be submitted to *The Journal of the American Chemical Society*. This chapter presents the first solution-based synthetic routes to compositionally controlled  $\text{Cu}_2\text{ZnSn}(\text{S}_{1-x}\text{Se}_x)_4$  nanocrystal solid-solutions. The synthesis of this mixed chalcogenide provides a direct route to determine the effect of Se inclusion in  $\text{Cu}_2\text{ZnSnS}_4$  nanocrystal thin films.

The synthetic method was developed by Shannon C. Riha, who also prepared the manuscript with helpful insights, discussions, and editing by Prof. Bruce A. Parkinson and Prof. Amy L. Prieto.

## 6.1 Overview

Nanocrystals of multicomponent chalcogenides, such as  $\text{Cu}_2\text{ZnSnS}_4$  (CZTS), are potential building blocks for low-cost thin film photovoltaics. CZTS PV devices with modest efficiencies have been realized through post-deposition annealing at high temperatures in Se vapor. However, little is known about the precise role of Se in the CZTS system. We report the direct solution-phase synthesis and characterization of  $\text{Cu}_2\text{ZnSn}(\text{S}_{1-x}\text{Se}_x)_4$  nanocrystals with  $0 \leq x \leq 1$  with an aim of probing the role of Se incorporation into CZTS. Our results indicate that increasing Se incorporation increases the lattice parameters, decreases the band gap of the material and decreases the PV properties while likely increasing the electrical conductivity of the particles.

## 6.2 Communication

Multicomponent chalcogenide nanocrystals (MCNs) are capable of revolutionizing the manufacture of thin film solar cells.<sup>1-7</sup> They offer the advantage of simple, low temperature deposition that can lead to inexpensive large-scale production. Furthermore, MCNs offer the additional advantage of having tunable structural, optical, electronic and defect properties that all can influence photovoltaic (PV) properties.<sup>1,8-10</sup> For example, it is known that in the  $\text{Cu}(\text{In,Ga})\text{Se}_2$  system, optimizing the In:Ga ratio changes the band gap to maximize solar cell efficiencies. Mixed chalcogenides also allow band gap tunability, offering an alternative to the quantum confinement effect, as this effect is generally lost when nanocrystals are annealed into dense films.<sup>2,11</sup>

$\text{Cu}_2\text{ZnSnS}_4$  (CZTS) is receiving increased attention for use in low-cost thin film PVs<sup>3,6,12,13</sup> due to its earth-abundant constituents, optimal band gap and high absorption

coefficient. CZTS crystallizes in the chalcopyrite crystal system with Cu and Zn cations sharing one Wyckoff position.<sup>14,15</sup> Theoretical and experimental work has shown that the electronic properties can be tuned by varying the Cu:Zn ratio as well as their ordering.<sup>12,14-16</sup> In both bulk and nanocrystal thin film PV devices, Cu:(Zn+Sn) = 0.8 and Zn:Sn = 1.2 ratios lead to the highest reported power conversion efficiencies.<sup>3,12,16,17</sup> Furthermore, Chen *et al.* calculated that the band gap of CZTS/Se solid solutions can be controlled by varying the S:Se concentration.<sup>9</sup> They predicted that the band gap linearly decreases with increasing Se content. Herein we report the first direct solution synthesis of  $\text{Cu}_2\text{ZnSn}(\text{S}_{1-x}\text{Se}_x)_4$  nanocrystals with control over x from 0 to 1, where the measured band gaps across the solid solution range are consistent with theoretical predictions.

Despite the similarities between bulk and nanocrystal thin films, PV devices prepared from CZTS nanocrystals without post-deposition annealing at high ( $\geq 500^\circ\text{C}$ ) temperatures are <1% efficient.<sup>6,18</sup> Following the procedures from the CIGS literature, Guo, et al. recently reported that annealing CZTS nanocrystals in the presence of Se vapor at  $500^\circ\text{C}$  resulted in a PV device with 7.2% conversion efficiency.<sup>3</sup> The final composition of the annealed films is not well controlled because high-temperature annealing steps provide little control over the S to Se ratio. The large efficiency increase is surprising if the incorporation of Se simply tunes the band gap. Two hypotheses in the literature suggest that the inclusion of Se i) creates  $\text{Cu}_2\text{ZnSn}(\text{S}_{1-x}\text{Se}_x)_4$  alloys which alter the optical and electronic properties of the films, or ii) facilitates enhanced grain growth.<sup>2</sup> A third possible, but related hypothesis is that the grain boundaries are passivated by Se-rich surfaces due to a lower band gap surface layer removing potential barriers for grain to grain carrier transport. A first step in testing these hypotheses is the development of a

robust synthesis for phase pure, compositionally controlled  $\text{Cu}_2\text{ZnSn}(\text{S}_{1-x}\text{Se}_x)_4$  (CZTS,Se) nanocrystals.

The synthesis of CZTS,Se nanocrystals was carried out using a hot injection method adapted from a previous report.<sup>13</sup> Briefly, copper(II) acetylacetonate, zinc acetate, and tin(IV) acetate were combined in appropriate ratios ( $\text{Cu}:(\text{Zn}+\text{Sn}) = 0.8$  and  $\text{Zn}:\text{Sn} = 1.2$ ) under inert conditions with oleylamine (OLA). The flask was heated under vacuum to 150 °C and then reduced to 125 °C after 5 minutes, where it was held until injection. Meanwhile, elemental S and Se were mixed with oleylamine and sodium borohydride ( $\text{NaBH}_4$ ) via sonication. Trioctylphosphine oxide (TOPO) was heated in a separate flask to 325 °C, at which point both the metal and chalcogenide precursors were simultaneously injected. The growth temperature was then reduced to 285 °C and the reaction was quenched after 5 minutes. Full experimental details can be found in the supporting information.

Control of the stoichiometry of MCNs is challenging, especially when five elements are involved in the reaction; therefore balancing the relative precursor reactivities is key to producing the desired composition without unwanted side products.<sup>9,10</sup> Compositionally controlled CZTS,Se nanocrystals were only obtained when elemental S and Se were sonicated together with  $\text{NaBH}_4$  and OLA, to balance the reactivities of S and Se were balanced. Recently it was reported that  $\text{NaBH}_4$ , in the presence of hydrophobic alkylamines (i.e., OLA), would reduce Se powder to form alkylammonium selenide complexes.<sup>19</sup> We explored keeping the OLA-Se and OLA-S precursors separate versus mixing them in one vial, prior to injection. Keeping the S and Se precursors separate often resulted in a Se-rich composition or in a phase separation of CZTS and CZTSe

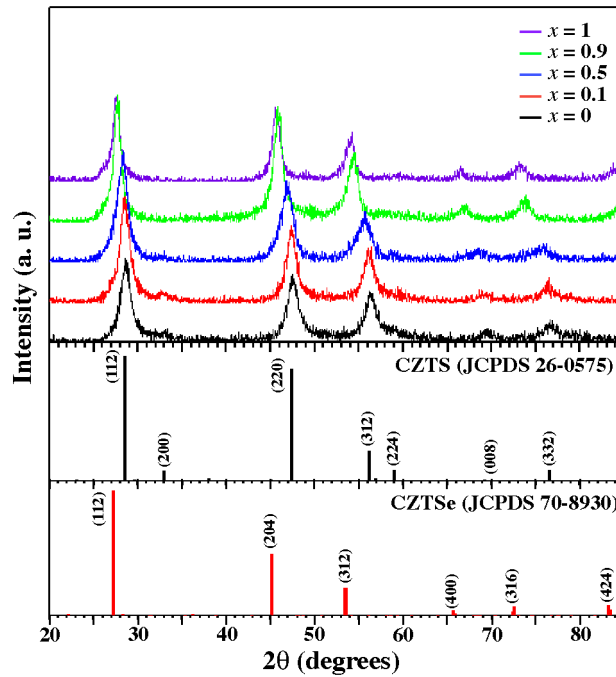
**Table 6.1.** Compositional Analysis, Lattice Parameters ( $a$  and  $c$ ), and Band Gap Energies of  $\text{Cu}_2\text{ZnSn}(\text{S}_{1-x}\text{Se}_x)_4$  Nanocrystals.

Theoretical Composition	Precursor	Composition determined by	$a$ (Å)	$c$ (Å)	$E_g$ (eV)
	Ratios Cu:Zn:Sn:S:Se	EDS Cu:Zn:Sn:S:Se			
$\text{Cu}_2\text{ZnSnS}_4$ ( $x = 0$ )	1.8:1.2:1:7:0	1.9(2):1.1(3):1.0(1):4.1(4)	5.41	10.81	1.54(1)
$\text{Cu}_2\text{ZnSn}(\text{S}_{0.9}\text{Se}_{0.1})_4$ ( $x = 0.1$ )	1.8:1.2:1:6.3:0.7	2.0(2):1.1(3):1.0(1):3.5(2):0.4(1)	5.44	10.89	1.52(2)
$\text{Cu}_2\text{ZnSn}(\text{S}_{0.5}\text{Se}_{0.5})_4$ ( $x = 0.5$ )	1.8:1.2:1:3.5:3.5	2.0(2):1.1(1):1.0(1):2.1(2):1.8(2)	5.48	10.95	1.50(2)
$\text{Cu}_2\text{ZnSn}(\text{S}_{0.1}\text{Se}_{0.9})_4$ ( $x = 0.9$ )	1.8:1.2:1:0.7:6.3	1.8(2):1.2(2):1.0(1):0.3(1):3.7(1)	5.60	11.17	1.48(1)
$\text{Cu}_2\text{ZnSnSe}_4$ ( $x = 1$ )	1.8:1.2:1:0:7	1.9(2):1.1(1):1.0(1):4.0(2)	5.61	11.28	1.47(2)

nanocrystals. We speculate that this could be due to variations in the relative chalcogenide speciation, and thus reactivity, at the time of nucleation. Nucleation occurs immediately upon injection; therefore, if the OLA-Se/OLA-S mixture contains multiple species, preferential incorporation of Se or distinct phase nucleation could give the observed results. Hence, a homogeneous mixture of OLA-S and OLA-Se was required to prepare compositionally controlled CZTS,Se nanocrystals. Once the reactivities of S and Se were controlled, the metal to chalcogen ratios and temperature were optimized to prepare the desired S:Se ratios and inhibit the formation of unwanted side products.

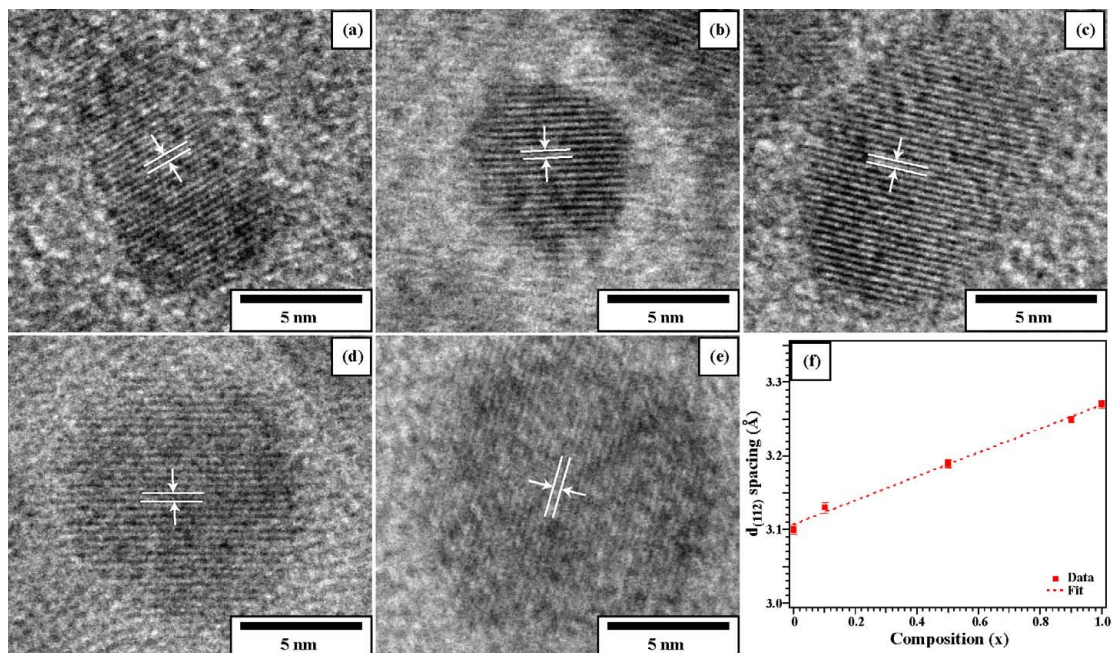
The compositions of the CZTS,Se nanocrystals were determined using energy dispersive x-ray spectroscopy (EDS) and are listed in Table 6.1. The relationship between the S and Se precursor ratios and the obtained S to Se ratios in the final CZTS,Se nanocrystals are in close agreement, illustrating that the reactivities of the chalcogen precursors were balanced.

Figure 6.1 shows the powder x-ray diffraction (XRD) data of CZTS,Se nanocrystals synthesized with S:Se ratios from 0 to 1. The nanocrystal sizes for each composition were determined by the Williamson-Hall method and are found in the Supporting Information (Table S6.1). The XRD data indicates the incorporation of Se in the CZTS



**Figure 6.1.** XRD patterns of  $\text{Cu}_2\text{ZnSn}(\text{S}_{1-x}\text{Se}_x)_4$  nanocrystals for various ratios of S to Se. The standard XRD patterns for CZTS and CZTSe are shown below.

nanocrystals. At  $x = 0$ , the diffraction peaks can be indexed to those of kesterite  $\text{Cu}_2\text{ZnSnS}_4$  (JCPDS 26-0575). As the Se content increases, the larger Se atoms ( $1.98 \text{ \AA}$ ) replace the smaller S atoms ( $1.84 \text{ \AA}$ ), resulting in an increase in the lattice parameter as seen in the shift in the diffraction peaks to lower  $2\theta$  angles (Figure S6.1a). Furthermore, at  $x = 0$ , the small peak at  $32.99^\circ 2\theta$  can be indexed to the (200) plane of CZTS. As the ratio of S:Se decreases, this peak intensity decreases and disappears at values of  $x \geq 0.9$ . Similarly the diffraction peak around  $2\theta = 83.18^\circ$ , corresponding to the (424) plane of CZTSe, appears at values of  $x \geq 0.9$ . At  $x = 1$ , the diffraction pattern corresponds to  $\text{Cu}_2\text{ZnSnSe}_4$  (JCPDS 70-8930). The  $\text{Cu}_2\text{ZnSn}(\text{S}_{1-x}\text{Se}_x)_4$  lattice parameters ( $a$  and  $c$  listed in Table 6.1) were calculated as a function of  $x$  from the XRD data and varied linearly with Se content, as expected by Vegard's Law (Figures S6.1b and S6.1c).



**Figure 6.2.** HR-TEM images of the  $d_{(112)}$  lattice fringes for  $\text{Cu}_2\text{ZnSn}(\text{S}_{1-x}\text{Se}_x)_4$  nanocrystals with (a)  $x = 0$ , (b)  $x = 0.1$ , (c)  $x = 0.5$ , (d)  $x = 0.9$ , (e)  $x = 1$ . The lattice spacing is plotted as a function of  $x$  in panel (f) and follows Vegard's Law.

Figures 6.2a-e display HR-TEM images highlighting the lattice fringes of individual  $\text{Cu}_2\text{ZnSn}(\text{S}_{1-x}\text{Se}_x)_4$  nanocrystals representative of each composition. Lattice spacings were calculated by averaging measurements from multiple fringes on each particle, as well as multiple particles. At  $x = 0$ , the measured lattice spacing is  $3.10 \pm 0.04 \text{ \AA}$  corresponding to the  $\text{Cu}_2\text{ZnSnS}_4$  (112) crystal plane. As the value of  $x$  increases from 0 to 1, the lattice spacing increases. When  $x = 1$ , the measured  $d_{(112)}$  spacing is  $3.27 \pm 0.04 \text{ \AA}$ . Again Vegard's Law is obeyed when plotting the  $d_{(112)}$  spacing as a function of a change in the value of  $x$  (Figure 6.2f). TEM images of the CZTS,Se nanocrystals with  $x$  ranging from 0 to 1 (Figure S6.2) showed average particle size ranging from 7.8 nm when  $x = 0$  to 11.0 nm when  $x = 1$ , and are consistent with those calculated from line broadening of the diffraction peaks (a statistical analysis of the particle sizes can be found in Table S6.1).

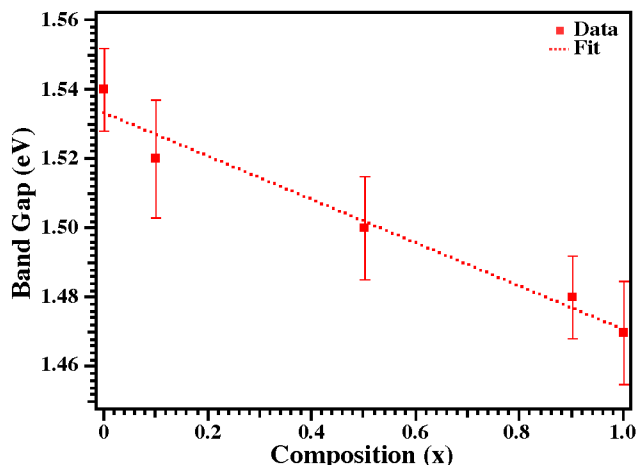


**Figure 6.3.** Band gap energies determined from the optical absorption of  $\text{Cu}_2\text{ZnSn}(\text{S}_{1-x}\text{Se}_x)_4$  colloidal nanocrystals. A linear decrease was observed with an increase in Se content.

As mentioned above, one way to tune the band gap of a semiconducting material is by quantum confinement. A more robust way, especially if the nanocrystals are to be annealed into a thin film, is to tune the band gap by changing the composition of MCNs. Figure S6.3a shows the UV-vis data from solutions of CZTS,Se nanocrystals from each composition. The band gap energies were calculated by plotting the square of  $\alpha hv$ —where  $\alpha$  is the absorption coefficient obtained from UV-vis spectra of solutions of CZTS,Se nanocrystals (Figure S4.3a) and  $hv$  is the photon energy—as a function of  $hv$ , and extrapolating the linear portion to the x-intercept (Figure S6.3b). Figure 3 plots the band gaps as a function of composition. The band gap energies determined from the optical absorption of the CZTS,Se colloidal nanocrystal (listed in Table 6.1) range from 1.54 eV for  $x = 0$  to 1.47 eV for  $x = 1$ , which are comparable to experimental bulk values reported for CZTS and CZTSe, respectively.<sup>5,9,13</sup> Increasing the Se concentration reduces the band gap energy, emphasizing the ability to change the band gap with composition. Although most binary semiconducting alloys demonstrate a non-linear “bowing” effect of their band gaps with composition,<sup>1,9,10</sup> the errors in our measurements and the small

change in the gap across the composition range does not allow the determination of a bowing parameter.

The synthesis of pure  $\text{Cu}_2\text{ZnSn}(\text{S}_{1-x}\text{Se}_x)_4$  MCNs with varying S:Se ratios is a direct route to testing the two hypotheses regarding annealing CZTS nanocrystals in Se vapor.<sup>3,16</sup> Preliminary results discussed herein suggest that the second hypothesis may help to explain the role of Se in CZTS nanocrystal thin films. In  $\text{Cu}(\text{In}_{1-x}\text{Ga}_x)\text{S}_2$ -based solar cells, thermodynamic calculations indicate that the S atoms will be replaced by Se when the films are annealed at high temperatures with an elevated partial pressure of Se.<sup>2</sup> The replacement of the S atoms by the larger Se atoms increases the crystal lattice parameters causing the films to expand leading to improved grain growth. Additionally, when Guo, *et al.* annealed their CIGS nanocrystal thin films in a S-only vapor they did not observe grain growth, further suggesting that Se is responsible for forming densely packed grains in that material.<sup>2</sup> The inclusion of Se in our CZTS nanocrystals also increases the lattice parameters as determined by XRD.

However, it is likely that in this system Se is a better transport agent than S with a more dramatic effect on grain growth than simply an increase in lattice parameters. To provide additional evidence supporting this hypothesis, the CZTS,Se thin films made from the syntheses reported in this manuscript were annealed, but at a much lower temperature (350 °C) compared to that reported by Guo and Todorov.<sup>3,16</sup> We observed a dramatic difference because pure CZTS nanocrystal films did not transport during annealing, whereas with some Se-rich CZTS,Se films, material was transported off the substrates into the quartz tube. Although the band gap, and hence theoretical efficiency, of Se-rich CZTS,Se films should decrease, the results from Guo indicate that the grain

boundaries that are present in nanocrystal films are the main cause of the observed low efficiencies for these films without annealing. Annealing in Se vapor at high temperatures results in fewer grain boundaries of relatively higher electrical conductivity (CZTSe nanocrystal powders show higher conductivity relative to pure CZTS nanocrystal powders, Figure S6.4), leading to higher efficiency. Current studies are underway to elucidate the structural changes occurring when annealing CZTS nanocrystals in a Se atmosphere to mimic this behavior in solution, as well as determining the PV performance of such materials as a function of Se concentration.

We have shown that MCNs of  $\text{Cu}_2\text{ZnSn}(\text{S}_{1-x}\text{Se}_x)_4$  can be successfully synthesized by the hot-injection method through careful tuning of the S and Se precursor reactivities. The composition-dependence of the lattice parameters followed Vegard's law. Varying the value of  $x$  from 0 to 1 resulted in a tunable band gap of 1.54 eV to 1.47 eV for  $x = 0$  and 1, respectively. The synthesis of pure  $\text{Cu}_2\text{ZnSn}(\text{S}_{1-x}\text{Se}_x)_4$  nanocrystals reported herein now provides an avenue for probing the effect of Se-inclusion in mixed chalcogenide thin films.

### 6.3 Experimental Details

***CZTS,Se Nanocrystal Synthesis.*** Copper(II) acetylacetonate ( $\text{Cu}(\text{acac})_2$ , Aldrich, 99.99%), tin(IV) acetate ( $\text{Sn}(\text{OAc})_4$ , Aldrich), zinc acetate ( $\text{Zn}(\text{OAc})_2$ , Fisher), sulfur powder (S, Aldrich), selenium powder (Se, Strem, 99.99%) trioctylphosphine oxide (TOPO, Aldrich, 99%), and sodium borohydride ( $\text{NaBH}_4$ , Alfa 98%) were purchased and used as received. Oleylamine (OLA, Acros, 80-90%) was degassed for 1 h with Ar before bringing it into the glove box. All reaction conditions were kept inert to prevent the

formation of an oxide. The target composition, deviated from stoichiometry with  $\text{Cu}:(\text{Zn}+\text{Sn}) = 0.8$  and  $\text{Zn}:\text{Sn} = 1.2$  which is based on the highest solar cell efficiencies.<sup>3,16,17</sup> The ratio of S to Se varied from 0 to 1 and the precursor ratios can be found in Table 6.1. In a typical synthesis, 0.3506 mmol  $\text{Cu}(\text{acac})_2$ , 0.2156 mmol  $\text{Zn}(\text{OAc})_2$ , 0.1875 mmol  $\text{Sn}(\text{OAc})_4$ , and 3 mL OLA were prepared in a 25 mL 3-neck round-bottom reaction flask and heated under vacuum to 150 °C. After 5 minutes the temperature was lowered to 125 °C and the mixture remained at this temperature under vacuum until injection. In a 20 mL scintillation vial, a total of 1.32 mmol elemental S and Se powders, 0.8 mmol  $\text{NaBH}_4$  and 3 mL OLA were sonicated until both the S and Se had dissolved—typically 45 min. In a 50 mL 3-neck round-bottom reaction flask, 10 mmol TOPO was heated to 325 °C on an Ar Schlenk line. When the temperature reached 100 °C, the flask was pumped and purged 3x, and then left under Ar for the remainder of the reaction. At 325 °C, the S/Se and metal precursors were rapidly injected via two 5 mL Luer-Lock syringes, simultaneously. The growth temperature was reduced to 285 °C and the reaction was quenched after 5 minutes by extracting the product solution from the reaction flask and adding minimal amounts of hexanes to prevent it from solidifying when cooled to room temperature. Methanol was added to the product, which was subsequently centrifuged to precipitate the particles from solution. The CZTS,Se nanocrystals were washed 3x with hexanes and methanol, and then resuspended in a 6:1 hexanes/toluene mix.

**Materials Characterization.** TEM samples were prepared by dipping carbon-coated nickel TEM grids (200 mesh, Electron Microscopy Sciences) into dilute solutions of CZTS,Se nanocrystals dispersed in hexanes/toluene. Low-magnification TEM images

were obtained on a JEOL 1400 at a working voltage of 100 kV. HR-TEM images were taken using a Phillips CM200 STEM under a working voltage of 200 kV. The TEM is equipped with a Princeton Gamma Tech Prism 2000 EDS detector, used for elemental analysis of the CZTS nanocrystals. SEM imaging was performed using a JEOL JSM 6500F FE-SEM that was equipped with EDAX Genesis energy dispersive spectroscopy detector. Images were acquired under a working voltage of 15 kV and working distance of 10 mm. XRD was performed on a Scintag X-2 Advanced Diffraction System equipped with Cu K $\alpha$  radiation ( $\lambda=1.54 \text{ \AA}$ ) using a dried powder sample of the CZTS,Se nanocrystals. UV-vis spectra was collected for Cu<sub>2</sub>ZnSn(S<sub>1-x</sub>Se<sub>x</sub>)<sub>4</sub> colloidal nanocrystals using an Agilent 8453 UV-Visible ChemStation Spectrophotometer. Conductivity measurements were conducted using a device, such that the nanocrystalline powder was pressed into a pellet between two copper plugs. The diameter of the pellet was 3 mm and the thickness was 1 mm. Linear sweep voltammetry was used to determine current-voltage behavior with a scan rate of 50 mV s<sup>-1</sup>.

#### **6.4 Acknowledgements**

We thank Dr. Gary Zito and Dr. John Chandler at the Colorado School of Mines for their assistance with HR-TEM. Additional TEM imaging was supported in part by the Microscope Imaging Network core infrastructure grant from Colorado State University. This study was funded by the Center for Revolutionary Solar Photoconversion (CRSP) and CSU Clean Energy Supercluster.

## 6.5 References

- (1) Chen, L.-J.; Liao, J.-D.; Chuang, Y.-J.; Fu, Y.-S. *J. Am. Chem. Soc.* **2011**, *133*, 3704-3707.
- (2) Guo, Q.; Ford, G. M.; Hillhouse, H. W.; Agrawal, R. *Nano Lett.* **2009**, *9*, 3060-3065.
- (3) Guo, Q.; Ford, G. M.; Yang, W.-C.; Walker, B. C.; Stach, E. A.; Hillhouse, H. W.; Agrawal, R. *J. Am. Chem. Soc.* **2010**, *132*, 17384-17386.
- (4) Panthani, M. G.; Akhavan, V.; Goodfellow, B.; Schmidtke, J. P.; Dunn, L.; Dodabalapur, A.; Barbara, P. F.; Korgel, B. A. *J. Am. Chem. Soc.* **2008**, *130*, 16770-16777.
- (5) Shavel, A.; Arbiol, J.; Cabot, A. *J. Am. Chem. Soc.* **2010**, *132*, 4514-4515.
- (6) Steinhagen, C.; Panthani, M. G.; Akhavan, V.; Goodfellow, B.; Koo, B.; Korgel, B. A. *J. Am. Chem. Soc.* **2009**, *131*, 12554-12555.
- (7) Talapin, D. V.; Lee, J.-S.; Kovalenko, M. V.; Shevchenko, E. V. *Chem. Rev.* **2010**, *110*, 389-458.
- (8) Smith, D. K.; Luther, J. M.; Semonin, O. E.; Nozik, A. J.; Beard, M. C. *ACS Nano* **2011**, *5*, 183-190.
- (9) Chen, S.; Walsh, A.; Yang, J.-H.; Gong, X. G.; Sun, L.; Yang, P.-X.; Chu, J.-H.; Wei, S.-H. *Phys. Rev. B* **2011**, *83*, 125201.
- (10) Chiang, M.-Y.; Chang, S.-H.; Chen, C.-Y.; Yuan, F.-W.; Tuan, H.-Y. *J. Phys. Chem. C* **2011**, *115*, 1592-1599.
- (11) Regulacio, M. D.; Han, M.-Y. *Acc. Chem. Res.* **2010**, *43*, 621-630.
- (12) Riha, S. C.; Fredrick, S. J.; Sambur, J. B.; Liu, Y.; Prieto, A. L.; Parkinson, B. A. *ACS Appl. Mater. Interfaces* **2010**, *3*, 58-66.
- (13) Riha, S. C.; Parkinson, B. A.; Prieto, A. L. *J. Am. Chem. Soc.* **2009**, *131*, 12054-12055.
- (14) Persson, C. *J. Appl. Phys.* **2010**, *107*, 053710.

- (15) Schorr, S.; Gonzalez-Aviles, G. *physica status solidi (a)* **2009**, *206*, 1054-1058.
- (16) Todorov, T. K.; Reuter, K. B.; Mitzi, D. B. *Adv. Mater.* **2010**, *22*, E156-E159.
- (17) Katagiri, H.; Jimbo, K.; Yamada, S.; Kamimura, T.; Maw, W. S.; Fukano, T.; Ito, T.; Motohiro, T. *Appl. Phys. Express* **2008**, *1*, 041201(1-2).
- (18) Guo, Q.; Hillhouse, H. W.; Agrawal, R. *J. Am. Chem. Soc.* **2009**, *131*, 11672-11673.
- (19) Wei, Y.; Yang, J.; Lin, A. W. H.; Ying, J. Y. *Chem. Mater.*, *22*, 5672-5677.

Supporting Information for:

**Compositionally Tunable  $\text{Cu}_2\text{ZnSn}(\text{S}_{1-x}\text{Se}_x)_4$  Nanocrystals: Probing the Effect of Se-  
Inclusion in Mixed Chalcogenide Thin Films**

*Shannon C. Riha, Bruce A. Parkinson, and Amy L. Prieto*

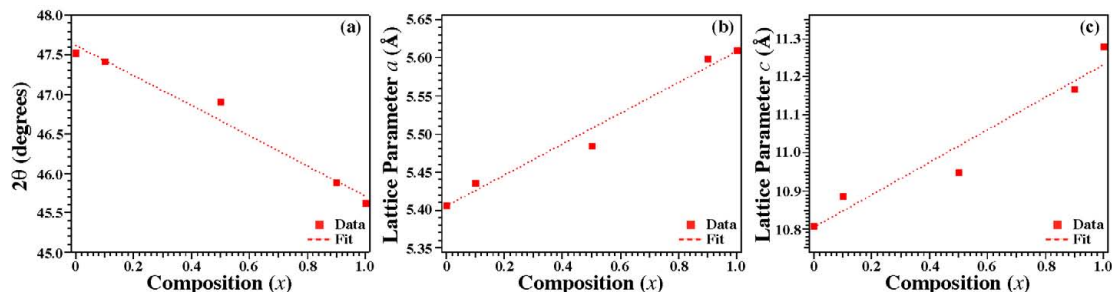


**Figure S6.1.** (a) The relationship between the (220/204) diffraction peak and the  $\text{Cu}_2\text{ZnSn}(\text{S}_{1-x}\text{Se}_x)_4$  composition as a function of  $x$ . As the Se content increases, the (220/204) peak exhibit a linear shift to lower  $2\theta$ . Lattice parameter  $a$  (b) and lattice parameter  $c$  (c) were determined from the XRD patterns and are plotted as a function of  $x$ . Both lattice parameters show a linear increase with increasing Se content. This data is consistent with Vegard's Law.

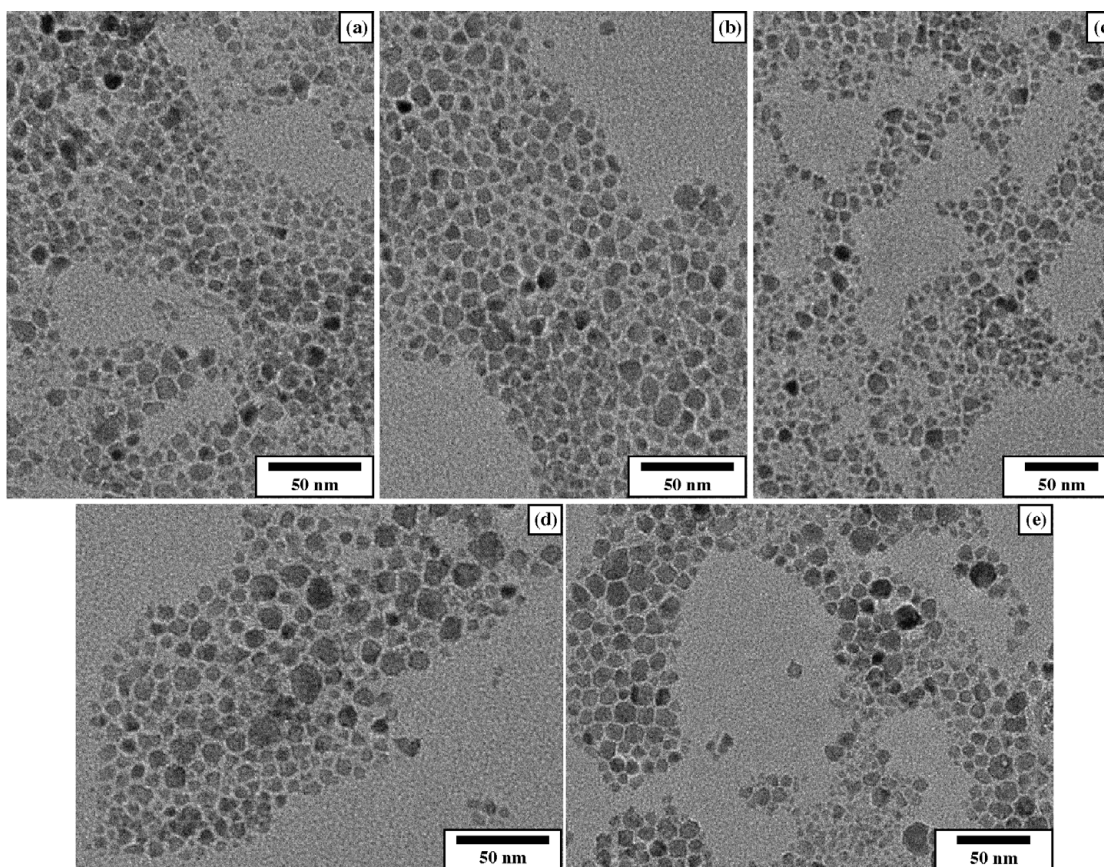


**Figure S6.2.** TEM images of  $\text{Cu}_2\text{ZnSn}(\text{S}_{1-x}\text{Se}_x)_4$  nanocrystals with (a)  $x = 0$ , (b)  $x = 0.1$ , (c)  $x = 0.5$ , (d),  $x = 0.9$ , and (e)  $x = 1$ . The average nanocrystal sizes range from 7.8 nm for  $x = 0$  to 11.0 nm for  $x = 1$ , and are consistent with those calculated from XRD data using the Williamson Hall method.

**Table S6.1.** Nanocrystal size distribution determined from XRD and TEM analysis.

Theoretical Composition	Nanocrystal Size from XRD (nm)	Nanocrystal Size from TEM (nm)
$\text{Cu}_2\text{ZnSnS}_4$ ( $x = 0$ )	$7.5 \pm 0.6$	$7.8 \pm 1.6$
$\text{Cu}_2\text{ZnSn}(\text{S}_{0.9}\text{Se}_{0.1})_4$ ( $x = 0.1$ )	$9.4 \pm 1.2$	$8.0 \pm 1.9$
$\text{Cu}_2\text{ZnSn}(\text{S}_{0.5}\text{Se}_{0.5})_4$ ( $x = 0.5$ )	$6.6 \pm 0.3$	$9.3 \pm 1.8$
$\text{Cu}_2\text{ZnSn}(\text{S}_{0.1}\text{Se}_{0.9})_4$ ( $x = 0.9$ )	$10.2 \pm 0.7$	$8.4 \pm 1.7$
$\text{Cu}_2\text{ZnSnSe}_4$ ( $x = 1$ )	$9.7 \pm 0.7$	$11.0 \pm 2.6$

**TEM Size Analysis.** Figure S6.2 shows low magnification TEM images of the nanocrystals from each  $\text{Cu}_2\text{ZnSn}(\text{S}_{1-x}\text{Se}_x)_4$  composition. The size distribution was determined by averaging the diameter of 100 nanocrystals from each sample over multiple areas on the TEM grid. The nanocrystal sizes range from  $7.8 \pm 1.6$  nm for  $x = 0$  to  $11.0 \pm 2.6$  nm for  $x = 1$ —these measured values along with the calculated values from the XRD data can be found in Table S6.1. It is quite clear that the size distribution varies by about 25% within each sample. Additionally, as the value of  $x$  increases, the particle size also increases.

Various parameters in the synthesis preparation were explored to help control the size distribution, such as surfactant choice, temperature, and growth time. Because selenium does not dissolve in OLA on its own, we used  $\text{NaBH}_4$  to assist in the reduction of Se so that OLA-Se could be formed.  $\text{NaBH}_4$  is a very powerful reducing agent, which is helpful for dissolving the Se, but may also have an effect on the growth of the CZTS,Se nanocrystals. Initially we tried adjusting the injection temperature as this affects the nucleation step in these reactions. At lower injection temperatures ( $\leq 300$  °C), we observed lower chalcogenide inclusion and the presence of binary impurities, while higher injection temperatures ( $\geq 350$  °C) lead to uncontrolled growth. The growth temperature was also varied from 325 °C to 260 °C. At the higher end of the growth temperatures, a very wide size distribution was observed and the nanocrystals did not

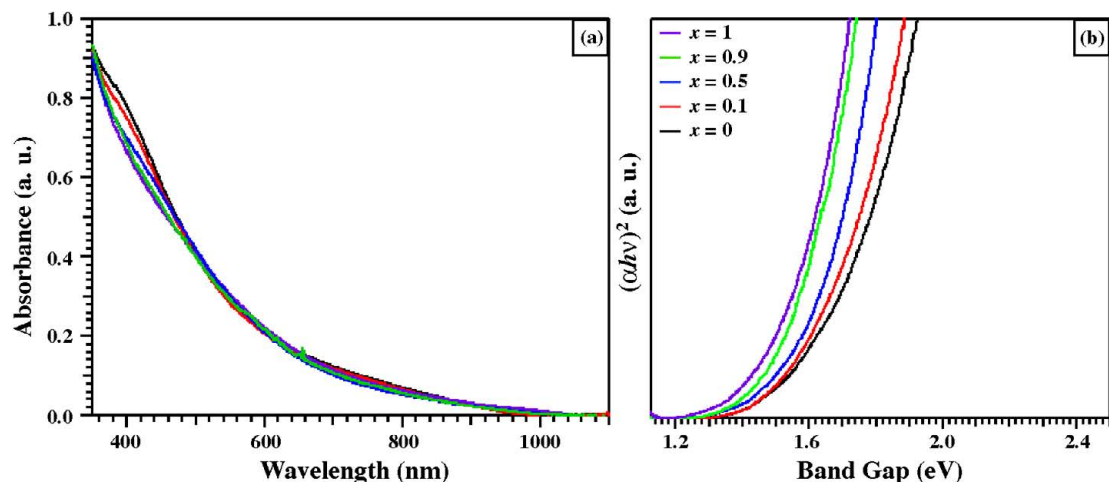


**Figure S6.3.** (a) Optical absorption of  $\text{Cu}_2\text{ZnSn}(\text{S}_{1-x}\text{Se}_x)_4$  nanocrystals with  $x$  varied from 0 to 1. (b) Plot of  $(\alpha h\nu)^2$  as a function of the photon energy for each CZTS,Se stoichiometry. The band gap demonstrates a red shift with increasing Se concentration.

suspend in non-polar solvents. At these temperatures, the surfactants are near or above their boiling points and may not adhere well to the growing nanocrystal surface. As a result more of the precursors are going to react on the nanocrystal surface, causing the particles to grow rapidly and uncontrollably. At lower growth temperatures, between 260 and 285 °C, we observed the optimal growth conditions. We could not go to lower temperatures without reducing the injection temperature, as the reaction flask did not cool fast enough for the low temperature to take effect. Additionally we explored longer growth times at 285 °C. Aliquots were taken in 15 minute increments up to 1 hour. Even after 15 minutes, the nanocrystals did not suspend in non-polar solvents indicating that the sizes were either too large or the nanocrystal surfaces were poorly capped.

Furthermore we also explored different surfactants as a way to control the size distribution. Typically Se precursors in hot injection syntheses are introduced as Se-phosphine complexes (i.e., trioctylphosphine selenide, TOPSe). Attempts to use TOP in our synthetic conditions resulted in little sulfur incorporation into the final nanocrystal

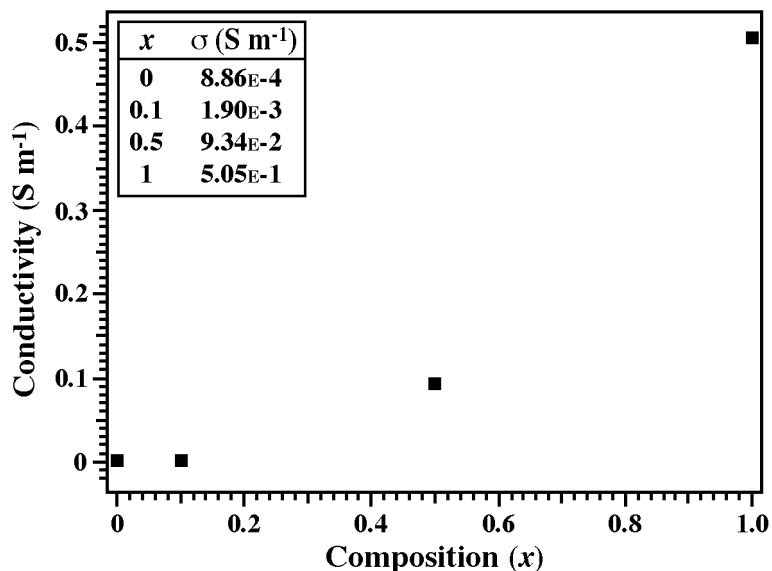


**Figure S6.4.** Conductivity determined from nanocrystal powders as a function of composition. An increase in the Se content leads to an increase in the conductivity.

product. This is likely due to the fact that TOPS reacts much more slowly than TOPSe, prohibiting control over the resulting composition. In addition to TOP, we also just heated the Se and S powders in OLA above the melting point of Se ( $\sim 220$  °C). Both the S and Se dissolved, however, similar results as when using TOP were observed. Because the flask had to be heated to above 220 °C, it is possible that some of the sulfur precursor started to decompose limiting its incorporation. Further attempts to control the size distribution are currently underway in our lab.

**Conductivity Measurements.** In order to test the hypothesis that the higher electrical conductivity—as a results of a decrease in band gap from the formation of Se-rich CZTS,Se—at the grain boundary is what leads to improved efficiencies, we did conductivity measurements on our CZTS,Se nanocrystal powders. Figure S6.4 plots the conductivity as a function of the composition. The conductivity was determined by sandwiching the nanocrystal powders between two copper plugs in a closed-cell device

and recording the current-voltage characteristics. The diameter of the spacing was 3 mm and the thickness 1 mm. From the I-V curve we determined the resistance that we could then convert to conductivity. These results show that the conductivity increases with Se content. This results suggest that there is less interfacial resistance in nanocrystal thin films (as-deposited or annealed) of Se-rich CZTS,Se alloys compared to S-rich CZTS,Se alloys. Therefore, it is reasonable that annealing CZTS thin films in a Se vapor would lead to better electron transport and give higher efficiencies, as has been observed in the literature.

## CHAPTER 7

### CU<sub>2</sub>SE NANOPARTICLES WITH DUAL FUNCTIONALITY DUE TO A CONTROLLED SOLID-STATE PHASE TRANSITION DRIVEN BY COPPER OXIDATION AND CATIONIC CONDUCTION

The contents in this dissertation chapter include the manuscript of a full article published in *The Journal of the American Chemical Society* **2011**, *133*, 1383-1390 and is available online at <http://dx.doi.org/10.1021/ja106254h>. This chapter is based on alternative ways to enhance carrier transport within nanocrystal thin films through controlled surface treatments. Furthermore, this article serves as the first reported synthesis of monoclinic stoichiometric Cu<sub>2</sub>Se nanocrystals.

The synthesis, device fabrication and conductivity studies were performed by Shannon C. Riha. Dr. Derek C. Johnson is credited for the XPS studies and XPS data fitting. The manuscript was prepared by Shannon C. Riha, with helpful insights, discussions, and editing by Dr. Derek C. Johnson and Prof. Amy L. Prieto.

## 7.1 Overview

Stoichiometric copper (I) selenide nanoparticles have been synthesized using the hot injection method. The effects of air exposure on the surface composition, crystal structure, and electronic properties were monitored using X-ray photoelectron spectroscopy (XPS), X-ray diffraction (XRD), and conductivity measurements. The current-voltage response changes from semiconducting to ohmic and within a week a 3000-fold increase in conductivity is observed under ambient conditions. The enhanced electrical properties can be explained by the oxidation of  $\text{Cu}^+$  and  $\text{Se}^{-2}$  on the nanoparticle surface, ultimately leading to a solid-state conversion of the core from monoclinic  $\text{Cu}_2\text{Se}$  to cubic  $\text{Cu}_{1.8}\text{Se}$ . This behavior is a result of the facile solid-state ionic conductivity of cationic Cu within the crystal and the high susceptibility of the nanoparticle surface to oxidation. This regulated transformation is enticing as one could envision using layers of  $\text{Cu}_2\text{Se}$  nanoparticles with dual functionality in optoelectronic devices simply by tuning the electrical properties for each layer through controlled oxidation.

## 7.2 Introduction

Transition metal chalcogenides are of current interest to energy-related research due to their semiconducting properties and the ability to tailor these properties through careful manipulation of the synthesis conditions. These materials have historically been made by energy intensive and ultra high vacuum solid-state techniques that result in a high fabrication cost. Current research is therefore focused on developing wet-chemical methods for the synthesis of high quality semiconducting nanomaterials as building blocks in optoelectronic devices.<sup>1-4</sup> Several solution-processed metal chalcogenide nanomaterials have been investigated as light harvesting materials for photovoltaics, such

as PbX (where X=S, Se, and Te),<sup>5-8</sup> Cu<sub>2</sub>S,<sup>9</sup> CuInS<sub>2</sub>,<sup>10,11</sup> CuInSe<sub>2</sub>,<sup>12,13</sup> CuIn<sub>x</sub>Ga<sub>1-x</sub>Se,<sup>14,15</sup> Cu<sub>2</sub>ZnSnS<sub>4</sub>,<sup>16-19</sup> and Cu<sub>2</sub>ZnSnSe<sub>4</sub>.<sup>20</sup> While the solution-based synthesis of these nanomaterials has been shown to be facile and applicable to a large class of compounds, the incorporation of such nanomaterials into fully functioning devices is not trivial.

A significant hurdle is that the surface of the chalcogenide nanomaterials is highly reactive due to the large number of unpassivated surface sites.<sup>21</sup> When exposed to oxygen, these surface sites often oxidize, thereby hindering their performance as a semiconducting material. This oxidation process is well documented; a well-studied example is thin films of lead chalcogenide nanoparticles incorporated into photovoltaic devices.<sup>5-8</sup> In addition to the highly reactive surface, the large density of nanoparticle interfaces in thin films serve as energy barriers, drastically reducing the interparticle electrical conductivity in nanostructured devices.<sup>22</sup> Because of these hurdles, new and innovative methods are required for the synthesis, deposition, and stabilization of semiconducting metal chalcogenide nanoparticles for device integration.

One way to overcome some of these limitations is to control the resistance of a nanostructured film. Tricoli and Pratsinis accomplished this by depositing films containing both semiconducting and conducting nanomaterials such as n-type SnO<sub>2</sub> and p-type CuO, respectively.<sup>22</sup> The conductive material therefore serves as nanoelectrodes that reduce the high film resistance, thereby lowering the electrical conductivity losses found in most nanoparticle films. However, this method requires the use of materials with different electronic structures and thus proper band alignment must be taken into consideration when choosing the semiconducting and conducting domains. To circumvent this, we have developed an approach to implement the same material as both

the semiconducting and conducting domains by controllably tuning the electronic properties of Cu<sub>2</sub>Se nanocrystals through time-resolved oxidation.

Stoichiometric Cu<sub>2</sub>Se and non-stoichiometric Cu<sub>2-x</sub>Se are p-type semiconductors that can exist in many different crystallographic systems including orthorhombic, monoclinic and cubic.<sup>23,24</sup> The optoelectronic properties of this material are promising, and potentially tunable, due to the wide range of possible crystal structures, particle size, and corresponding band gaps.<sup>24-29</sup> The band gap energy for both Cu<sub>2</sub>Se and Cu<sub>2-x</sub>Se is in the optimal range for use as an absorber material in photovoltaic devices. However, a widely varying indirect band gap of 1.1 to 1.5 eV<sup>27,30,31</sup> has been reported with a direct band gap between 2.0-2.3 eV.<sup>27,31,32</sup> While it has been shown that conductivity increases with increasing temperature—typical semiconducting behavior—many researchers also report observing an ohmic type response.<sup>27,33-45</sup> The wide range in observed band gap energies and varying electronic behavior is likely due to differences in the Cu to Se stoichiometry, recombination sites due to dislocations, large grain size distributions in polycrystalline films, size effects, and/or oxidation state of the Cu and Se.<sup>46</sup> Cu<sub>2</sub>Se contains Cu in the +1 oxidation state while the substoichiometric analog consists of multivalent Cu. When stoichiometric Cu<sub>2</sub>Se is exposed to air under ambient conditions, Cu<sup>+</sup> oxidizes to Cu<sup>+2</sup> forming a surface oxide. In bulk crystals, and most thin films, the effects of surface oxidation are negligible. However, the effect is much more profound for nanoparticles because the surface-to-volume ratio is large. The surface oxidation can therefore significantly alter the physical and/or electronic properties of the material. We aim to take advantage of this process and use it to controllably tune the electronic properties of the material. As demonstrated in the results and discussion section, oxidation of the nanoparticles leads to a solid-state conversion of Cu<sub>2</sub>Se to the superionic conductor,

$\text{Cu}_{1.8}\text{Se}$ , with a conductive coating. This coupled with the variability in crystal structure and stoichiometry makes  $\text{Cu}_2\text{Se}$  nanoparticles an interesting model system to investigate a mixed semiconducting and conducting nanocrystal film initially composed of the same compound.

Because of the flexibility present in the  $\text{Cu}_2\text{Se}$  family of compounds, both the structure and composition of the desired product must be controlled in order to tune the electronic and optical properties.<sup>47</sup> This control is exerted by carefully choosing the material synthesis procedure while simultaneously recognizing that the structure and stoichiometry are sensitive to the oxidation state of Cu as well as the high vapor pressure of Se.<sup>48</sup> We chose to pursue a one-pot solution phase synthesis that provides control over the oxidation state of the constituent elements<sup>49</sup> as well as the size and morphology of the resulting nanoparticles.<sup>29,50</sup> It also offers a scalable, cost-effective route allowing for flexible processing aimed at device fabrication. Recently, non-stoichiometric  $\text{Cu}_{2-x}\text{Se}$  nanocrystals via a one-pot synthesis has been reported resulting in beautiful morphologies and narrow size distributions.<sup>51,52</sup> To our knowledge, this is the first reported one-pot solution phase synthesis of stoichiometric  $\text{Cu}_2\text{Se}$  nanoparticles without the initial presence of the substoichiometric phase. Through drop casting thin films of stoichiometric  $\text{Cu}_2\text{Se}$  nanoparticles, we developed the initial steps which allow the assembly of functional energy-related devices from a single material by controlling the surface oxidation and resulting solid-state conversion to  $\text{Cu}_{1.8}\text{Se}$ .

### 7.3 Results and Discussion

Figure 7.1a and 7.1b contains representative TEM and HR-TEM images of  $\text{Cu}_2\text{Se}$  synthesized by simultaneously injecting TOPSe and TOPCu from separate syringes into

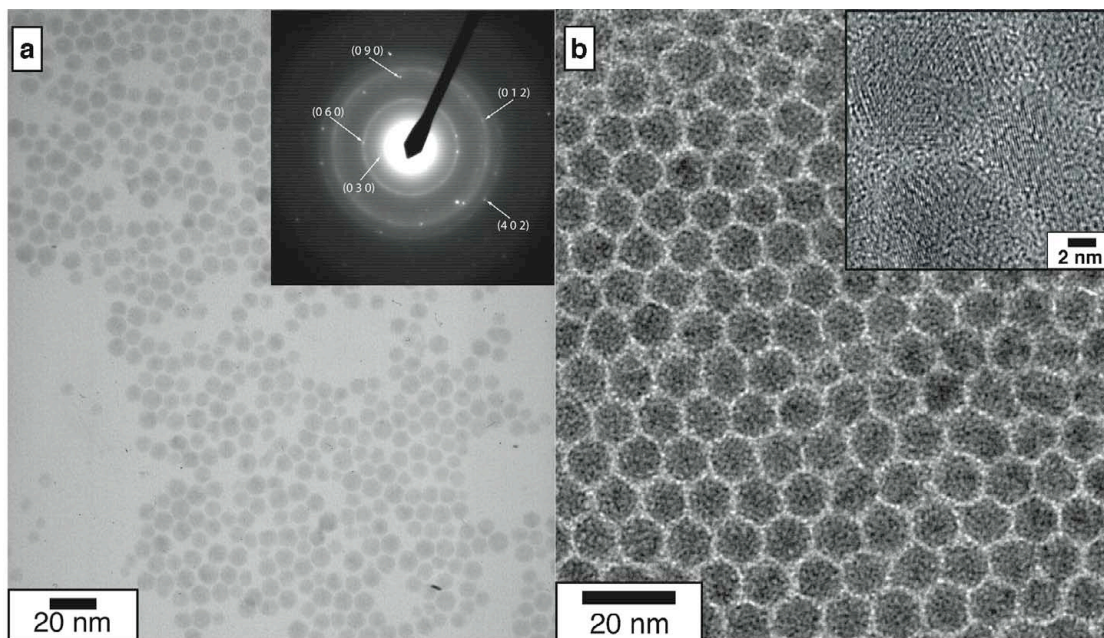


**Figure 7.1.** (a) TEM and (b) HR-TEM images of  $\text{Cu}_2\text{Se}$  nanoparticles synthesized via simultaneous injection of TOPSe and TOPCu. Inset (a), SAED pattern of the nanoparticles indexed to stoichiometric monoclinic  $\text{Cu}_2\text{Se}$ . Inset (b), HR-TEM image showing the crystallinity of the nanoparticles.

the reaction flask at the same rate. This procedure produced monodispersed nanocrystals with a hexagonal morphology that arranged in a close-packed configuration. A characteristic SAED pattern of the nanoparticles (Figure 7.1a inset) is indexed to the (030), (060), (090), (012) and (402) reflections of monoclinic  $\text{Cu}_2\text{Se}$ . In addition, multiple lattice fringes were observed in the HR-TEM image contained in Figure 7.1b (inset). The measured spacings of 3.4 Å, 2.3 Å, and 2.1 Å correspond to the (060), (090), and (012) planes of monoclinic  $\text{Cu}_2\text{Se}$ , respectively, thereby corroborating the indexed SAED pattern. Particle size analysis performed on the sample yielded an average size of  $10.1 \pm 0.8$  nm, corresponding to a monodispersity of 8.1% (Figure S7.1a). However, as illustrated in Figure S7.1b, when the injection rate, sonication time, and injection and growth temperature were altered, monodispersed nanoparticles could not be synthesized.

This result demonstrates that the above mentioned synthesis conditions were the three key parameters that control the Cu<sub>2</sub>Se nanoparticle nucleation and growth. Of the three, the most important aspect was temperature, as variation of both the injection and growth temperature led to inconsistent results. This is because the injection temperature controls the particle nucleation kinetics.<sup>53</sup> In this case, the injection temperature must be high enough to immediately decompose the Cu and Se precursors, thereby promoting instantaneously nucleation of the desired nanoparticles. Nucleation was then followed by nanocrystal growth, which was also temperature dependent. This is due to the fact that the growth temperature controls the stability, diffusion rate, and binding strength of the surfactant to the growing nanocrystal surface, ultimately affecting the growth rate.<sup>53</sup> When the growth temperature was above 290 °C, uncontrolled growth occurred leading to a bimodal size distribution. At temperatures below 275 °C, the growth rate was too slow, which also resulted in a broad size distribution. Based on these results, it was determined that an injection temperature of 300 °C and a growth temperature of 285 °C was optimal for the synthesis of monodisperse Cu<sub>2</sub>Se nanoparticles.

The nanoparticle size and size distribution was also a function of precursor injection rate. When the injection rate was different for each precursor, a bimodal size distribution was observed. This is not surprising as different precursor injection rates would lead to a variation in the relative ratios of the Cu and Se precursors, ultimately inducing multiple instantaneous nucleation events. Similar results were obtained when the TOPSe and TOPCu were combined into one syringe prior to injection. This could be attributed to heterogeneity of the combined precursor solution and/or a reaction occurring between the Cu and Se precursors before injection. The best results were obtained when TOPSe and TOPCu were in separate syringes but injected at the same time and rate. Because Cu<sub>2</sub>Se

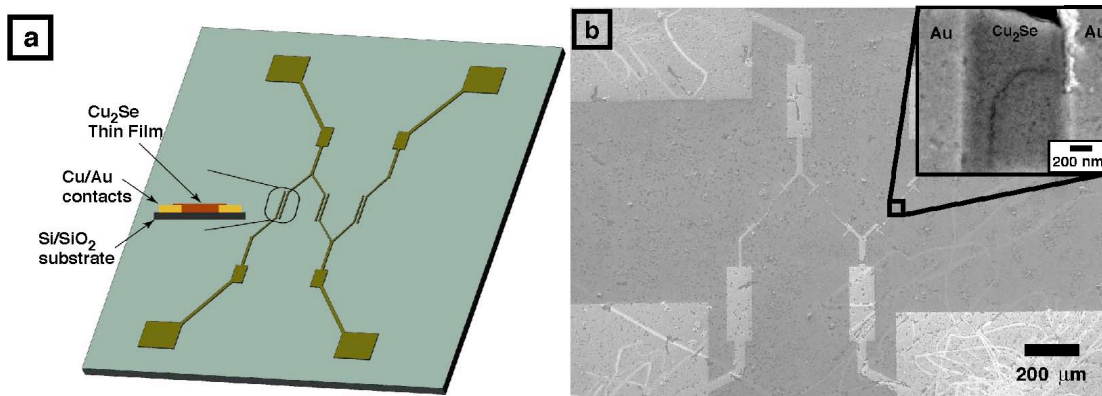


**Figure 7.2.** (a) Schematic representation of a  $\text{Cu}_2\text{Se}$  nanocrystal thin film device. (b) SEM micrograph of a device. The inset is a high-resolution image of the thin film overlaying the two electrodes.

is a promising candidate for photovoltaic applications, the transport properties of thin films fabricated by drop-casting solutions of  $\text{Cu}_2\text{Se}$  nanoparticles were measured.

Devices consisting of the  $\text{Cu}_2\text{Se}$  nanoparticles were assembled using EBL with a design similar to that employed by Bawendi and coworkers (Figure 7.2a).<sup>54,55</sup> Figure 7.2b contains a scanning electron micrograph of a chip showing three characteristic devices used for testing. The inset clearly shows a continuous  $\text{Cu}_2\text{Se}$  film of nanoparticles (darker gray middle region) bridging two Au electrodes (light gray outer regions). To ensure that the observed current came from the nanocrystalline film, current measurements as a function of voltage were collected from the  $\text{SiO}_2$  substrate and the Au electrodes resulting in open circuit and metallic behavior, respectively. To determine if the electronic properties of a device containing  $\text{Cu}_2\text{Se}$  nanoparticles can be regulated through a time controlled oxidation of the film, I-V measurements were collected before and after exposure to atmosphere.

The inset in Figure 7.3 contains plots of the current as a function of voltage collected from devices illustrated in Figure 7.2 that were protected in a nitrogen atmosphere prior to oxygen exposure. The symmetric S-shaped curve measured from the film is indicative

of a semiconductor with a maximum current of  $\pm 4$  nA at  $\pm 1$  V. When kept in an inert environment, the current response remained unchanged over 48 hrs. The stability of the Cu<sub>2</sub>Se nanoparticle thin film was then evaluated in air by measuring the I-V response immediately after removing the device from the nitrogen glovebox. The current response was subsequently evaluated hourly for six hours. The data curves for the first seven measurements are plotted in Figure 7.3. The initial scan conducted outside the nitrogen glovebox exhibited semiconducting behavior with a slight increase in current to 5.4 nA, a difference of ca. 1.5 nA when compared to the 48 hr measurement collected inside the box before the device was exposed to air. Similar results were obtained after 1 hr of exposure to air with a doubling of the maximum current measured before air exposure. However, after 2 hrs of exposure a substantial increase in current was observed and the I-V curve transitioned to an almost linear response, indicating more ohmic than semiconducting behavior. As illustrated in Figure 7.3 and S7.2a, this trend continued with an increase of almost two orders of magnitude in the current output after 6 hrs of air exposure. The ohmic response continued with a drastic rise in current to 5  $\mu$ A after 24 hrs of air exposure and a slight increase to 6 mA after 48 hrs. The maximum current of 13.5  $\mu$ A, a 3000-fold increase from the initial response, was observed after 1 wk with a subsequent decrease to 6.5  $\mu$ A after 2 wks of exposure. The change in behavior from semiconducting to ohmic, as well as the increase in current response by over three orders of magnitude, demonstrated the potential to tune the electronic properties of Cu<sub>2</sub>Se nanoparticles through controlled oxidation.

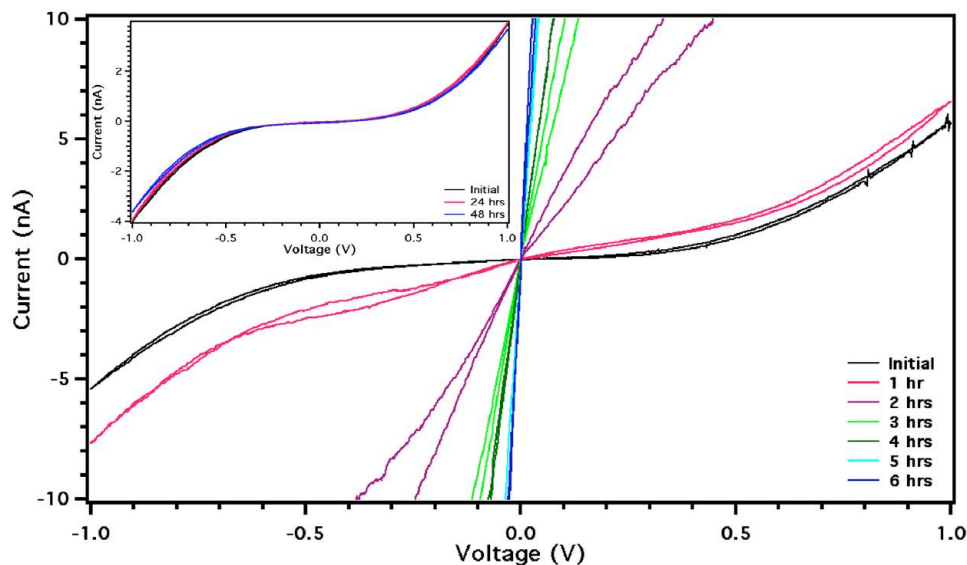


**Figure 7.3.** Current-voltage measurements of a  $\text{Cu}_2\text{Se}$  nanoparticle thin film taken as a function of time exposed to air. Measurements are taken immediately following removal from the glovebox and then once an hour for the subsequent 6 hrs. The inset illustrates the semiconducting behavior of the film when kept in an inert environment for the initial, 24 hour and 48 hour current-voltage measurements recorded inside the glovebox.

As mentioned above, it is well known that  $\text{Cu}^+$  in  $\text{Cu}_2\text{Se}$  can oxidize to  $\text{Cu}^{+2}$  when exposed to air, a process that is enhanced in nanoparticles due to a high density of surface sites. In addition to being highly reactive, nanoparticles allow one to monitor chemical and crystallographic changes that may not be observable in the bulk material. Using XRD and XPS, the oxidative induced changes in  $\text{Cu}_2\text{Se}$  as a function of exposure time to air were monitored in order to better understand the observed change in electronic properties. Beginning with a systematic XRD investigation,  $\text{Cu}_2\text{Se}$  samples were prepared in a nitrogen atmosphere in order to prevent oxidation. Once removed, an initial XRD pattern was immediately collected and the sample was then stored under ambient conditions between subsequent measurements for time intervals consistent with the electronic transport study (initial, 24 hr, 48 hr, 1 wk and 2 wks). The XRD patterns are

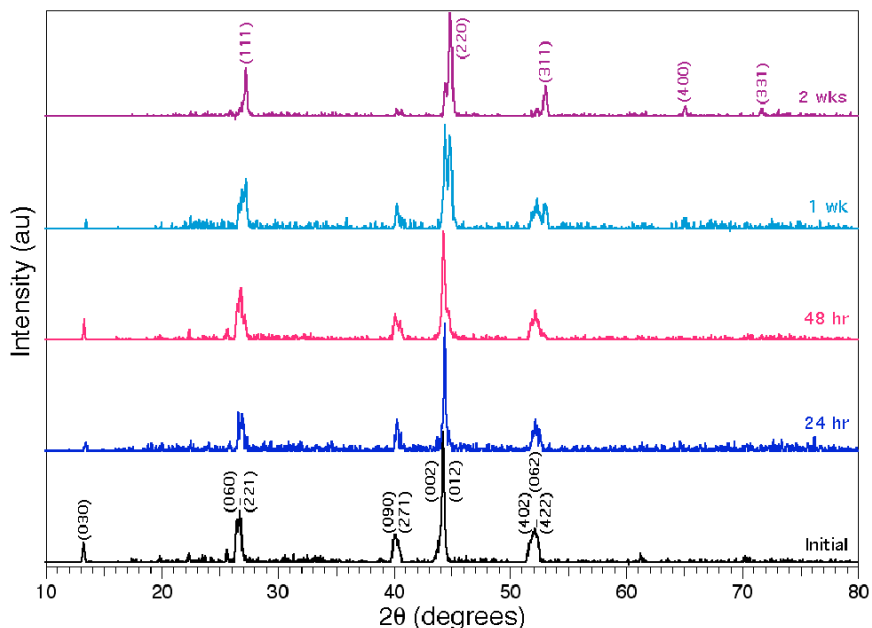


**Figure 7.4.** XRD patterns of  $\text{Cu}_2\text{Se}$  nanoparticles as a function of air exposure. The initial pattern was taken immediately after the sample was removed from the glovebox. That pattern is indexed to monoclinic  $\text{Cu}_2\text{Se}$  (JCPDS 27-1131). As the exposure time increases, the peaks shift to higher  $2\theta$  until the particles are converted to cubic  $\text{Cu}_{1.8}\text{Se}$  (JCPDS 71-0044).

stacked in Figure 7.4 as a function of time to clearly show the transformation of the  $\text{Cu}_2\text{Se}$  nanoparticle crystal structure to  $\text{Cu}_{1.8}\text{Se}$  when exposed to air.

The diffraction peaks in the initial pattern presented in Figure 7.4 have been indexed to monoclinic  $\text{Cu}_2\text{Se}$  (JCPDS 27-1131), thereby confirming the reflection assignments in the SAED pattern shown in Figure 7.1. All peaks could be assigned, suggesting that no crystalline impurities were present. There was a slight shift to higher  $2\theta$  for all peaks in the XRD pattern of the sample exposed to air for 24 hrs, indicating a decrease in the lattice parameters when compared to the initial sample. After 48 hrs, however, a shoulder was apparent at higher  $2\theta$  for the peak located at  $44^\circ$ , which became more pronounced as the exposure time increased. The shoulder eventually developed into a separate peak while peaks corresponding to the copper deficient  $\text{Cu}_{1.8}\text{Se}$  began to emerge. After 2 wks of exposure, all of the diffraction peaks were assigned to cubic  $\text{Cu}_{1.8}\text{Se}$

(JCPDS 71-44) suggesting a complete solid-state conversion. This conversion is enticing because  $\text{Cu}_{1.8}\text{Se}$  is cubic, instead of monoclinic, and Cu deficient when compared to  $\text{Cu}_2\text{Se}$ . Because of these variations, the substoichiometric material also has different material properties. The solid-state conversion to substoichiometric  $\text{Cu}_{1.8}\text{Se}$  in conjunction with an approximate 3000-fold increase in conductivity clearly demonstrates that initially fabricating a functional device with stoichiometric  $\text{Cu}_2\text{Se}$  and controllably oxidizing it can result in films with tunable electronic properties.

To further understand the mechanism behind the solid-state conversion demonstrated by the time-resolved XRD analysis, a systematic XPS study was performed to investigate the oxidation states of both the Cu and Se atoms as a function time when exposed to air. The evolution of the Cu2p XPS spectra contained in Figure 7.5a as a function of exposure time shows a clear oxidation from  $\text{Cu}^+$  to a mixture of  $\text{Cu}^+$  and  $\text{Cu}^{+2}$ . As illustrated in Figure 7.5b, the initial  $\text{Cu}2p_{3/2}$  and  $\text{Cu}2p_{1/2}$  peaks were symmetric, narrow, and devoid of satellite peaks. This spectrum is indicative of monovalent copper. When the  $\text{Cu}_2\text{Se}$  sample was exposed to oxygen for two weeks, however, the Cu2p peaks in the spectrum contained in Figure 7.5c broaden and undergo splitting while pronounced satellite peaks form due to paramagnetic  $\text{Cu}^{+2}$ . Since XPS is primarily a surface characterization technique, this dramatic change in the spectra can be attributed to the oxidation of a significant portion of the surface  $\text{Cu}^+$ , resulting in the presence of mixed valent  $\text{Cu}^{+ +2}$ .

The Se atoms were also evaluated using XPS techniques and underwent a similar conversion when exposed to oxygen. Figure 7.6a contains Se3d spectra that clearly show a shift to higher binding energy with an increase in exposure time. The  $\text{Cu}_2\text{Se}$  spectrum plotted in Figure 7.6b for a sample not exposed to oxygen contains  $\text{Se}3d_{5/2}$  and  $\text{Se}3d_{3/2}$  peaks, which in addition to appearing symmetric and narrow, demonstrates the

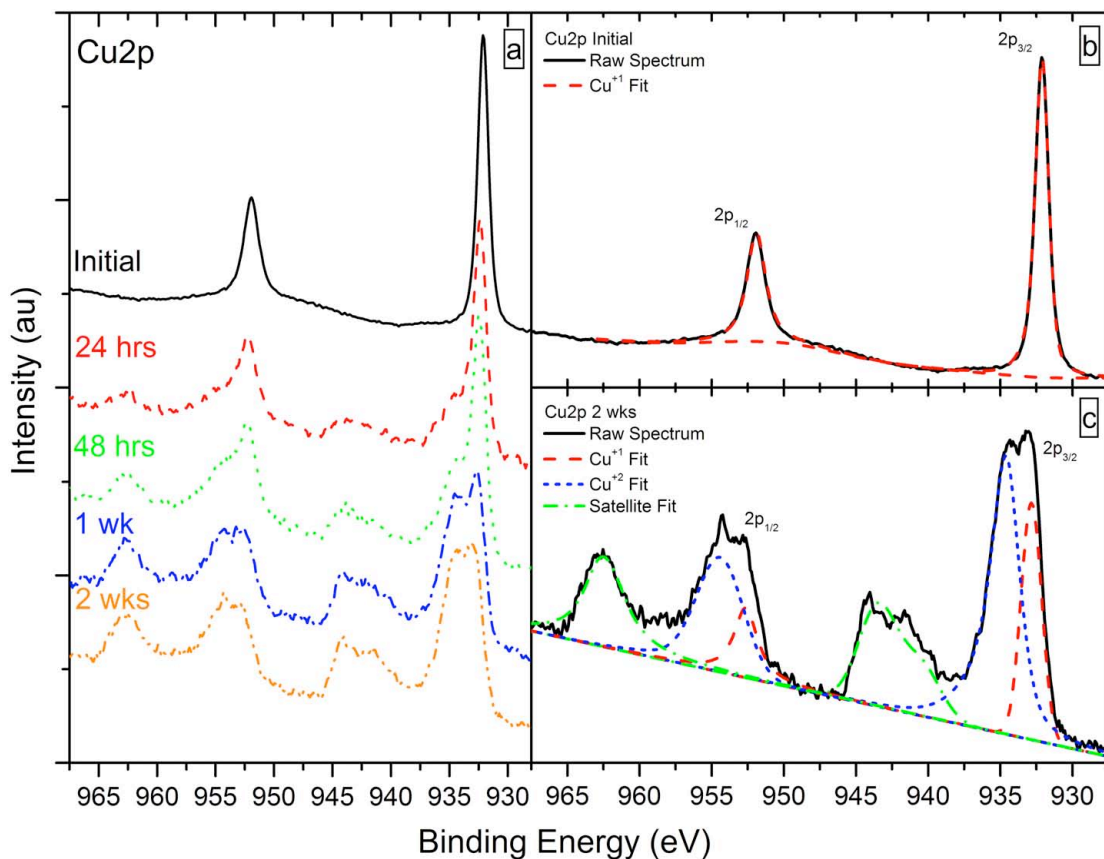


**Figure 7.5.** (a) Change in the Cu2p XPS spectra after exposure to oxygen. (b) Initial XPS spectrum of the Cu2p region as well as the Cu2p<sub>3/2</sub> and Cu2p<sub>1/2</sub> peak fit used to calculate atomic ratios. (c) XPS spectrum of the Cu2p region with peak fits for Cu(I), Cu(II) and satellites due to the paramagnetic Cu(II) after the sample had been exposed to oxygen for two weeks.

characteristic shape of Se<sup>-2</sup> in a consistent bonding environment. That is, the Se3d<sub>3/2</sub> peak is at a binding energy 0.86 eV higher than the Se3d<sub>5/2</sub> peak and the spin-orbital splitting ratio is 2/3.<sup>56</sup> The observed binding energy of 53.9 eV for the Se3d peak is also in agreement with what has been previously reported in the literature for Cu<sub>2</sub>Se,<sup>57</sup> further confirming the indexed XRD and SAED patterns. However, once exposed to air for two weeks, the Se spectrum contained in Figure 7.6c contains two very distinctive peaks around 54 and 58.5 eV. The fitting of these peaks was evidence of multiple oxidation states ranging from the selenide to the oxide species. The evolution of the Cu and Se

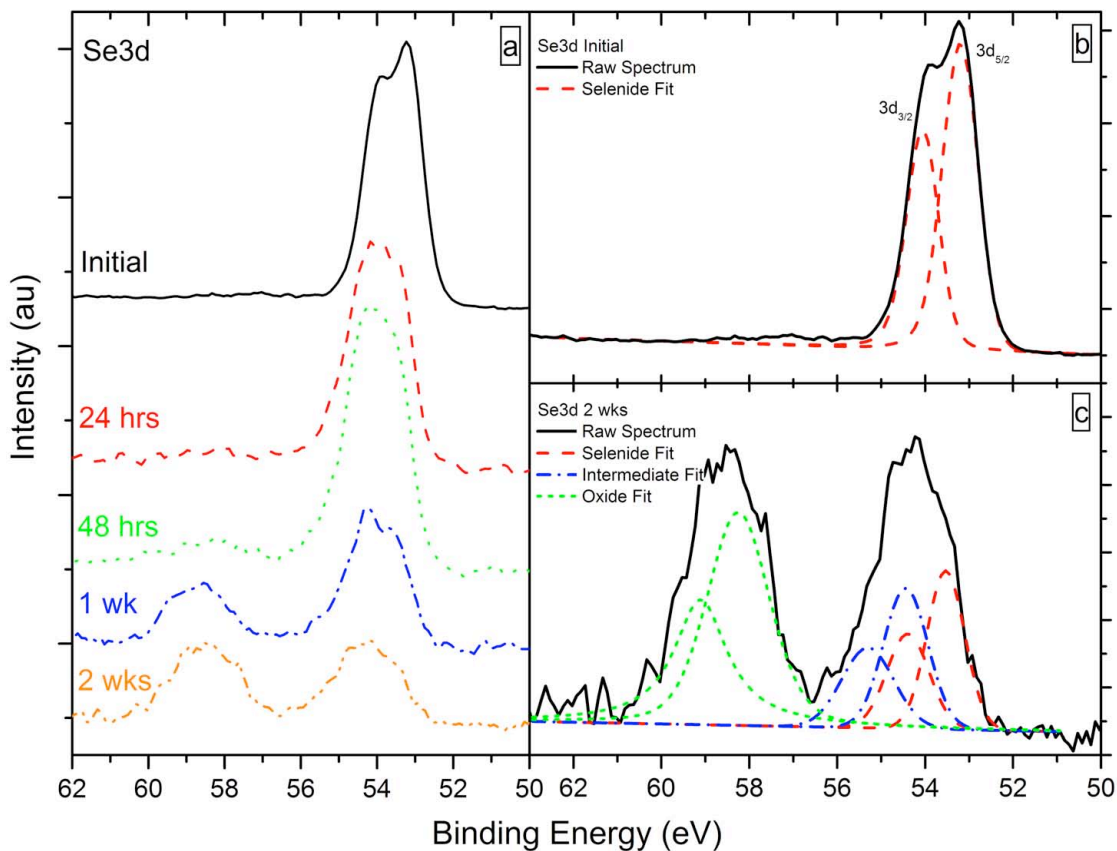


**Figure 7.6.** (a) Change in the Se3d XPS spectra after exposure to oxygen. (b) Initial XPS spectrum of the Se3d region as well as the Se3d<sub>5/2</sub> and Se3d<sub>3/2</sub> peak fit used to calculate atomic ratios. (c) Characteristic XPS spectrum of the Se3d region with Se(II-, due to the selenide), an intermediate oxidation state (roughly correlating to Se(0)) and Se(IV, likely due to SeO<sub>2</sub>) peak fits for the sample that had been exposed to oxygen for two weeks.

spectra were analyzed in more detail in order to shed light on the changing crystal structure and chemical composition of the nanoparticles.

An evaluation of the initial Cu2p<sub>3/2</sub> and Se3d<sub>5/2</sub> peak areas yielded a Cu to Se atomic ratio of 2.0:1.0, demonstrating that the initial sample was Cu<sub>2</sub>Se. As the solid-state conversion progressed, for which the XPS spectra of Cu and Se are presented in panels a-e of Figures S7.3 and S7.4, respectively, the atomic ratio increased from an initial value of 2.0:1.0 to 5.2:1.0. A bar graph illustrating the evolution of the atomic ratio as a function of exposure time is plotted in Figure S7.3f. These data, coupled with the XRD

analysis that indicated a solid-state conversion from  $\text{Cu}_2\text{Se}$  to  $\text{Cu}_{1.8}\text{Se}$ , suggested that solid-state diffusion of cationic Cu from the particle core to the surface occurred. This is not surprising because Se atoms are not mobile in this particular crystal structure while the diffusion of cationic Cu has been shown to be facile.<sup>35,58-60</sup> Consequently, as illustrated in Figure S7.3f, the surface  $\text{Cu}^+$  oxidized to  $\text{Cu}^{2+}$  upon exposure to oxygen, thereby establishing a chemical potential gradient that resulted in the diffusion of  $\text{Cu}^+$  from the particle core to the surface. Equilibrium was achieved when the conversion to more air-stable  $\text{Cu}_{1.8}\text{Se}$  was complete, at which ca. 80% of the surface Cu existed as  $\text{Cu}^{2+}$  in the form of conductive copper oxide,  $\text{CuO}$ ; copper hydroxide,  $\text{Cu}(\text{OH})_2$ ; copper selenite,  $\text{CuSeO}_2$ ; or their combination.<sup>8,61</sup>

As with Cu, the Se atoms oxidized when exposed to oxygen. Initially,  $\text{Se}^{-2}$  was the only Se species present. In 24 hrs, however, ca. 45% of the selenide species was converted to an intermediate species with an oxidation state more positive than that of  $\text{Se}^{-2}$  with a smaller percentage of ca. 5% being converted to  $\text{Se}^{+4}$ , tentatively identified as  $\text{SeO}_2$ . The intermediate Se species could be in the form of polyselenide. With the formation of Cu-O adducts, a sufficient number of Cu-Se bonds have to be broken; the free Se atoms could then form short polyselenide (Se-Se-Se) chains on the surface causing the shift in the XPS spectra to higher binding energy.<sup>62</sup> However, due to the complexity of the Se3d spectra for samples exposed to oxygen, relating the oxidation state of the intermediate species to an absolute binding energy was problematic as the binding energy shifts for different Se compounds are small.<sup>56</sup> Nonetheless, it was obvious when analyzing the spectra shown in Figure S7.4a-e that as the oxygen exposure time increased, Se was converted from the anion to the fully oxidized cation through an intermediate species. As illustrated in Figure S7.4f, a majority of the surface Se has been

converted to the oxide after 2 wks of exposure, while approximately equal amounts of the selenide and intermediate species were present. In bulk samples, the oxidation of both Cu and Se surface sites would have little effect on the physical and electronic properties of the material. On the contrary, when the size is reduced to the nanoscale, the effects of surface oxidation can alter both the physical and electronic properties. This was further elucidated in the optical properties of  $\text{Cu}_2\text{Se}$ , where the UV-Vis spectra are shown in Figure S7.5. Time resolved UV-Vis measurements show that after 24 h of air exposure the indirect band gap increases from 1.3 eV to 1.4 eV, while the direct band gap increases from 2.2 eV to 2.4 eV. This change in band gap energy remains constant after 2 weeks and may explain the large variations of reported literature values.<sup>27,30-32</sup> Because of this fact, the dramatic changes observed in the time resolved XRD and XPS data, coupled with the UV-vis data, are reconciled with the transformation from semiconducting to an ohmic response of the  $\text{Cu}_2\text{Se}$  nanoparticle devices.

The XRD and XPS data contained in Figures 7.4-7.6 mimic the observed trends in the I-V curves plotted in Figure 7.3 and S7.2. A  $\text{Cu}_2\text{Se}$  sample not exposed to oxygen was composed of  $\text{Cu}^+$  and  $\text{Se}^{-2}$  with a Cu:Se ratio of 2.0:1.0 without a surface oxide layer. The semiconducting behavior was therefore dictated by the intrinsic properties of the  $\text{Cu}_2\text{Se}$  nanoparticles and the interparticle contact resistance. After 24 hrs of air exposure, however, the resistance dropped significantly manifesting as a large increase in the maximum current. This behavior can be explained by the presence of conducting CuO and intermediate Se species on the surface of the nanoparticles as well as the solid-state conversion to the superionic conductor  $\text{Cu}_{1.8}\text{Se}$ . As the Cu was oxidized to  $\text{Cu}^{+2}$ , for which the surface  $\text{Cu}^+$  decreased to ca. 50% its original concentration in 24 hrs (Figure S7.2f), a chemical potential gradient was established within the particle. This resulted in

the solid-state diffusion of cationic Cu from the particle core to the surface, making the particle core Cu deficient. As the Cu deficiency increased, more holes are generated thereby increasing the majority charge carrier concentration.<sup>63</sup> As illustrated in Figure 7.4, equilibrium was reached when the particles were converted to the substoichiometric  $\text{Cu}_{1.8}\text{Se}$ . The drop in the maximum current from 1 wk to 2 wks can be explained by the conversion of surface Se from an intermediate species to the oxide. As illustrated by Figure S7.4f, the relative ratio of the fully oxidized species to the intermediate species became greater than one between 1 wk and 2 wks. This is important because the binding energy of the Se intermediate is close to that exhibited by zero valent Se, which provides more charge carriers at the expense of less energy than the oxide species. However, the formation of a significant Se surface oxide could increase the interparticle resistance and mitigate the increase in charge carriers generated within and on the surface of the particles due to the solid-state conversion and CuO formation, respectively.

#### **7.4 Conclusions**

A methodology has been created to implement the same material in energy-related devices as both the semiconducting and conductive domain by controllably tuning the electronic properties of  $\text{Cu}_2\text{Se}$  nanocrystals through time-resolved oxidation. To accomplish this, a synthesis procedure for monodispersed  $\text{Cu}_2\text{Se}$  nanoparticles without the presence of substoichiometric  $\text{Cu}_{1.8}\text{Se}$  was developed for which three key variables for controlling size and size distribution were identified. Upon optimization of these parameters—*injection temperature, growth temperature, and injection rate*—reproducible, monodisperse  $\text{Cu}_2\text{Se}$  nanoparticles with a diameter of  $10.1 \pm 0.8$  nm were synthesized. Thin film devices of these nanoparticles were subsequently prepared

by drop casting onto EBL fabricated Au contacts. These devices initially demonstrated semiconducting behavior; however after one week of exposure to oxygen, a 3000-fold increase in conductivity and a change to ohmic behavior was observed. XRD and XPS studies suggest the change in conductivity is due to Cu<sub>2</sub>Se nanoparticles readily reacting with oxygen, ultimately leading to a solid-state conversion to Cu<sub>1.8</sub>Se.

## 7.5 Experimental Details

**Chemicals.** Selenium powder (99.99%), copper acetate hydrate (98%), technical grade trioctylphosphine (TOP, 90%), trioctylphosphine oxide (TOPO, 99.9%), methylisobutyl ketone (MIBK, 99+%), and ACS grade isopropyl alcohol (IPA, >99.5%) were purchased from Sigma Aldrich. Octylphosphonic acid (OPA) was purchased from PCI Synthesis. Poly(methylmethacrylate) (PMMA), both 495K MW and 950K MW, were purchased from MicroChem. The chemicals were used as received without further purification. All anhydrous solvents were freeze-pump-thawed to remove any dissolved oxygen prior to use.

**Cu<sub>2</sub>Se Nanoparticle Synthesis.** Nanoparticles of Cu<sub>2</sub>Se were prepared under inert conditions using standard Schlenk line and glovebox techniques.<sup>50,64-68</sup> In a typical synthesis, a mixture of 4.6 mmol TOPO and 2 mmol OPA in a 50 mL 3-neck round bottom flask were prepared in a nitrogen glovebox. Equipped with a stir bar, thermocouple, and reflux condenser, the reaction flask was sealed with rubber septa, transferred to an Ar Schlenk line where it was degassed at 70 °C and subsequently heated to 300 °C at a rate of 500 °C/hr. In two separate vials, precursor solutions of copper (TOPCu) and selenium (TOPSe) were prepared in the glovebox by combining 1 mmol copper acetate hydrate in 2.5 mmol TOP and 1 mmol selenium powder in 1.5 mmol TOP.

Both vials were sealed with rubber septa and the as-prepared solutions were then taken out of the glovebox and sonicated until the selenium powder completely dissolved and the TOPCu became a light aqua green. After sonicating, the TOPCu and TOPSe solutions were loaded into separate 2.5 mL gas tight Luer Lock syringes and rapidly injected into the reaction flask containing the TOPO/OPA solution simultaneously. After injection, the growth temperature was lowered to 285 °C and the reaction was allowed to proceed for 13 min. The reaction was then quenched by injecting the product into degassed toluene.

Purification of the Cu<sub>2</sub>Se nanoparticles was performed in the glovebox using degassed solvents to avoid surface oxidation. The resulting product solution was centrifuged in excess toluene for 20 minutes to remove any residual bulk product. The supernatant was decanted and transferred to another centrifuge tube where 2.5 mL acetonitrile was added and the resulting murky-brown solution was centrifuged for another 20 minutes. The supernatant was again decanted and transferred to a fresh centrifuge tube. Methanol was then used to precipitate the remaining nanoparticles from the supernatant, which were subsequently redispersed in toluene. Methanol was added a second time to remove any excess surfactant and the resulting Cu<sub>2</sub>Se nanoparticles were stored in toluene for future characterization.

***Transmission electron microscopy (TEM).*** TEM images and selected area electron diffraction (SAED) were collected using a JEOL JEM-2000 transmission electron microscope under a working voltage of 160 kV. High-resolution TEM (HR-TEM) images were obtained with a Philips CM200 STEM using a working voltage of 200 kV. The TEM samples were created by dipping a carbon-coated copper grid in a toluene solution containing the nanoparticles three times.

***X-ray diffraction (XRD).*** Powder XRD was performed on a Scintag X-2 Advanced Diffraction System equipped with Cu K $\alpha$  radiation with a wavelength of 1.54 nm. Samples were prepared in the glovebox from a slurry of Cu<sub>2</sub>Se nanoparticles in toluene. The samples were subsequently dried under inert conditions and XRD patterns were taken immediately after removal from the glovebox as well as after 24 hrs, 48 hrs, 1 week, and 2 weeks of oxygen exposure.

***UV-vis.*** UV-vis spectra were collected for Cu<sub>2</sub>Se thin films using an Agilent 8453 UV-Visible ChemStation Spectrophotometer. The thin films were prepared on quartz microscope slides inside a nitrogen glovebox, and the UV-VIS was taken immediately after removal from the glovebox, and at 24 h, 48 h, 1 wk, and 2 wks of air exposure.

***X-ray photoelectron spectroscopy (XPS).*** XPS spectra were obtained using a Physical Electronics ESCA 5800 system employing monochromatic Al K $\alpha$  (E = 1486.6 eV) as the X-ray source. High-resolution scans were utilized to confirm the presence and provide information regarding the bonding environment and oxidation state of Cu and Se. These scans were performed with a pass energy of 23.5 eV and a step size of 0.10 eV/step. All spectra were shifted to account for sample charging using inorganic carbon as a reference to 284.80 eV.

***Conductivity measurements.*** Current-voltage (I-V) measurements were taken employing a two-probe method using a Compactstat Electrochemical Interface potentiostat with a step size of 2 mV and a scan rate of 2.5 mV/s. Devices were fabricated by spin-coating a layer of 495K MW PMMA, followed by a second layer of 950K MW PMMA, onto a silicon chip with a 100 nm thermal oxide layer. Electron beam lithography (EBL) was employed to draw electrodes spaced 500-600 nm apart. A developing solution of methyl-isobutyl ketone and isopropanol in a 1:2 volume/volume

ratio was subsequently used to develop the features. Approximately 20 nm of chromium and 80 nm of gold were evaporated onto the substrates. The chips were then submersed in acetone to remove the remaining PMMA. To avoid oxygen contamination, a suspension of Cu<sub>2</sub>Se nanoparticles was drop-cast onto the chip in the glovebox following a procedure previously reported in the literature.<sup>69</sup> Briefly, a metal stub was placed in the center of a recrystallization dish and 2 mL of degassed toluene was added. The substrate with the evaporated metal contacts was positioned on top of the stub and 10 drops of the Cu<sub>2</sub>Se nanoparticle solution was placed on the substrate. A watch glass covered the recrystallization dish to slow the evaporation rate. This process was repeated three times to ensure a uniform film of nanoparticles between the metal contacts. Current-voltage measurements of the nanocrystalline film were collected both in the glovebox and after the film was exposed to air.

## **7.6 Acknowledgements**

This work was supported by start-up funds from Colorado State University. The authors' thank Dr. Sandeep Kohli (XRD) and Dr. Pat McCurdy (XPS) for their technical assistance as well as Mr. Vern Robertson from JEOL.

## 7.7 References

- (1) Talapin, D. V.; Lee, J.-S.; Kovalenko, M. V.; Shevchenko, E. V. *Chem. Rev.* **2010**, *110*, 389-458.
- (2) Kamat, P. *J. Phys. Chem. C* **2008**, *112*, 18737-18753.
- (3) Hillhouse, H. W.; Beard, M. C. *Curr. Opin. Colloid Interface Sci.* **2009**, *14*, 245-259.
- (4) Kamat, P. *J. Phys. Chem. C* **2007**, *111*, 2834-2860.
- (5) Law, M.; Luther, J. M.; Song, Q.; Hughes, B. K.; Perkins, C. L.; Nozik, A. J. *J. Am. Chem. Soc.* **2008**, *130*, 5974-5985.
- (6) Luther, J. M.; Law, M.; Beard, M. C.; Song, Q.; Reese, M. O.; Ellingson, R. J.; Nozik, A. J. *Nano Lett.* **2008**, *8*, 3488-3492.
- (7) Luther, J. M.; Law, M.; Song, Q.; Perkins, C. L.; Beard, M. C.; Nozik, A. J. *ACS Nano* **2008**, *2*, 271-280.
- (8) Sykora, M.; Kopolov, A. Y.; McGuire, J. A.; Schulze, R. K.; Tretiak, O.; Pietryga, J. M.; Klimov, V. I. *ACS Nano* **2010**, *4*, 2021-2034.
- (9) Wu, Y.; Wadia, C.; Ma, W.; Sadtler, B.; Alivisatos, A. *Nano Lett.* **2008**, *8*, 2551-2555.
- (10) Koo, B.; Patel, R. N.; Korgel, B. A. *Chem. Mater.* **2009**, *21*, 1962-1966.
- (11) Zhong, H. Z.; Zhou, Y.; Ye, M. F.; He, Y. J.; Ye, J. P.; He, C.; Yang, C. H.; Li, Y. F. *Chem. Mater.* **2008**, *20*, 6434-6443.
- (12) Basol, B. M.; Kapur, V. K.; Norsworthy, G.; Halani, A.; Leidholm, C. R.; Roe, R. *Electrochem. Solid-State Lett.* **1998**, *1*, 252-254.
- (13) Koo, B.; Patel, R. N.; Korgel, B. A. *J. Am. Chem. Soc.* **2009**, *131*, 3134-3135.
- (14) Panthani, M. G.; Akhavan, V.; Goodfellow, B.; Schmidtke, J. P.; Dunn, L.; Dodabalapur, A.; Barbara, P. F.; Korgel, B. A. *J. Am. Chem. Soc.* **2008**, *130*, 16770-16777.
- (15) Tang, J.; Hinds, S.; Kelley, S. O.; Sargent, E. H. *Chem. Mater.* **2008**, *20*, 6906-6910.

- (16) Guo, Q.; Hillhouse, H. W.; Agrawal, R. *J. Am. Chem. Soc.* **2009**, *131*, 11672-11673.
- (17) Riha, S. C.; Parkinson, B. A.; Prieto, A. L. *J. Am. Chem. Soc.* **2009**, *131*, 12054-12055.
- (18) Steinhagen, C.; Panthani, M. G.; Akhavan, V.; Goodfellow, B.; Koo, B.; Korgel, B. A. *J. Am. Chem. Soc.* **2009**, *131*, 12554-12555.
- (19) Kameyama, T.; Osaki, T.; Okazaki, K.-i.; Shibayama, T.; Kudo, A.; Kuwabata, S.; Torimoto, T. *J. Mater. Chem.* **2010**, *20*, 5319-5324.
- (20) Shavel, A.; Arbiol, J.; Cabot, A. *J. Am. Chem. Soc.* **2010**, *132*, 4514-4515.
- (21) Katari, J. E. B.; Colvin, V. L.; Alivisatos, A. P. *J. Phys. Chem.* **1994**, *98*, 4109-4117.
- (22) Tricoli, A.; Pratsinis, S. E. *Nat. Nanotechnol.* **2010**, *5*, 54-60.
- (23) Haram, S. K.; Santhanam, K. S. V. *Thin Solid Films* **1994**, *238*, 21-26.
- (24) Haram, S. K.; Santhanam, K. S. V.; Neumannspallart, M.; Levyclement, C. *Mater. Res. Bull.* **1992**, *27*, 1185-1191.
- (25) Gurin, V. S.; Prokopenko, V. B.; Alexeenko, A. A.; Wang, S.; Prokoshin, P. V. *Mater. Sci. Eng., C* **2001**, *15*, 93-95.
- (26) Machado, K. D.; de Lima, J. C.; Grandi, T. A.; Campos, C. E. M.; Maurmann, C. E.; Gasperini, A. A. M.; Souza, S. M.; Pimenta, A. F. *Acta Crystallographica B* **2004**, *60*, 282-286.
- (27) Al-Mamun; Islam, A.; Bhuiyan, A. H. *J. Mater. Sci. - Mater. Electron.* **2005**, *16*, 263-268.
- (28) Jagminas, A.; Juskenas, R.; Gailiute, I.; Statkute, G.; Tomasiunas, R. *J. Cryst. Growth* **2006**, *294*, 343-348.
- (29) Seoudi, R.; Shabaka, A. A.; Elokr, M. M.; Sobhi, A. *Mater. Lett.* **2007**, *61*, 3451-3455.
- (30) Chen, W. S.; Stewart, J. M.; Mickelsen, R. A. *Appl. Phys. Lett.* **1985**, *46*, 1095-1097.

- (31) Hermann, A. M.; Fabick, L. *J. Cryst. Growth* **1983**, *61*, 658-664.
- (32) Okimura, H.; Matsumae, T.; Makabe, R. *Thin Solid Films* **1980**, *71*, 53-59.
- (33) Abdullaev, G. B.; Aliyarova, Z. A.; Asadov, G. A. *Phys. Stat. Sol.* **1967**, *21*, 461-464.
- (34) Ambade, S. B.; Mane, R. S.; Kale, S. S.; Sonawane, S. H.; Shaikh, A. V.; Han, S. H. *Appl. Surf. Sci.* **2006**, *253*, 2123-2126.
- (35) Balapanov, M. K.; Zinnurov, I. B.; Mukhamed'yanov, U. K. *Russ. J. Electrochem.* **2007**, *43*, 585-589.
- (36) Dhanam, M.; Manoj, P. K.; Prabhu, R. R. *J. Cryst. Growth* **2005**, *280*, 425-435.
- (37) El Akkad, F.; Mansour, B.; Hendeya, T. *Mat. Res. Bull.* **1981**, *16*, 535-539.
- (38) Hu, Y. X.; Afzaal, M.; Malik, M. A.; O'Brien, P. *J. Cryst. Growth* **2006**, *297*, 61-65.
- (39) Itoh, K.; Usuki, T.; Tamaki, S. *J. Phys. Soc. Jpn.* **1998**, *67*, 3512-3516.
- (40) Kashida, S.; Shimosaka, W.; Mori, M.; Yoshimura, D. *J. Phys. Chem. Solids* **2003**, *64*, 2357-2363.
- (41) Ohtani, T.; Motoki, M.; Koh, K.; Ohshima, K. *Mater. Res. Bull.* **1995**, *30*, 1495-1504.
- (42) Pai, R. R.; John, T. T.; Lakshmi, M.; Vijayakumar, K. P.; Kartha, C. S. *Thin Solid Films* **2005**, *473*, 208-212.
- (43) Pathan, H. M.; Lokhande, C. D.; Amalnerkar, D. P.; Seth, T. *Appl. Surf. Sci.* **2003**, *211*, 48-56.
- (44) Sklyarchuk, V. M.; Plevachuk, Y. O. *Semiconductors* **2002**, *36*, 1123-1127.
- (45) Statkute, G.; Tomasiunas, R. *J. Appl. Phys.* **2007**, *101*, 113715.
- (46) Gosavi, S. R.; Deshpande, N. G.; Gudage, Y. G.; Sharma, R. *J. Alloys Compd.* **2008**, *448*, 344-348.
- (47) Schafer, A.; Kollwitz, M.; Ahlrichs, R. *J. Chem. Phys.* **1996**, *104*, 7113-7121.

- (48) Wang, W. Z.; Yan, P.; Liu, F. Y.; Xie, Y.; Geng, Y.; Qian, Y. T. *J. Mater. Chem.* **1998**, *8*, 2321-2322.
- (49) Puentes, V. F.; Krishnan, K. M.; Alivisatos, A. P. *Science* **2001**, *291*, 2115-2117.
- (50) Peng, X. G.; Manna, L.; Yang, W. D.; Wickman, J.; Scher, E.; Kadavanich, A.; Alivisatos, A. P. *Nature* **2000**, *404*, 59-61.
- (51) Choi, J.; Kang, N.; Yang, H. Y.; Kim, H. J.; Son, S. U. *Chem. Mater.* **2010**, *22*, 3586-3588.
- (52) Deka, S.; Genovese, A.; Zhang, Y.; Miszta, K.; Bertoni, G.; Krahne, R.; Giannini, C.; Manna, L. *J. Am. Chem. Soc.* **2010**, *132*, 8912-8914.
- (53) Yin, Y.; Alivisatos, A. P. *Nature* **2005**, *437*, 664-670.
- (54) Morgan, N. Y.; Leatherdale, C. A.; Drndic, M.; Jarosz, M. V.; Kastner, M. A.; Bawendi, M. *Phys. Rev. B* **2002**, *66*, 075339.
- (55) Porter, V. J.; Mentzel, T.; Charpentier, S.; Kastner, M. A.; Bawendi, M. G. *Physical Review B* **2006**, *73*, 155303.
- (56) Moulder, J. F.; Stickle, W. F.; Sobol, P. E.; Bomben, K. D. *Handbook of x-ray photoelectron spectroscopy : a reference book of standard spectra for identification and interpretation of XPS data*; Physical Electronics, Inc.: Minnesota, 1995.
- (57) Cahen, D.; Ireland, P. J.; Kazmerski, L. L.; Thiel, F. A. *J. Appl. Phys.* **1985**, *57*, 4761-4771.
- (58) Balapanov, M. K.; Yakshibaev, R. A.; Mukhamed'yanov, U. K. *Phys. Solid State* **2003**, *45*, 634-638.
- (59) Bikkulova, N. N.; Stepanov, Y. M.; Mikolaichuk, A. N. *Russ. J. Electrochem.* **2007**, *43*, 595-597.
- (60) Skomorokhov, A. N.; Trots, D. M.; Knapp, M.; Bikkulova, N. N.; Fuess, H. *J. Alloys Compd.* **2006**, *421*, 64-71.
- (61) Folmer, J. C. W.; Jellinek, F. *Journal of the Less-Common Metals* **1980**, *76*, 153-162.
- (62) Kalyva, M.; Siokou, A.; Yannopoulos, S. N.; Wagner, T.; Orava, J.; Frumar, M. *J. Non-Cryst. Solids* **2009**, *355*, 1844-1848.

- (63) Ogorelec, Z.; Celustka, B. *J. Phys. Chem. Solids* **1969**, *30*, 149-155.
- (64) Manna, L.; Scher, E. C.; Alivisatos, A. P. *J. Am. Chem. Soc.* **2000**, *122*, 12700-12706.
- (65) Milliron, D. J.; Hughes, S. M.; Cui, Y.; Manna, L.; Li, J.; Wang, L. W.; Alivisatos, A. P. *Nature* **2004**, *430*, 190-195.
- (66) Murray, C. B.; Norris, D. J.; Bawendi, M. G. *J. Am. Chem. Soc.* **1993**, *115*, 8706-8715.
- (67) Peng, X.; Wickham, J.; Alivisatos, A. P. *J. Am. Chem. Soc.* **1998**, *120*, 5343-5344.
- (68) Qu, L.; Peng, Z. A.; Peng, X. *Nano Lett.* **2001**, *1*, 333-337.
- (69) Park, J.; Lee, S.; Lee, H. H. *Organic Electronics* **2006**, *7*, 256-260.

Supporting Information for:

**Cu<sub>2</sub>Se Nanoparticles with Dual Functionality Due to a Controlled Solid-State Phase  
Transition Driven by Copper Oxidation and Cationic Conduction**

*Shannon C. Riha, Derek C. Johnson, and Amy L. Prieto*

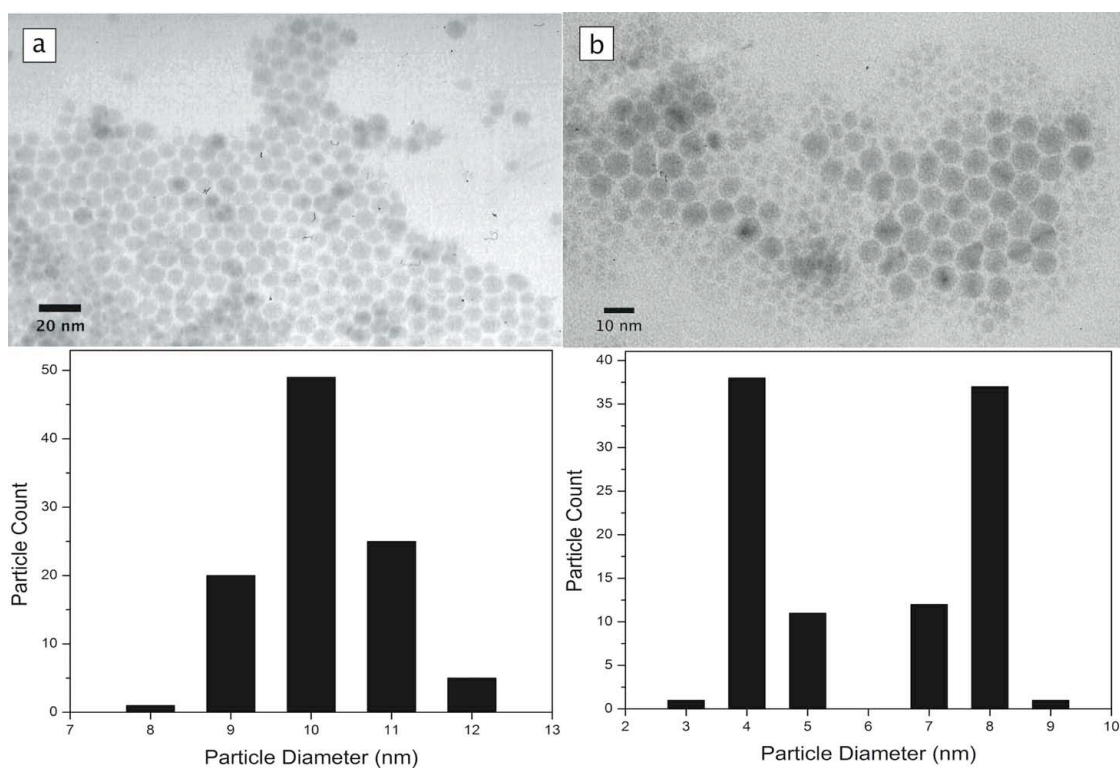


**Figure S7.1.** TEM images of Cu<sub>2</sub>Se nanoparticles along with the corresponding size distribution plots. (a) Cu<sub>2</sub>Se nanoparticles synthesized by simultaneous injection of TOPSe and TOPCu. The TEM image and size distribution plot clearly shows a monodisperse system with a particle size of  $10.1 \pm 0.8$  nm, a monodispersity of 8.1%. (b) Cu<sub>2</sub>Se nanoparticles synthesized by injecting TOPSe at a faster rate than TOPCu. A bimodal distribution is depicted by the image and the size distribution plot clearly shows a bimodal distribution with particle sizes of  $4.2 \pm 0.4$  nm and  $7.8 \pm 0.4$  nm, which gives a monodispersity of 4.9% and 8.6%, respectively.

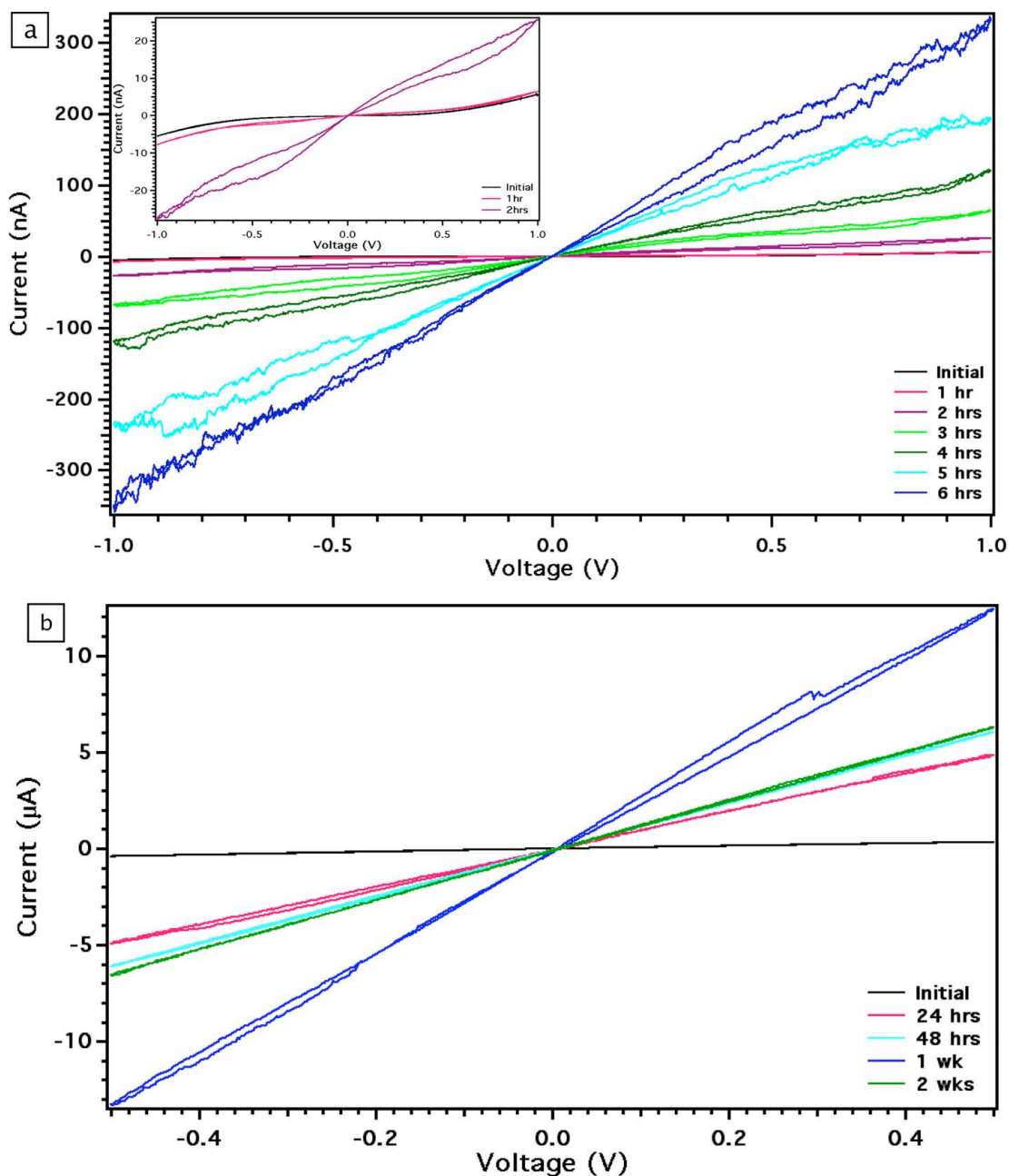


**Figure S7.2.** Plots of current as a function of voltage from Cu<sub>2</sub>Se nanoparticle thin film devices at varying exposure times to air. (a) Current response was measured once the device was removed from the inert atmosphere of the glovebox and subsequently recorded once an hour for six hours. The maximum current increased almost two orders of magnitude when compared to the initial scan, while simultaneously converting from semiconducting to ohmic. (b) Current response studied for 2 wks of air exposure in order to correlate chemical changes and crystal structure transformations to transport properties. The characteristics of the curves are similar to that observed in (a) with a large increase in current and an ohmic response.

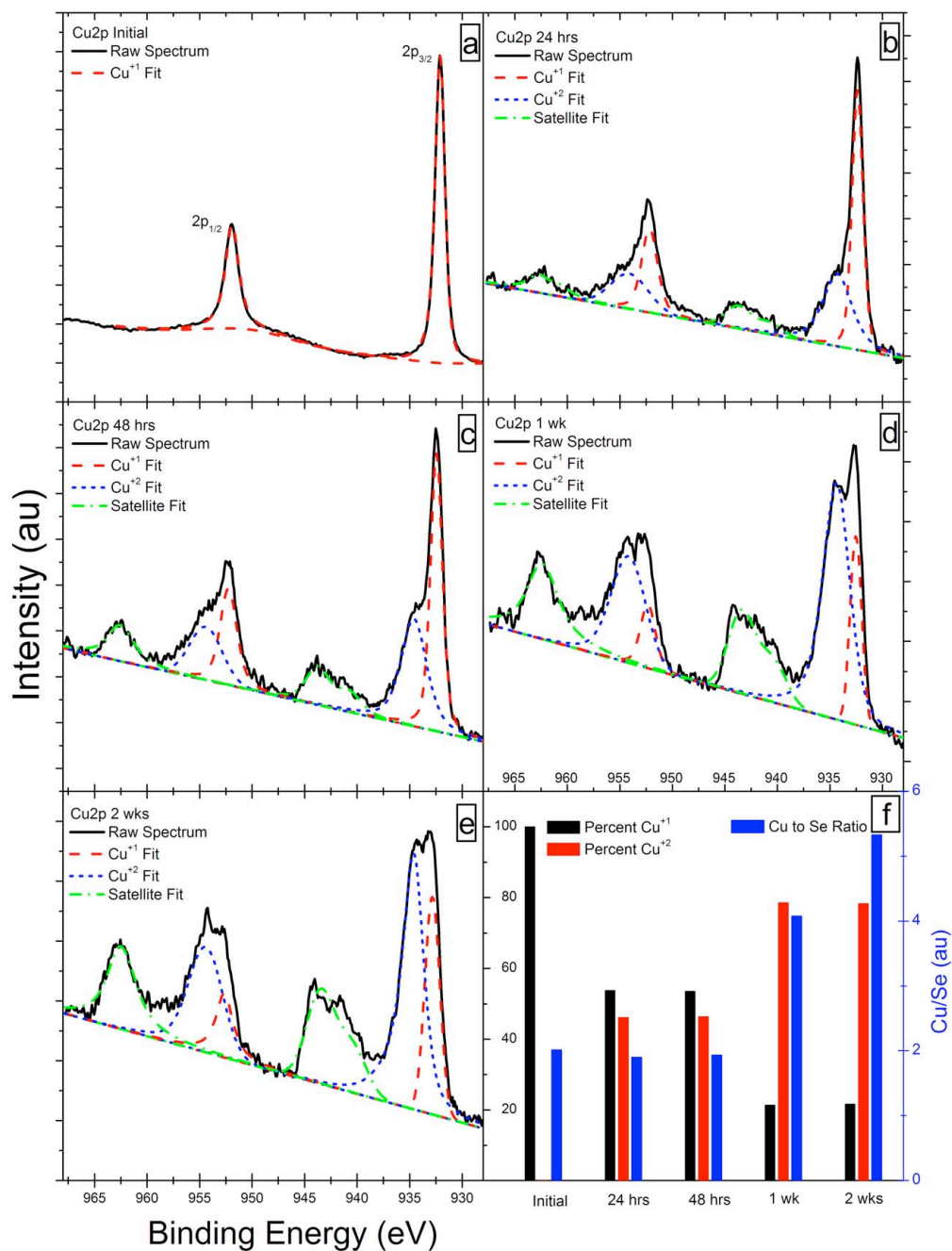


**Figure S7.3.** High resolution XPS Cu2p region spectra of Cu<sub>2</sub>Se nanoparticles as a function time exposed to air. Panels (a) – (e) correspond to spectra recorded for the initial particles and 24 hr, 48 hr, 1 wk and 2 wks of exposure, respectively. Each set of spectra contains the raw spectrum and a peak fit for Cu(I). Panels (b) – (e) also contain peak fits for Cu(II) and shake-up satellites. Panel (f) displays the percentage of surface Cu(I) and Cu(II), left y-axis, and the ratio of total Cu to Se, right y-axis, as a function of exposure time.

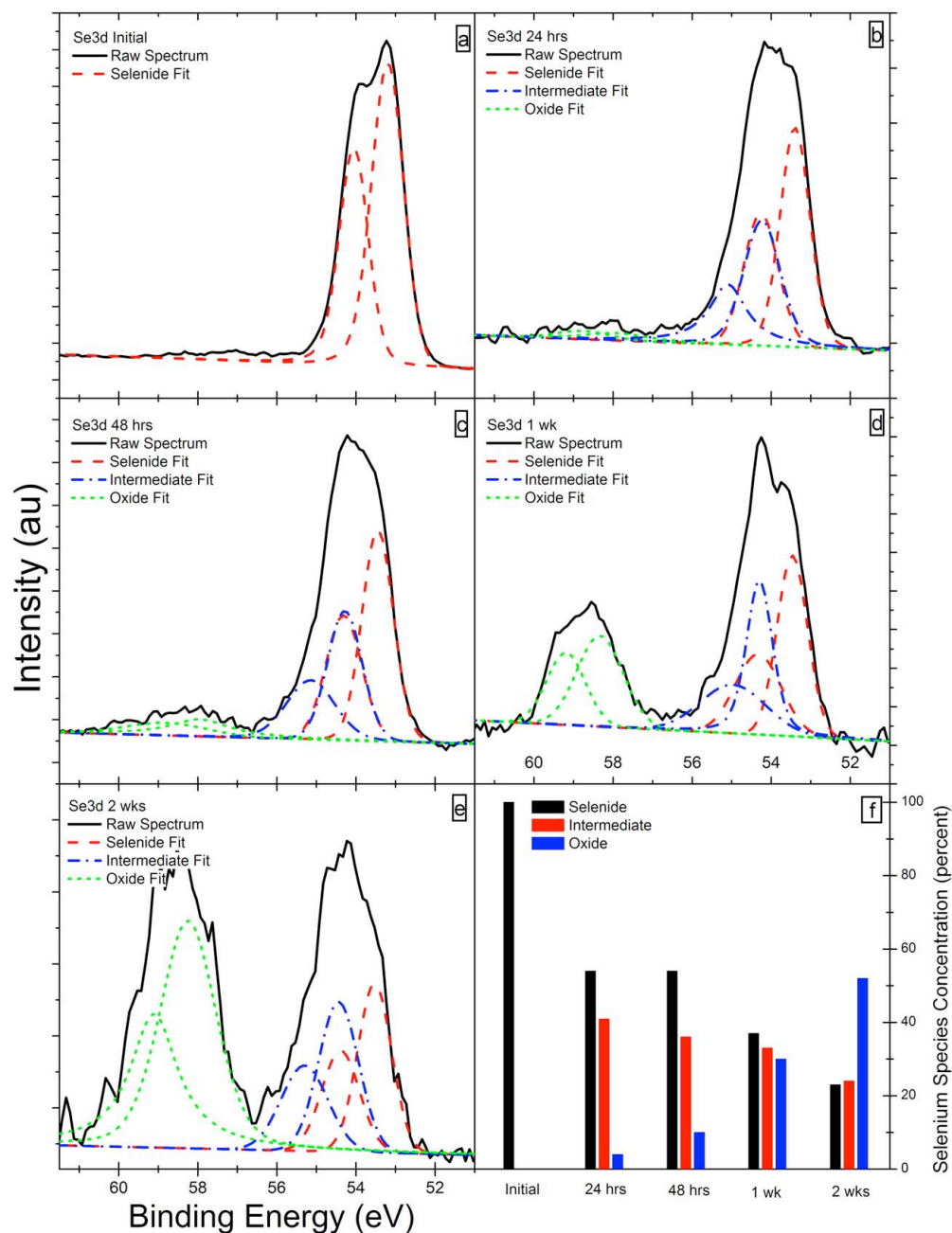


**Figure S7.4.** High resolution XPS Se3d region spectra of  $\text{Cu}_2\text{Se}$  nanoparticles as a function of time exposed to air. Panels (a) – (e) correspond to spectra recorded for the initial particles and 24 hr, 48 hr, 1 wk and 2 wks of exposure, respectively. Each set of spectra contains the raw spectrum and a peak fit for the selenide species. Panels (b) – (e) also contain peak fits for the intermediate species as well as the oxide. Panel (f) displays the percent of each selenium species—selenide, intermediate and oxide—as a function of exposure time.

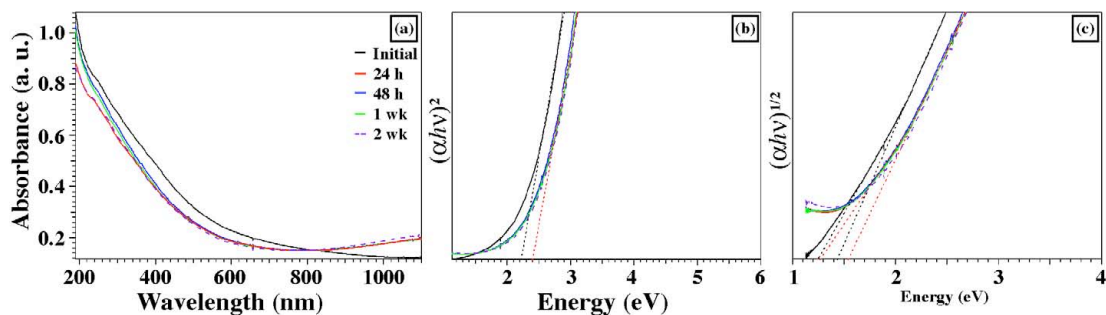


**Figure S7.5.** UV-Vis spectra of Cu<sub>2</sub>Se nanoparticle films as a function of time exposed to air. Panel (a) shows the absorption spectrum highlighting a change in the absorbance after 24 h. Panels (b) and (c) plot the direct and indirect band gaps, respectively. The initial direct band gap is 2.2 eV with an indirect band gap of 1.3 eV. After 24 h of air exposure the direct band gap increases to 2.4 eV, while the indirect band gap increases to 1.4 eV. The absorption spectra remain the same for the 48 h, 1 wk, and 2 wk measurements, suggesting the optical properties are immediately changed by air exposure.

## CHAPTER 8

### SUMMARY

The worldwide high-energy demand and the negative impact on the environment resulting from the use of carbon-based fuels are driving the implementation of renewable energy into our current energy market. Of the different types of renewable energies, solar power is one energy source that has not made a significant contribution to the energy market. Although solar power has the potential to produce enough energy to power the planet, it is not cost-competitive with carbon-based fuels. Efforts towards reducing this cost have been achieved by the introduction of 2<sup>nd</sup> generation devices, which rely on less materials usage while maintaining moderate efficiencies. However, these devices currently require the use of high energy processing methods, which are not amenable for large-scale production. Therefore, new initiatives are driven towards solution-processed thin film solar cells using nanocrystal inks of earth abundant semiconducting materials.

Nanocrystals offer several advantages for use in thin film solar cells, such as a size tunable band gap. Moreover, the advantage of deposition under ambient temperature and pressure render them amenable for inexpensive large-scale production. While the advantages of using nanocrystals in photovoltaic devices are numerous, thin films made

from such materials suffer from poor charge carrier transport and low device efficiencies. Although sintering the nanocrystals in the thin film is an effective solution, annealing the nanocrystals at high temperatures eliminates quantum confinement effects, creates structural defects, increases production costs, and limits large-scale processing. Rather, the goal of the research discussed herein has been to control the optical and electronic properties of the nanocrystals, as well as the charge transport through nanocrystal thin films, through composition tuning and simple surface chemistry treatments.

In order to accomplish this, the focus of this dissertation was placed on the  $\text{Cu}_2\text{ZnSnS}_4$  (CZTS) system. CZTS is an ideal photovoltaic material, with an optimal band gap, high absorption coefficient, and a high degree of tunability compared to potential binary materials. Here it was demonstrated that high quality nanocrystals of CZTS were synthesized by the hot injection method. Chapters 5 and 6 highlight the tunability of this quaternary material by showing that composition can be used to tune the optical and electronic properties. In Chapter 5, the copper to zinc ratio was altered, changing the overall composition of the CZTS nanocrystals. Using photoelectrochemical characterization, nanocrystal thin films of each composition were compared. Our results indicated that copper-poor/zinc-rich stoichiometries lead to higher photocurrents and higher photon conversion efficiencies. Furthermore, it was determined that minority carrier diffusion and recombination via the redox couple at the back contact are the main loss mechanisms.

In many reports, CZTS nanocrystal thin films are annealed in the presence of Se; however, little is known about the effect of Se-inclusion in the CZTS system. The synthesis of  $\text{Cu}_2\text{ZnSn}(\text{S}_{1-x}\text{Se}_x)_4$  nanocrystal solid-solutions was presented in Chapter 6, as

a route to directly probe the effect of Se inclusion. The increase in selenium content introduced into the CZTS system leads to a decrease in the band gap energy, as well as an increase in conductivity.

To overcome recombination and poor charge carrier transport, an alternative approach to sintering nanocrystal thin films has been presented using a different copper-based system. In this study, it was determined that the controlled oxidation of stoichiometric copper selenide ( $\text{Cu}_2\text{Se}$ ) nanocrystals lead to a solid-state conversion to  $\text{Cu}_{1.8}\text{Se}$  nanocrystals. More importantly, the surface oxidation resulted in an increase in the film conductivity by introducing a more conductive pathway for charge carriers to travel through. Therefore, simple surface chemistry treatments to enhance charge transport in nanocrystal thin films can be used as alternatives to nanocrystal sintering.

The experimental results discussed within this dissertation open up new avenues for research in the area of nanocrystal thin film optoelectronics.  $\text{Cu}_2\text{ZnSn}(\text{S}_{1-x}\text{Se}_x)_4$  is emerging as a very promising photovoltaic material; however, this material has only been investigated as a solar absorber in the past decade and since it is a quaternary material it is quite complex. There have been many reports now in the literature, in addition to the two discussed in this dissertation, for the synthesis of  $\text{Cu}_2\text{ZnSnS}_4$  nanocrystals. Because of the different reagents and ligand choices, these nanocrystals have different surface chemistry. We already discussed that the surface chemistry impacts the photophysical properties; however, these materials have not been compared one to one. In fact we observed a difference between the CZTS nanocrystals prepared by the synthesis method in Chapter 4 and Chapter 6 in the photoelectrochemical data as well as in the annealing affects. Appendix 1 shows the results from the photoelectrochemical characterization of

$\text{Cu}_2\text{ZnSn}(\text{S}_{1-x}\text{Se}_x)_4$  nanocrystal thin films. Therefore, synthesizing CZTS nanocrystals by each method and testing the materials by photoelectrochemical characterization is warranted. As discussed, nanocrystal thin film solar cells, including CZTS-based devices, have suffered from low efficiencies without post-deposition annealing, while annealing in a Se vapor drastically enhances device efficiencies. We have successfully synthesized compositionally controlled  $\text{Cu}_2\text{ZnSn}(\text{S}_{1-x}\text{Se}_x)_4$  nanocrystal solid-solutions in effort to probe the role of Se-inclusion in CZTS. Future directions could be aimed towards studying the difference between annealing pure  $\text{Cu}_2\text{ZnSnS}_4$  nanocrystals in Se vapor versus annealing the  $\text{Cu}_2\text{ZnSn}(\text{S}_{1-x}\text{Se}_x)_4$  nanocrystal solid-solutions (with controlled Se content) to determine the optimal S:Se ratio. Photoelectrochemical characterization is a quick way to screen the two approaches (Appendix 1). Ultimately, both preparation methods should be used towards the fabrication of a complete solid-state device.

Although annealing is a quick way to minimize recombination losses, ultimately the goal of nanocrystal thin film research should be to move away from annealing and instead use simple surface chemistry treatments. The results from the  $\text{Cu}_2\text{Se}$  work presented in Chapter 7 suggest that the conductivity of nanocrystal thin films can be tuned by controllable surface oxidation, so long as the resultant surface oxide is more conductive than the non-oxidized nanocrystals. A more in depth study on the kinetics of oxygen uptake in an oxygen-only environment may be warranted. From this, one could optimize the oxide shell thickness and further determine the photophysical characteristics of the core-shell  $\text{Cu}_2\text{Se}$  nanocrystals. Although  $\text{Cu}_2\text{Se}$  may not be the ideal solar absorber material, one can apply these results to a much more promising system, like

CZTS,Se. For example, changing the surface chemistry by using more conducting ligands, such as metal chalcogenide complexes, could result in improved electron transport in the CZTS,Se nanocrystal thin films and enhance solar cell performance without the need for post-deposition annealing. What would be even more promising is to combine the idea of the core-shell formation in the  $\text{Cu}_2\text{Se}$  results with the improved conductivity observed in the CZTS,Se experiments. Creating CZTS/CZTS,Se/CZTSe gradient core-shell nanocrystals, in combination with simple chemical surface treatments, offers an even better route to enhancing CZTS-based nanocrystal thin film efficiencies.

## APPENDIX 1

### PHOTOELECTROCHEMICAL CHARACTERIZATION OF $\text{Cu}_2\text{ZnSn}(\text{S}_{1-x}\text{Se}_x)_4$ NANOCRYSTALS THIN FILMS

***Photoelectrochemical Characterization.*** The decrease in band gap energy with increasing Se content would suggest a lower efficiency based on the Shockley-Queisser approximation. Furthermore, incorporation of sodium borohydride in the synthesis method appeared to etch the particles, affecting the surface chemistry. Preliminary photoelectrochemical characterization—described in Chapter 5—was performed to determine the effect of Se inclusion and synthetic method on the photophysical properties. We tested both as-deposited nanocrystal thin films (Figure A1a), prepared by the layer-by-layer dip casting procedure described in Chapter 5, and nanocrystal thin films that were annealed at low temperatures (Figure A1b). The *in situ* ligand exchange allowed the long insulating ligands inherent from the nanocrystal synthesis to be replaced by short and volatile capping ligands. Annealing the nanocrystal thin films facilitates the removal of these volatile ligands, which should result in grain growth. The films were loaded into a quartz tube with the presence of additional CZTS,Se nanocrystal powder (of the same composition) and placed in a horizontal tube furnace. The tube was pumped and

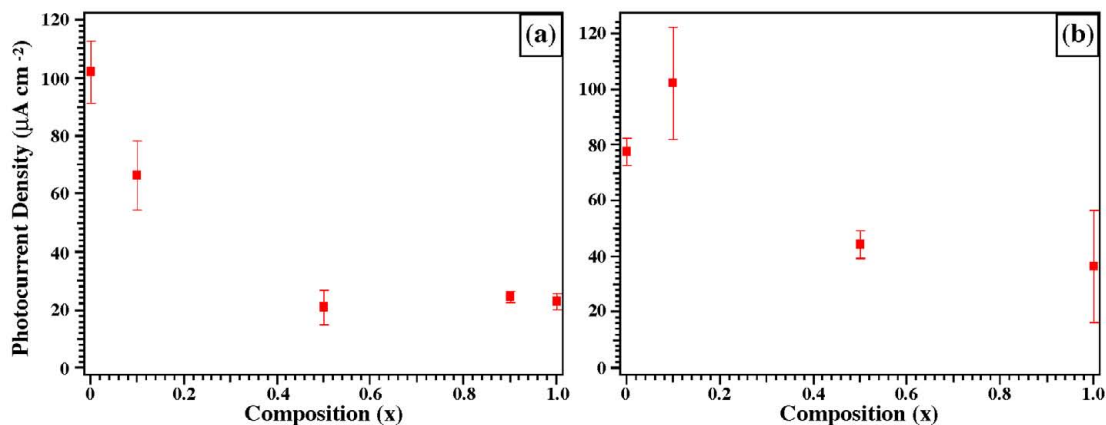


**Figure A1.** Photocurrent density from (a) as-deposited and (b) annealed CZTS,Se thin films, measured as a function of the  $\text{Cu}_2\text{ZnSn}(\text{S}_{1-x}\text{Se}_x)_4$  nanocrystal composition. The photocurrent was measured at  $-450$  mV vs Ag|AgCl using a 17 mW 532 nm laser in a 0.1 M KCl/0.1M Eu(III) aqueous electrolyte.

purged 3x with Ar and then the pressure was raised to 1000 Torr where it remained for the entire annealing process. The temperature was ramped to 350 °C at a rate of 10 °C/min. It was held at 350 °C for 1.5 hrs before self-cooling to room temperature. From the PEC data taken from as-deposited nanocrystal thin films, we observed a decrease in the photocurrent density with an increase in the Se content (shown in Figure A1a). Similarly, Figure A1b shows the photocurrent density for the annealed thin films as a function of the  $\text{Cu}_2\text{ZnSn}(\text{S}_{1-x}\text{Se}_x)_4$  thin film composition. In this case, the annealing does not show significant improvement as compared to the 10-fold increase observed with the CZTS nanocrystals synthesized by the method in Chapter 4, nor was significant grain growth observed. One explanation is that the annealing time and temperature chosen were based on results from Chapter 4, and have not been optimized for this set of nanocrystals. Nonetheless, we observe a similar trend as the as-deposited CZTS,Se nanocrystal thin films. As the Se content increased, the photocurrent density decreased, with the exception of when  $x = 0.1$ . It is quite interesting that the highest photocurrent

was obtained with 10% Se inclusion. Further investigation into this composition is underway. This data suggests that the formation of CZTS,Se alloys are not likely responsible for the improved performance; however, these results are from only one wavelength of light. We attempted to measure IPCE data for the entire visible spectrum but we were not able to obtain a sufficient amount of photocurrent to distinguish it from the dark current. Furthermore, electrochemical kinetics and recombination effects limit these results. Also changes in the nanocrystal composition, conductivity and surface chemistry may lead to the observed trends. Therefore, further work to elucidate this behavior is underway.